

POLITECNICO DI TORINO

Master of Science in Mechanical Engineering

Master Thesis

**Optically Accessible Direct-Injection Spark-Ignited  
(DISI) Engine – Experimental Analysis and 3D-  
CFD Simulation**



**Academic Supervisors:**

Prof. Federico MILLO

PhD Andrea PIANO

**CNR – STEMS Supervisors:**

Dr. Simona Silvia MEROLA

Dr. Eng. Adrian IRIMESCU

**Candidate:**

Gerardo STANZIONE

October 2022

# Abstract

Nowadays, the growing importance of human emissions on the environment has led to decreasing emissions from internal combustion engines, and consequently reducing consumption, with ever more stringent regulation. For this reason, the study of lean combustion spark-ignited engines was improved, but this type of combustion is less stable than the stoichiometric one, different researchers are studying what causes this Cycle-to-Cycle Variability (CCV) and how to solve the problem. In this thesis, the kernel formation was investigated in an optically accessible Direct-Injection Spark-Ignition (DISI) engine to correlate its formation with CCV. The work is divided into two main parts, in the first one was reported the thermodynamic analysis of the engine parameters (Indicated Mean Effective Pressure (IMEP), Covariance of the previous parameters ( $COV_{IMEP}$ ), Peak of pressure and its covariance ( $P_{MAX}$  and  $COV_{P_{MAX}}$ ), Mass Fraction Burned (MFB), Net Heat Release Rate (NHRR) etc...); two different spark plugs were used (i.e. Single and Double J-electrode), three different orientations for the first one (Uni-, Cross- and Counterflow with respect to the tumble motion) and two for the second one (Uni- and Crossflow with respect to the tumble motion).

In the second part was developed a 3-D CFD model on the software Converge CFD (v3.0), which reproduced the in-cylinder thermofluidodynamic phenomena of the engine, the data obtained in the experimental part and the previous analysis were used to validate the simulation model. The Reynolds Averaged Navier-Stokes (RANS) together with the RNG  $k - \epsilon$  turbulence model was used to account for the variation of the flow field. To simulate appropriately the combustion phase a detailed chemical kinetics solver (SAGE) was used. The 3-D CFD model allowed us to analyse the variations of the flow field and the mixture composition during the kernel formation to understand the influence of these and different spark plugs on CCV.

# Contents

<b>1. Introduction.....</b>	<b>1</b>
1.1 Background .....	1
1.2 Influence of Engine Parameters .....	2
1.3 Influence of Spark Plug Configuration .....	5
1.4 Influence of Tumble Motion and Mixture Composition.....	11
1.5 Motivation and Research Goal.....	20
<b>2. Experimental Analysis.....</b>	<b>21</b>
2.1 Test Rig Setup .....	21
2.2 Procedure and Measurement Methodology for Thermodynamic Analysis .....	28
2.3 Experimental Conditions.....	30
2.4 Thermodynamic Results.....	32
2.4.1 Thermodynamic Results for Partial Load and Lean Mixture .....	32
2.4.2 Thermodynamic Results for Partial Load and Stoichiometric Mixture .....	37
2.4.3 Thermodynamic Results for WOT conditions and Lean Mixture .....	41
2.4.4 Thermodynamic Results for WOT conditions and Stoichiometric Mixture .....	45
<b>3. 3-D CFD Simulation Analysis.....</b>	<b>50</b>
3.1 Simulation Setup .....	50
3.1.1 Geometry Preparation .....	50
3.1 Cold Cycle Setup.....	52
3.2.1 Boundary Setup.....	52
3.2.2 Regions and Initialization .....	56
3.2.3 Grid Control .....	58
3.3 Cold Cycle Results .....	59
3.3.1 In-Cylinder Mass.....	59
3.3.2 In-Cylinder Thermodynamic Parameters.....	63

3.3.3 In-Cylinder Motion .....	66
<b>4. Conclusions and Future Works .....</b>	<b>69</b>
<b>References.....</b>	<b>73</b>

# List of Figures

Figure 1.1 Bowditch's extension assembly from [3].	1
Figure 1.2 IMEP and $COV_{IMEP}$ for the three engine speed with two $\lambda$ from [5].	2
Figure 1.3 In-cylinder pressure (top), heat release rate (HRR) (middle), volume fraction burned (VFB) (bottom) traces for stoichiometric air-fuel ratio from [5].	3
Figure 1.4 IMEP and $COV_{IMEP}$ for five different $\lambda$ at 1000rpm from [5].	4
Figure 1.5 In-cylinder pressure (top), heat release rate (HRR) (middle), volume fraction burned (VFB) (bottom) traces for three different $\lambda$ at 1000rpm from [5].	5
Figure 1.6 Orientation of single electrode spark plug.	6
Figure 1.7 IMEP and $COV_{IMEP}$ for different air-fuel ratio from [6].	6
Figure 1.8 Mass Fraction Burned (MFB) for $\lambda = 1.3$ from [6].	7
Figure 1.9 IMEP (top) and $COV_{IMEP}$ (bottom) for different SA from [6].	8
Figure 1.10 MFB for SA = 8 CAD (top) and for SA = 16 CAD (bottom) with $\lambda = 1.15$ from [6].	9
Figure 1.11 $COV_{IMEP}$ with different spark plug orientation from [7].	10
Figure 1.12 delta $COV_{IMEP}$ with different spark plug orientation from [7].	10
Figure 1.13 Tumble motion near spark plug at 2000 rpm from [8].	11
Figure 1.14 ISFC (top), SA (middle) and $COV_{IMEP}$ (bottom) with the variation of $\lambda$ at 2000 rpm, 280 kPa IMEP from [8].	11
Figure 1.15 Dilution with air and exhaust gas with T0 (top) and T3 (bottom) tumble at 2000 rpm, 280kPa IMEP from [8].	12
Figure 1.16 First combustion phases with T0 (top) and T3 (bottom) tumble at 2000 rpm, 280kPa IMEP from [8].	13
Figure 1.17 Experimental in-cylinder pressure traces (top), comparison between experimental and simulated in-cylinder pressure from [9].	14
Figure 1.18 COV of engine parameters, comparison between experimental and simulated results from [9].	15
Figure 1.19 Comparison of the velocity field (left) and air-fuel ratio (right) between Cycle 4 and Cycle 5 from [9].	16
Figure 1.20 Cycle 4 in-cylinder pressure with Cycle 5's velocity field (top), Cycle 4 in-cylinder pressure with Cycle 5's mixture field (bottom) from [9].	17
Figure 1.21 (a) Correlation between PCP and XX (left), PCP and Sphericity (right) from [9].	18
Figure 1.22 Flame morphology at 3% MFB for the lowest two and highest two cycles (the exhaust ports are on the right) from [9].	18
Figure 1.23 Velocity field just prior-to-ignition for the lowest four (top) and highest four (bottom) cycles (intake ports were on the left) from [9].	19
Figure 1.24 Correlation between X position of the centre of mass (COMoX) and velocity in the X direction (U5.5mm) just prior-to-ignition from [9].	20
Figure 2.1 Schematic representation of test rig setup from [10].	22
Figure 2.2 (a) Magneti Marelli injector, (b) injector nozzle from [6].	22
Figure 2.3 AVL ETU from [6].	23
Figure 2.4 G.D.I. Control System from [6].	23
Figure 2.5 Engine head with a single spark plug in Uniflow configuration	24
Figure 2.6 Different configurations of the spark plug.	25

Figure 2.7 Test rig setup (top), Electric machine coupled with the engine (49.7 kW power, 230 Nm maximum torque)(bottom) from [6].....	27
Figure 2.8 Description of LabView script.....	28
Figure 2.9 Representation of cylinder geometry from [14].....	29
Figure 2.10 In-Cylinder Pressure with $\lambda = 1.3$ , SA = 20 CAD and WOT conditions. ....	32
Figure 2.11 In-Cylinder Pressure with $\lambda = 1.3$ , SA = 30 CAD and Partial Load. ....	33
Figure 2.12 IMEP and $COV_{IMEP}$ with $\lambda = 1.3$ , SA = 30 CAD and Partial Load. ....	34
Figure 2.13 $P_{MAX}$ and $COV_{P_{MAX}}$ with $\lambda = 1.3$ , SA = 30 CAD and Partial Load. ....	35
Figure 2.14 CA50 with $\lambda = 1.3$ , SA = 30 CAD and Partial Load.....	36
Figure 2.15 CA5 with $\lambda = 1.3$ , SA = 30 CAD and Partial Load.....	36
Figure 2.16 In-Cylinder Pressure with $\lambda = 1.0$ , SA = 16 CAD and Partial Load. ....	37
Figure 2.17 IMEP and $COV_{IMEP}$ with $\lambda = 1.0$ , SA = 16 CAD and Partial Load. ....	38
Figure 2.18 $P_{MAX}$ and $COV_{P_{MAX}}$ with $\lambda = 1.0$ , SA = 16 CAD and Partial Load. ....	39
Figure 2.19 CA50 with $\lambda = 1.0$ , SA = 16 CAD and Partial Load.....	40
Figure 2.20 CA5 with $\lambda = 1.0$ , SA = 16 CAD and Partial Load.....	40
Figure 2.21 In-Cylinder Pressure with $\lambda = 1.3$ , SA = 20 CAD and WOT conditions. ....	41
Figure 2.22 IMEP and $COV_{IMEP}$ with $\lambda = 1.3$ , SA = 20 CAD and WOT conditions. ....	42
Figure 2.23 $P_{MAX}$ and $COV_{P_{MAX}}$ with $\lambda = 1.3$ , SA = 20 CAD and WOT conditions. ....	43
Figure 2.24 CA50 with $\lambda = 1.3$ , SA = 20 CAD and WOT conditions.....	44
Figure 2.25 CA5 with $\lambda = 1.3$ , SA = 20 CAD and WOT conditions.....	44
Figure 2.26 In-Cylinder Pressure with $\lambda = 1.0$ , SA = 10 CAD and WOT conditions. ....	45
Figure 2.27 IMEP and $COV_{IMEP}$ with $\lambda = 1.0$ , SA = 10 CAD and WOT conditions. ....	46
Figure 2.28 $P_{MAX}$ and $COV_{P_{MAX}}$ with $\lambda = 1.0$ , SA = 10 CAD and WOT conditions. ....	47
Figure 2.29 CA50 with $\lambda = 1.0$ , SA = 10 CAD and WOT conditions.....	48
Figure 2.30 CA5 with $\lambda = 1.0$ , SA = 10 CAD and WOT conditions.....	48
Figure 3.1 Frontal view of engine surface.....	51
Figure 3.2 Top view of engine surface.....	51
Figure 3.3 Original valve seat (top), Modified valve seat (bottom). ....	52
Figure 3.4 Intake valve (left), Exhaust valve (right). ....	53
Figure 3.5 Intake and exhaust valve lift profile.....	53
Figure 3.6 (a) Inflow boundary (green), (b) Outflow boundary (red). ....	55
Figure 3.7 (a) Total intake pressure, (b) Total intake temperature, (c) Static exhaust pressure, (d) Static exhaust temperature of cold cycle.....	55
Table 3.2 Boundaries and regions. ....	57
Figure 3.8 Regions: blue cylinder, green intake system and red exhaust system. ....	58
Figure 3.9 Exhaust mass flow of cold cycle and exhaust vales lift. ....	60
Figure 3.10 Closing phase of exhaust valves. ....	60
Figure 3.11 Intake mass flow of cold cycle and intake vales lift. ....	61
Figure 3.12 Opening phase of intake valves. ....	61
Figure 3.13 Closing phase of intake valves.....	62
Figure 3.14 In-Cylinder mass during the cold cycle. ....	63
Figure 3.15 In-cylinder pressure during cold cycle.....	63
Figure 3.16 Logarithmic diagram of cold cycle. ....	64

Figure 3.17 Detail of the logarithmic diagram of cold cycle.....	65
Figure 3.18 In-cylinder temperature during cold cycle. ....	65
Figure 3.19 Air flow motion inside the chamber: tumble (blue), cross tumble (orange) and swirl (green). ....	66
Figure 3.20 Tumble and turbulent intensity of the cold cycle.....	67
Figure 3.21 Flow motion on the plane passing through the intake valve axis:-315 CAD (a), -270 CAD (b), -200 CAD (c), -90 CAD (d) and -10 CAD (e) .....	68

# List of Tables

Table 2.1 Engine characteristics. ....	21
Table 2.2 Experimental conditions .....	31
Table 3.1 Initialization temperature for WALL boundaries for cold cycle. ....	54
Table 3.2 Boundaries and regions .....	57
Table 3.3 Initialization values of regions. ....	58

# Acronyms and Symbols

AFR Air-Fuel Ratio

AMR Adaptive Mesh Refinement

ATDC After Top Dead Center

BDC Bottom Dead Center

BTDC Before Top Dead Center

CAD Crank Angle Degree

CCV Cycle-to-Cycle Variability

CFD Computational Fluid Dynamics

COV Coefficient of Variation

DOI Duration of Injection

ICE Internal Combustion Engine

DISI Direct-Injection Spark-Ignition

EVC Exhaust Valve Closing

EVO Exhaust Valve Opening

HRR Heat Release Rate

IMEP Indicated Mean Effective Pressure

IVC Intake Valve Closing

IVO Intake Valve Opening

KH Kelvin-Helmholtz

LES Large Eddy Simulation

MBT Maximum Brake Torque

MFB Mass Fraction Burned

NHRR Net Heat Release Rate

NTC No Time Counter

PFI Port Fuel Injection

RANS Reynolds-Averaged Navier-Stokes

RT Rayleigh-Taylor

SA Spark Advance

SOI Start of Injection

TDC Top Dead Center

VFB Volume Fraction Burned

3-D 3-Dimensional



# 1. Introduction

## 1.1 Background

Over the past few years, the continuous need to increase the efficiency of internal combustion engines (ICE) led to the use of lean burn combustion in Direct-Injection Spark-Ignition as a good method to reduce fuel consumption and emission of  $CO_2$ , but this type of combustion has a higher Cycle-to-Cycle Variability (CCV) [1-2].

Therefore, a lot of scientific studies tried to understand the main cause of this CCV and how to reduce it by modifying the orientation of the spark plug electrode with respect to tumble motion, but also the type of spark plug (normally single or double J-electrode).

For these studies, the use of an optically accessible engine allows us to view the displacement of the first flame kernel with respect to the electrode, this type of engine uses a Bowditch's extension with a quartz piston [3-4] that enables the possibility to observe what happens during the combustion in the combustion chamber.

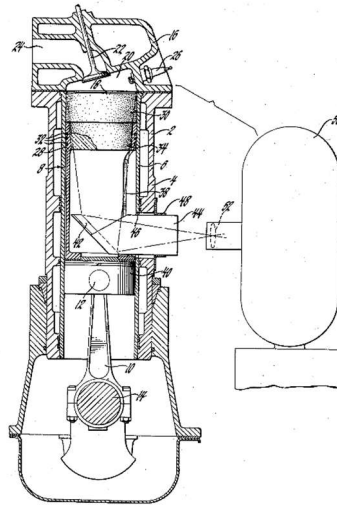


Figure 1.1 Bowditch's extension assembly from [3].

## 1.2 Influence of Engine Parameters

Engine parameters influence the CCV in DISI engine, therefore, Irimescu, A., Merola, S. and Martinez, S. [5] studied the influence of engine speed and injection phasing in lean combustion, and also, the influence of the variation of dilution on  $COV_{IMEP}$ .

First of all, the influence of different engine speeds was analysed with two different  $\lambda$  values, MBT timing was used for lean combustion and constant spark advance (SA) for  $\lambda = 1$ .

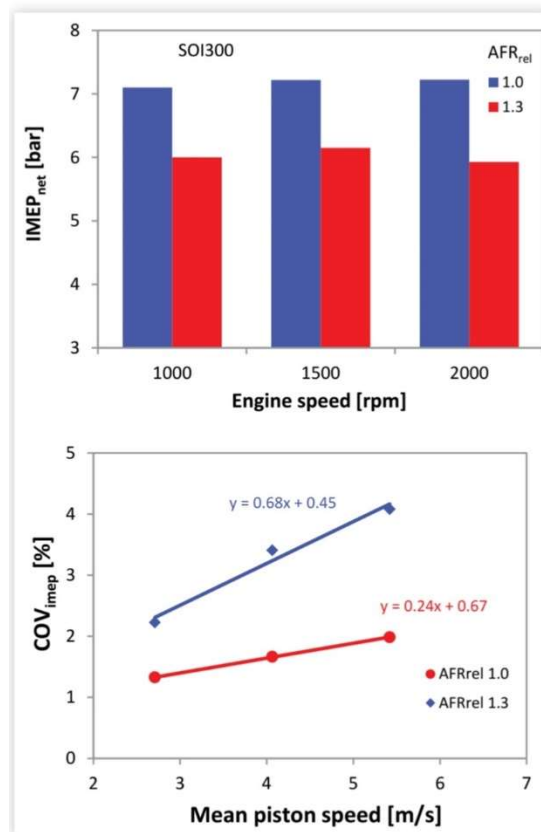


Figure 1.2 IMEP and  $COV_{IMEP}$  for the three engine speed with two  $\lambda$  from [5].

It was seen that the IMEP value was approximately constant at around 7 bar with the stoichiometric mixture and around 6 bar with the lean combustion, moreover, during the lean combustion, the medium speed (1500 rpm) ensured a slightly higher IMEP. For this experimental part, was used constant spark timing (i.e. 10 CAD BTDC) for  $\lambda = 1.0$ , instead, for  $\lambda = 1.3$  was employed the MBT timing. Furthermore, the lean combustion allowed to reach an increase of 8% in fuel conversion efficiency compared to  $\lambda = 1$ .

The  $COV_{IMEP}$  values were below 5%, which was the threshold for stable combustion, furthermore, growth rates were higher with lean combustion, one of the factors that influence the slope was the SA but the main factors were the flow field and the turbulence intensity

which was proportional to engine speed, their effect became more important with a lean mixture while the combustion velocity decreased.

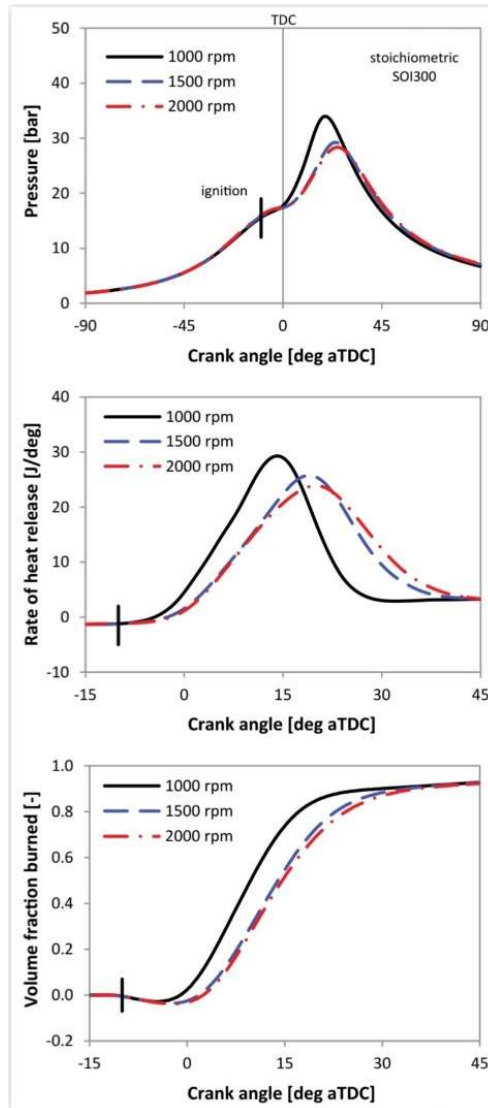


Figure 1.3 In-cylinder pressure (top), heat release rate (HRR) (middle), volume fraction burned (VFB) (bottom) traces for stoichiometric air-fuel ratio from [5].

The Pressure, HRR and VFB traces (Figure 1.3) demonstrated that SA for 1000 rpm was retarded, this caused a peak of pressure resulting in increased blow-by losses, indeed, with low speed, the blow-by losses were 15% higher than the charge at the end of the intake stroke, instead, at maximum engine speed this value was around 10%. These peaks of pressure and HRR disappeared during lean combustion with MBT timing, thus the value of spark timing was very important in the blow-by losses.

The second part of this study analysed the variation of air-fuel ratio, from  $\lambda = 1.0$  to  $\lambda = 1.6$ , with constant engine speed (1000 rpm) and MBT timing. From experimental data (Figure 1.4) was deduced that the IMEP value decreased with increasing air-fuel ratio, it

started from 7 bar for stoichiometric mixture and decreased up to 5 bar for the combustion with  $\lambda = 1.6$ , and vice versa, the value of  $COV_{IMEP}$  increased with  $\lambda$ , only with  $\lambda=1.6$  the threshold of 5% was exceeded (almost  $COV_{IMEP} = 6\%$ ), the increase of variability was approximately linear for the value from stoichiometric mixture to  $\lambda=1.5$ .

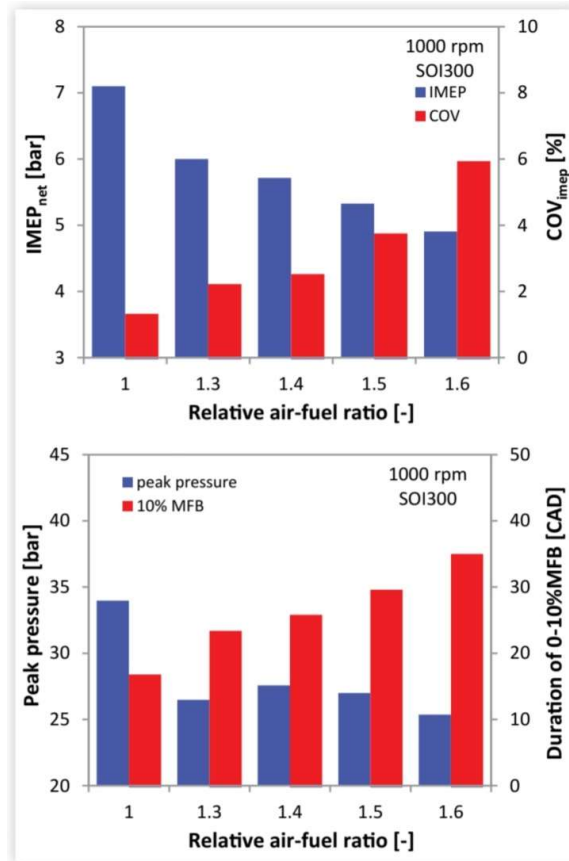


Figure 1.4 IMEP and  $COV_{IMEP}$  for five different  $\lambda$  at 1000rpm from [5].

Figure 1.4 shows, also, the values of peak pressure, as expected, the stoichiometric combustion reached the maximum peak of pressure (around 34 bar) while the lowest peak pressure was obtained with the leanest mixture, the variation of pressure was not linear, indeed, the combustion with  $\lambda = 1.3$  obtain a value lower than the  $\lambda = 1.4$  one. In this experimental case the duration of 0-10% MFB was calculated, the variation was monotonous as the air-fuel ratio increased, for the stoichiometric ratio the duration of the first combustion phase was around 18 CAD, instead, the duration reached values around 35 CAD with the leanest mixture.

The pressure traces shown in Figure 1.5 are useful to demonstrate that the use of MBT timing with all the values of  $\lambda$  allowed to avoid the peak of pressure, this was confirmed by the traces of the rate of heat release, only with the leanest case the peak of pressure was lightly

shifted toward the TDC, this was probably due to the almost flat trace of HRR. The negative value of VFB was due to the simplified model used to calculate these traces.

Lastly, the fuel conversion efficiency was calculated, it reached its maximum value at  $\lambda = 1.5$ , after which efficiency was decreased with a higher  $\lambda$  value.

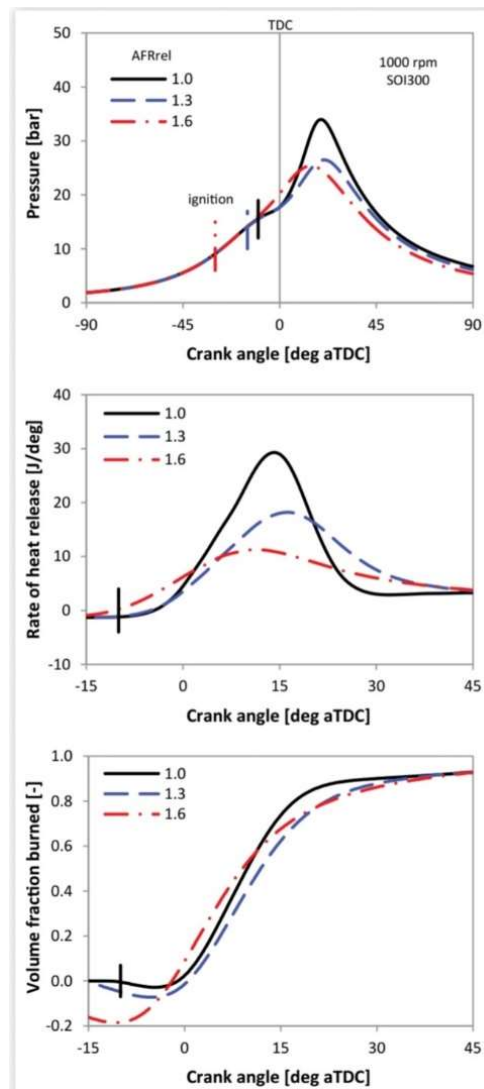


Figure 1.5 In-cylinder pressure (top), heat release rate (HRR) (middle), volume fraction burned (VFB) (bottom) traces for three different  $\lambda$  at 1000rpm from [5].

### 1.3 Influence of Spark Plug Configuration

The spark plug configuration has a very important influence on CCV, in particular, the type of spark plug and its orientation with respect to tumble motion, [6] investigated the effect of the orientation of a single electrode spark plug in an optically accessible engine, also, was investigated the effect of  $\lambda$  and SA variation at 2000 rpm.

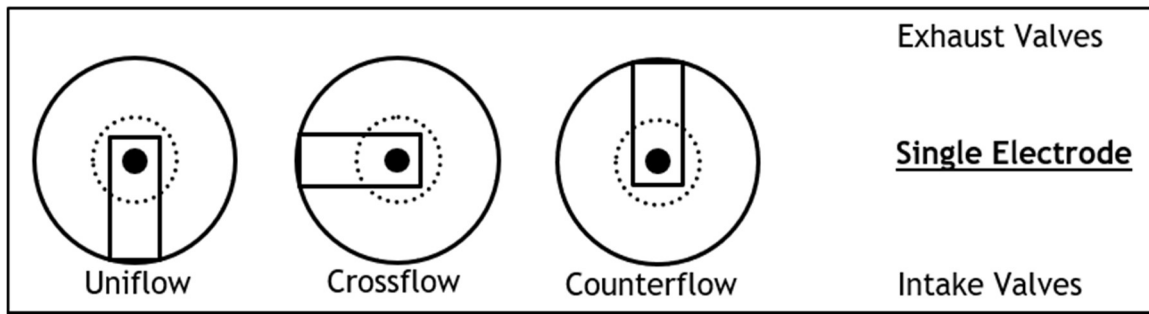


Figure 1.6 Orientation of single electrode spark plug.

It analysed three values of air-fuel ratio ( $\lambda = 1/1.15/1.3$ ) with fixed SA



Figure 1.7 IMEP and  $COV_{IMEP}$  for different air-fuel ratio from [6].

Figure 1.7 shows that the IMEP value was about the same in all spark plug orientations, as expected the values of IMEP were the highest with the stoichiometric mixture (around 8.5 bar) and decreased as mixtures were leaned out, indeed, with  $\lambda = 1.3$  obtained IMEP values almost 6.5 bar.  $COV_{IMEP}$  values were very high with the poorest mixture, up to 11.8% with Counterflow orientation, and exceed the threshold value for stable combustion, in the combustion with  $\lambda = 1$  the variability was almost constant with the three orientations, while

Crossflow reached the highest variability with  $COV_{IMEP}$  around 3% for the combustion with  $\lambda = 1.3$ .

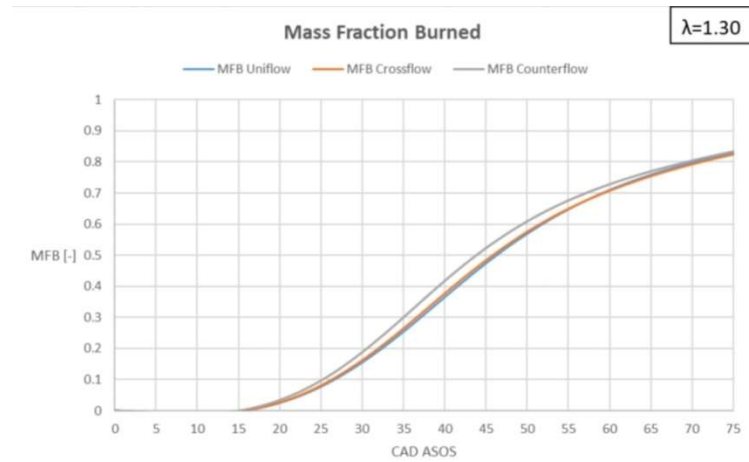


Figure 1.8 Mass Fraction Burned (MFB) for  $\lambda = 1.3$  from [6].

Furthermore, Figure 1.8 demonstrates that lean combustion reached MFB50 more slowly with respect to richer mixtures, 45 CAD ASOS with the leanest mixture, while MFB50 = 28 CAD ASOS for  $\lambda = 1$ . Overall, Uniflow and Counterflow orientations obtained alternatively the lowest combustion duration, in particular with the leanest mixture Counterflow allowed to obtain the fastest combustion. Moreover, the duration of kernel development (0-10% MFB) increased with the poorest combustion, passing from 17 CAD with  $\lambda = 1$  to 25 CAD for the leanest mixture. Overall, the combustion with the Uniflow configuration is faster than others.

Afterwards, it examined the effect of different SA (SA = 8/12/16/20/24 CAD) with  $\lambda = 1.15$ .

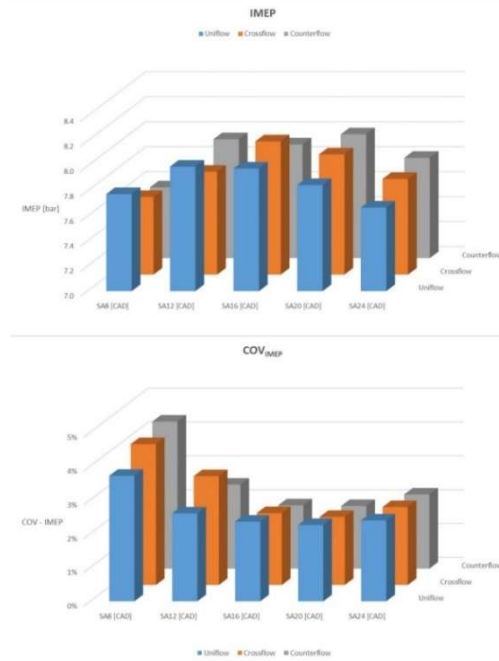


Figure 1.9 IMEP (top) and  $COV_{IMEP}$  (bottom) for different SA from [6].

In Figure 1.9 can see that IMEP values with Uniflow and Crossflow orientations increased with the increase of Spark Advance up to 16 CAD, where was obtained the maximum value (IMEP = 8 bar) with Crossflow configuration, for  $SA \geq 16$  CAD the values decreased and with  $SA = 24$  CAD, in these conditions, Counterflow obtained the highest IMEP value (almost 7.8 bar). For SA lower than 16 CAD the Uniflow configuration allowed to obtain the highest values. Overall, the  $COV_{IMEP}$  values were below the stability threshold (5%), indeed the most instability combustion was obtained with  $SA = 8$  CAD and Counterflow configuration (almost 4.2%), the stability increased as SA was increased up to 16 CAD, where the Counterflow reached the lowest value ( $COV_{IMEP} = 1.7\%$ ). After this minimum value the stability decreased with the increase of SA because the combustion was more anticipated, the values were around 2% with all the configurations. The Uniflow orientation ensured the lowest instability with the retarded combustion but the highest with the anticipated combustion.

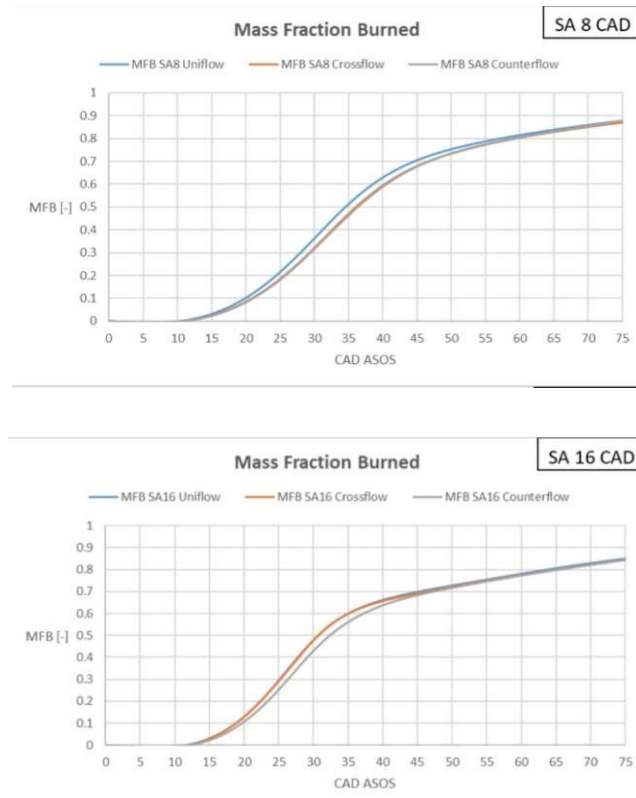


Figure 1.10 MFB for SA = 8 CAD (top) and for SA = 16 CAD (bottom) with  $\lambda = 1.15$  from [6].

Lastly, the traces of MFB were analysed (Figure 1.10), and the combustion was slower for delayed SA with Uniflow which was the configuration with faster burning (MFB50 = 35 CAD ASOS) while Crossflow and Counterflow orientation had the same trend with an MFB50 = 37 CAD ASOS. With a SA = 16 CAD BTDC, the burning velocity was higher, Crossflow and Uniflow had the same traces and were the fastest orientation, and Counterflow was the slowest. The minimum value of MFB with this SA was 30 CAD ASOS with respect to 35 CAD ASOS of the previous case, instead, the highest value of MFB50 was 33 CAD ASOS, then, lower than the maximum of the case with SA = 8 CAD BTDC. From SA > 16 CAD BTDC the three orientations had the same MFB trend with a value of MFB50 equal to 30 CAD ASOS.

The results, in terms of  $COV_{IMEP}$  values, were confirmed by [7], this report was carried out on a production 2.5 L V-6 4 valves engine, only one cylinder was instrumented to perform the tests while the others worked normally, indeed, in the cylinder no. 5 there was a pressure transducer (Kistler, Model 6043), while an encoder was used to correlate the data from the transducer with crank angle position. During the tests was investigated the effect of air-fuel ratio variation with different positions of a single electrode spark plug, the engine speed was 1500 rpm with 262kPa BMEP. In this test, the flow direction was towards 300°.

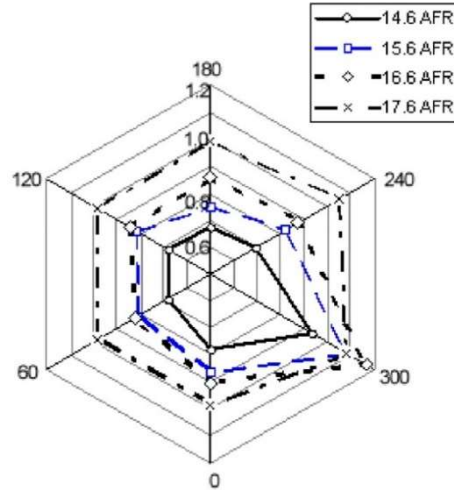


Figure 1.11  $COV_{IMEP}$  with different spark plug orientation from [7].

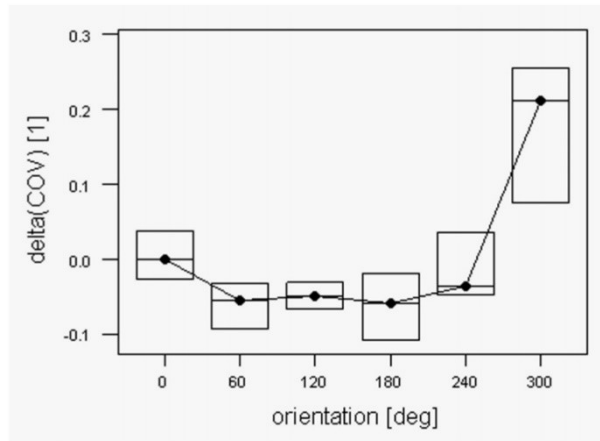


Figure 1.12  $\Delta COV_{IMEP}$  with different spark plug orientation from [7].

$COV_{IMEP}$  values, obviously, increased with the leaner mixture, Figure 1.11 shows a radar plot, all the orientation had the same variability with all the air-fuel ratio with a minimum value obtained in stoichiometric combustion, then the orientation of the electrode was not important except in “Counterflow” orientation (300°) that obtain the worse result with all the  $\lambda$  values.

Figure 1.12 shows that  $COV_{IMEP}$  had a certain variability during the various cycles, the “Uniflow” configuration (120°) had the lower variability with respect to mean value, and “Counterflow” (300°) the major one. Other cases (60° and 180°) were similar to Crossflow but the differences between these and 120° were small, while the “Counterflow” orientation had a very large variability with a median value of 0.2, instead, the median value of “Uniflow” configuration was around -0.5.

## 1.4 Influence of Tumble Motion and Mixture Composition

Tumble motion has a central role in the flame kernel development and consequently in CCV, [8] analysed the influence of several levels of tumble flow in a highly diluted mixture, the dilution was with air either exhaust gas recirculation (EGR). Four different percentage of tumble motion was analysed, Figure 1.13 shows that T0 was the standard one and T3 was the maximum one, as expected, both tumble's mean velocity decreased near the TDC but T3 ensured always a higher speed.

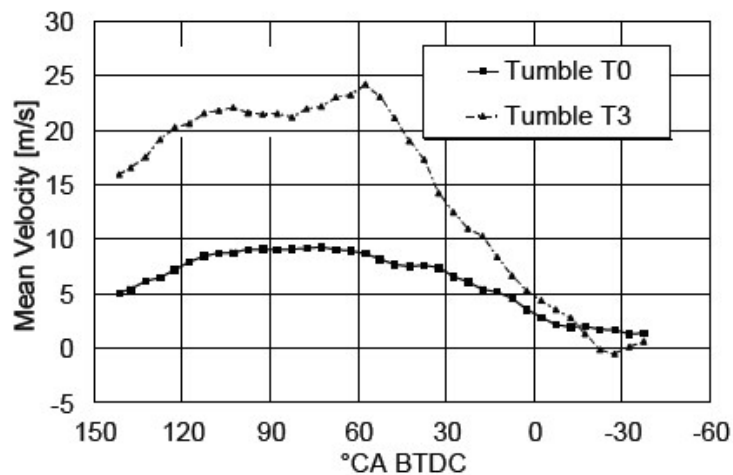


Figure 1.13 Tumble motion near spark plug at 2000 rpm from [8].

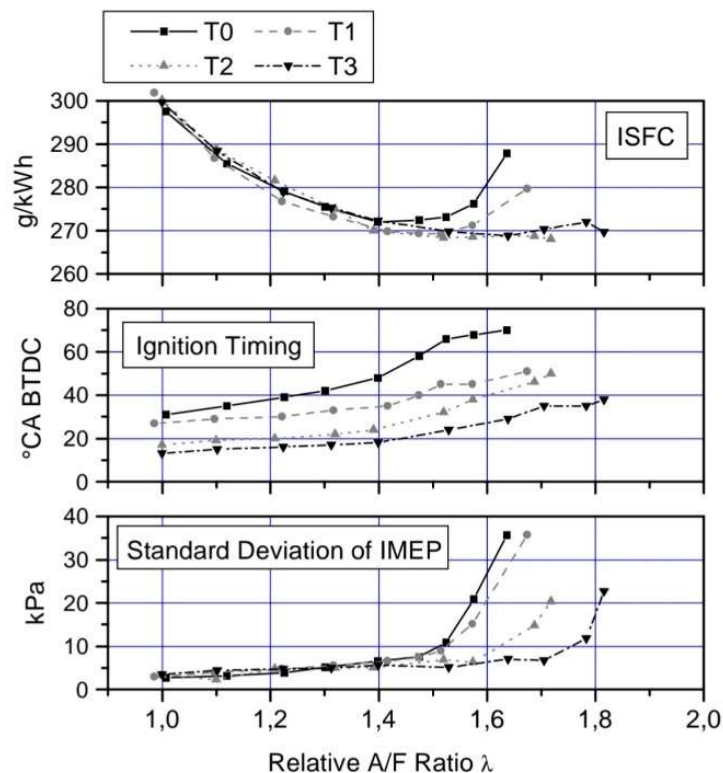


Figure 1.14 ISFC (top), SA (middle) and  $COV_{IMEP}$  (bottom) with the variation of  $\lambda$  at 2000 rpm, 280 kPa IMEP from [8].

The tumble level had a very important influence on combustion as shown in Figure 1.14, a greater tumble allowed to achieve higher values of  $\lambda$  (about  $\lambda = 1.8$ ) with stable combustion (low  $COV_{IMEP}$ , in this work, was considered the Standard Deviation of IMEP) and contained SA ( $40^\circ$  CAD BTDC), also, fuel consumption dropped significantly thanks to lean mixture. With the standard tumble motion, it was possible to reach an air-fuel ratio around 1.6 but with a higher spark advance ( $70$  CAD BTDC) and the same stability, but the fuel consumption increased,  $280$  g/kWh respect to  $269$  g/kWh with T3 and  $\lambda = 1.6$ . In [8] scientists analysed also the effect of tumble with two different dilution methods, air (higher  $\lambda$ ) and EGR.

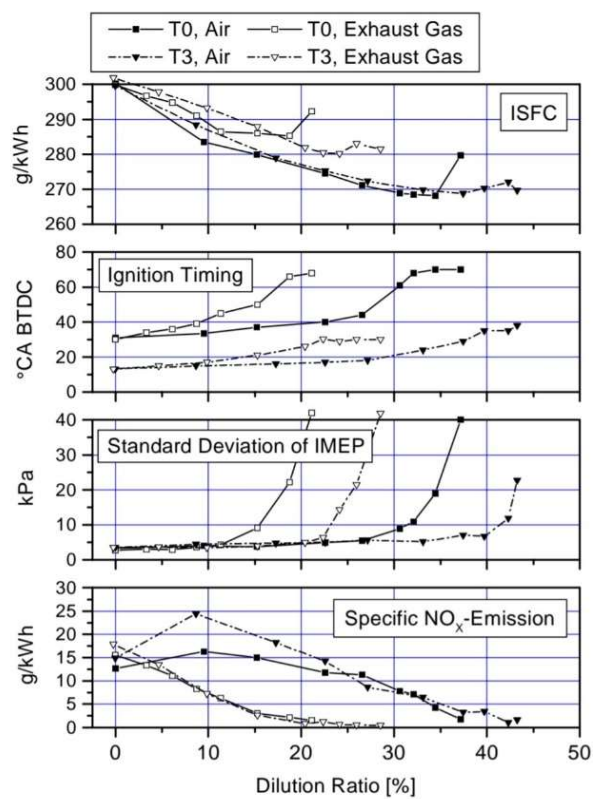


Figure 1.15 Dilution with air and exhaust gas with T0 (top) and T3 (bottom) tumble at 2000 rpm, 280kPa IMEP from [8].

As expected, a higher level of tumble ensured more stable combustion with both dilution methods, indeed, T3 allowed 10 kPa of standard deviation of IMEP with a 40% air-dilution ratio, compared to T0 which showed 20 kPa of standard deviation of IMEP with a 35% air-dilution ratio. The same with EGR dilution (Figure 1.15), which allowed to use of a 15% exhaust gas dilution with a T0 tumble level, this configuration obtained a standard deviation of IMEP equal to 10 kPa, and the same variability was obtained with a dilution of around 23% using T3 tumble level. In this part of the analysis were examined also the effect of tumble and dilution on  $NO_x$  emissions, and a higher reduction of emissions was ensured with

a low EGR-dilution ratio. Unlike, emissions were higher with a lower air-dilution ratio, probably for higher gas temperature due to a greater level of the tumble. In terms of fuel consumption, air-dilution obtained the best results with an ISFC value of around 270 g/kWh with 35% dilution, increasing dilution percentage with T0 showed a slightly higher fuel consumption, while with T3 the ISFC value was about the same. With EGR dilution, the fuel consumption decreased but was lower than in the previous case, also with this dilution the ISFC values with T3 tumble level were lower and the possibility to use a higher percentage of EGR allowed to obtain a minimum ISFC value of 280 g/kWh with respect to 292 g/kWh with the lower tumble level.

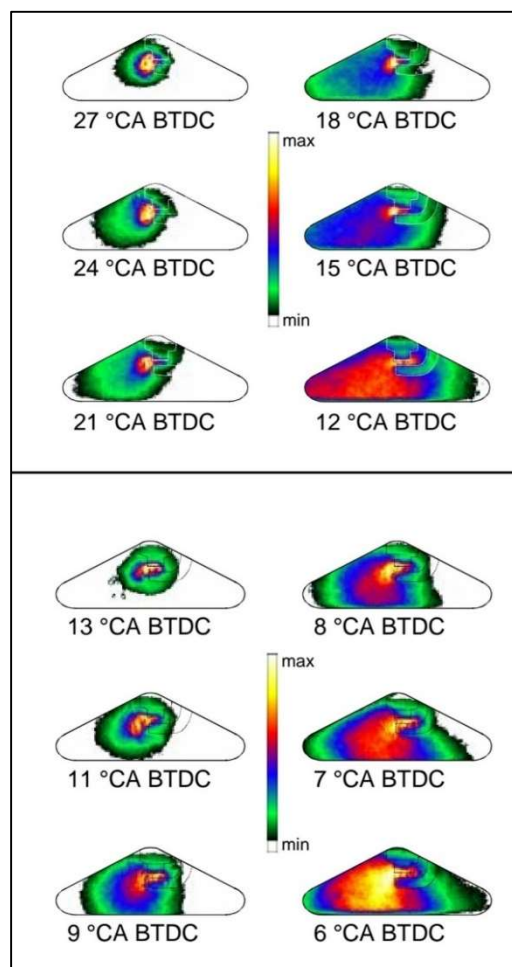


Figure 1.16 First combustion phases with T0 (top) and T3 (bottom) tumble at 2000 rpm, 280kPa IMEP from [8].

Figure 1.16 shows the flame kernel development in an optically accessible engine, the combustion with T0 (and SA = 37° CA BTDC) was more slowly (top), and the first kernel appeared after 10° CAD, with respect to 4° CAD when T3 level of tumble was used (bottom). Furthermore, the kernel displacement was higher with the T0 level than T3 because the ratio between the speed of combustion and the tumble speed is low. Lastly, Figure 1.16 shows

that the duration of burning is lower with T3 level, 7° CAD compared to 15° CAD with T0. Overall, the burning velocity was higher with T3 tumble motion as we see in the figure above.

The influence of tumble was studied also in [9], the authors analysed the CCV in SI engine using a large-eddy simulation (LES) and G-equation combustion model to understand the influence of velocity and equivalent ratio fields. The simulation was performed using CFD code CONVERGE and the model was validated through experimental tests with a 1.4 L in-line four-cylinder SI-PFI FGW engine, with an effective CR = 9.72 and an engine speed of 2500 rpm, the intake pressure and temperature were respectively 1.51 bar and 304 K. In the CFD model, the base mesh size was 0.7 mm in the cylinder and became 0.175 mm near the spark plug during combustion phases with the use of CONVERGE's adaptive mesh refinement (AMR).

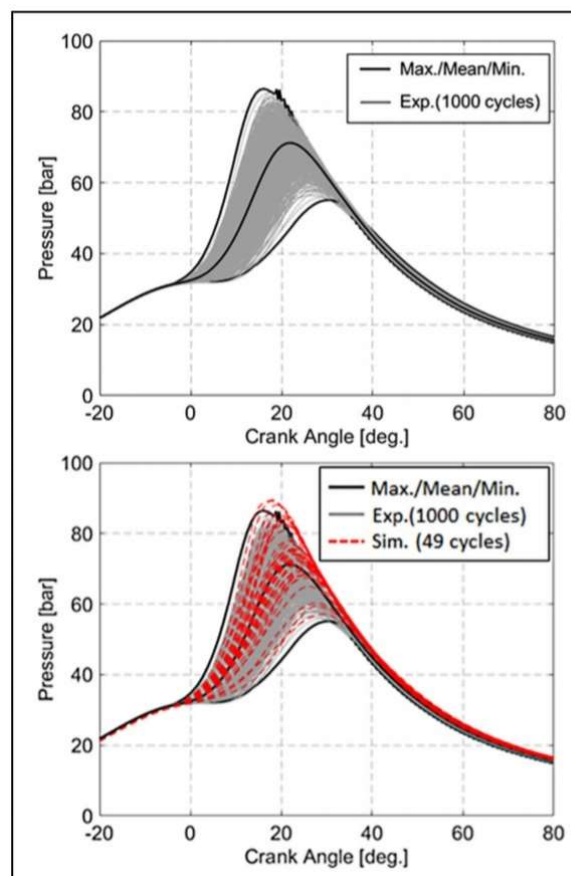


Figure 1.17 Experimental in-cylinder pressure traces (top), comparison between experimental and simulated in-cylinder pressure from [9].

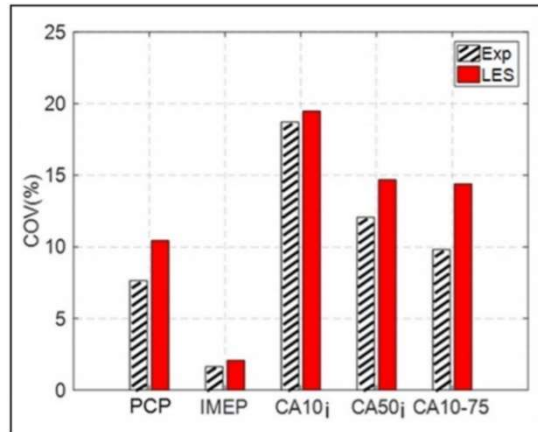


Figure 1.18 COV of engine parameters, comparison between experimental and simulated results from [9].

Figure 1.17 shows that simulation results were very similar to experimental, the in-cylinder pressure traces of the 1000 experimental cycles were shown at the top side of the figure, simulated pressure traces were added at the bottom side, and the experimental and simulated traces were very close. The  $COV_{IMEP}$  and the variability of different durations of burning (CA10, CA50, CA10-75) are shown in Figure 1.18, also, the differences between these parameters were very small, in particular, the value of  $COV_{IMEP}$  was almost the same, and the simulated variability of CA10 was very close to experimental value. Experimental and simulated  $COV_{IMEP}$  values needed more cycles to reach a quasi-steady value, the simulation did not achieve this stability with only 49 LES cycles. Overall, the simulation model was valid.

After the validation of the model, scientists analysed two particular simulated cycles, a cycle with a high peak of pressure (cycle 4) and a cycle with a low peak of pressure (cycle 5) to understand what cause the different peak pressure.

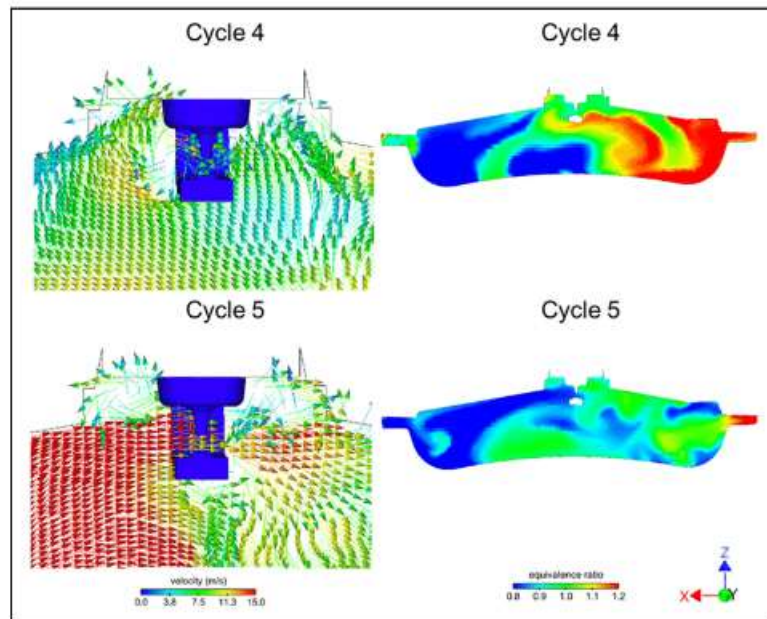


Figure 1.19 Comparison of the velocity field (left) and air-fuel ratio (right) between Cycle 4 and Cycle 5 from [9].

Cycle 4 showed a multi-directional flow with a lower speed and a stoichiometric mixture in the spark gap, vice-versa, Cycle 5 exhibited a unidirectional flow in the negative X direction (toward the exhaust side), which probably was due to tumble motion, and a lower equivalent ratio in the spark gap (Figure 1.19), these two important differences caused the variability of the cycles. To understand which between tumble motion or equivalent ratio had a major influence on cycle pressure and velocity, scientists restarted Cycle 4 with Cycle 5's flow field, after, they computed Cycle 4 with Cycle 5's  $\lambda$  distribution.

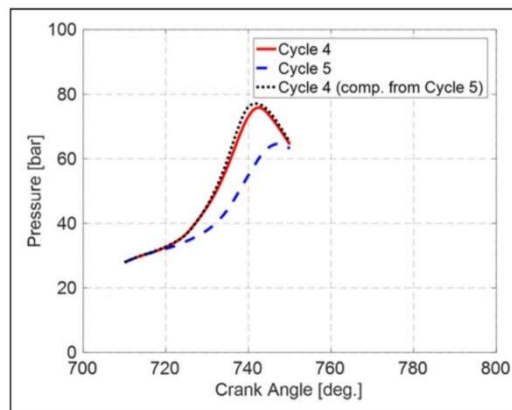
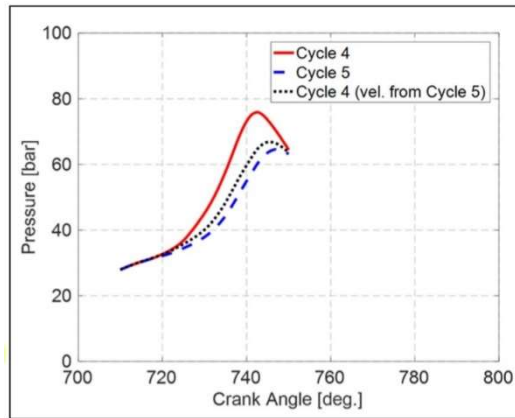


Figure 1.20 Cycle 4 in-cylinder pressure with Cycle 5's velocity field (top), Cycle 4 in-cylinder pressure with Cycle 5's mixture field (bottom) from [9].

Figure 1.20 shows that velocity field was more important than composition distribution, indeed, Cycle 4 with the flow field of Cycle 5 had a lower peak of pressure, slightly higher than the original Cycle 5, instead, Cycle 4 with Cycle 5's composition had a high peak of pressure, very similar to the original Cycle 4.

Lastly, was analysed the correlation between the peak of pressure and the flame topologies.

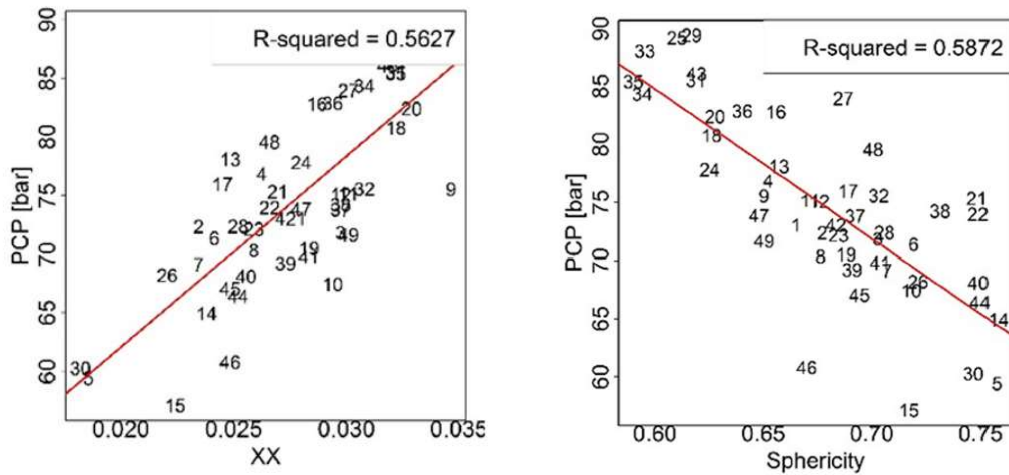


Figure 1.21 (a) Correlation between PCP and XX (left), PCP and Sphericity (right) from [9].

Figure 1.21 shows that a higher displacement in the X direction was correlated with a higher peak of pressure, indeed, the correlation parameter was  $R^2 = 0.5627$ , vice-versa, the cycles that showed a spherical combustion shape obtained lower peak of pressure, as demonstrated at the right side of Figure 1.21. The Z-displacement didn't correlate with PCP; indeed, the correlation parameter was very low ( $R^2 = 0.04884$ ).

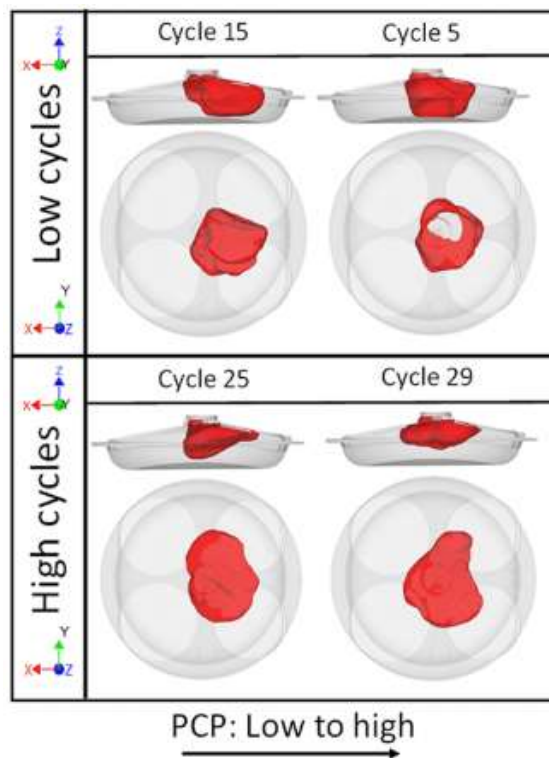


Figure 1.22 Flame morphology at 3% MFB for the lowest two and highest two cycles (the exhaust ports are on the right) from [9].

Another important analysis was performed at the same percentage of MFB = 3% (Figure 1.21) and was compared two lower cycles and two higher cycles to demonstrate that MFB percentage had no effect on ZZ correlation, in the figure above it was possible to see that the low cycles had a higher displacement in Z direction and sphericity, while the flame of high cycles had a squished shape.

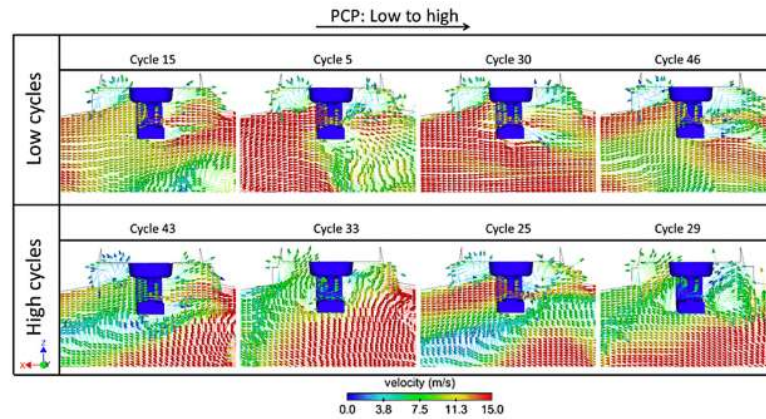


Figure 1.23 Velocity field just prior-to-ignition for the lowest four (top) and highest four (bottom) cycles (intake ports were on the left) from [9].

Figure 1.23 confirmed that low cycles had a higher velocity field in the spark gap toward the negative X direction before the ignition, according to tumble motion; this probably caused the displacement of the flame in that direction later in the cycle. Unlike, high cycles had a higher flow field in the positive Z direction, this motion was like a squish and pushed the flame toward the head, the flame shape became more squashed, and then the burning velocity increased for the greater area-volume ratio. Overall, high cycles (with low CCV) had a higher Z direction velocity and lower in the negative X direction during the ignition.

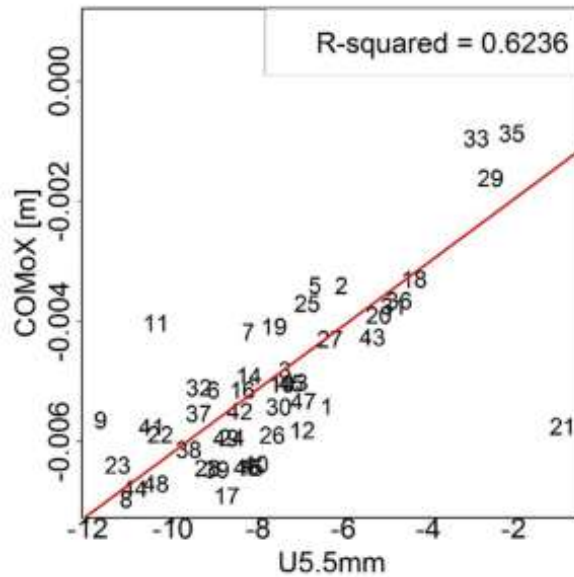


Figure 1.24 Correlation between X position of the centre of mass (COMoX) and velocity in the X direction (U5.5mm) just prior-to-ignition from [9].

The velocity in the X direction had a very important correlation ( $R^2 = 0.5627$ ) with the displacement of the flame toward the exhaust side, the higher the negative X velocity, the higher the displacement in the negative X direction of the flame (Figure 1.24).

## 1.5 Motivation and Research Goal

This work aimed to investigate the influence of the spark plug configuration on the Cycle-to-Cycle Variability (CCV) during lean combustion and to understand the thermodynamic and chemical phenomena that influence kernel formation. A lot of experimental tests were carried out in the laboratory, these allowed us to obtain a large amount of thermodynamic data which was used to validate the 3D-CFD model of the optically accessible GDI engine. The CFD simulation, after proper calibration, allowed to see what happen in the spark gap, in terms of the flow field and mixture composition, during the first burning phase, to understand the correlation between the kernel formation and the cycle-to-cycle variability. During the experimental tests were kept constant the engine speed (1000 rpm) and was used the MBT timing for the five spark plug configurations: Single J-electrode (Uni-, Cross-, Counterflow orientations) and Double J-electrode (Uni-, and Crossflow orientations). Finally, the research goal was to reduce the cycle-to-cycle variability of lean burning, so that this type of combustion can be implemented to reduce environmental pollutants emissions and fuel consumption.

## 2. Experimental Analysis

This work was divided into two main parts, in the first one, described in this chapter, carried out the thermodynamic analysis of the experimental data, in the second part, shown in Chapter 3, the 3-D CFD Simulation of the experimental engine.

### 2.1 Test Rig Setup

The experimental tests were performed in one of the laboratories of the “Istituto di Scienze e Tecnologie per l’Energia e la Mobilità Sostenibili” (CNR-STEMS) in Naples. For these tests was used an optically accessible Direct-Injection Spark-Ignition (DISI) single-cylinder four-stroke engine, engine head was a four-valve pent-roof head properly modified for this optical engine, because, originally this engine head was equipped on a 1.4 L Fiat four-cylinder turbocharged inline engine. The other parts of the test engine were designed to work with Bowditch’s extended piston, furthermore, on the piston top, there was the quartz section that allowed us to see what happens in the combustion chamber during combustion.

Engine characteristics are reported in Table 2.1.

Displacement	399 $cm^3$
Stroke	81.3 mm
Bore	79 mm
Connecting Rod	143 mm
Compression Ratio	10:1
Number of Valves	4
Intake Valves Open	363 CAD bTDC
Intake Valves Close	144 CAD bTDC
Exhaust Valves Open	153 CAD aTDC
Exhaust Valves Close	360 CAD aTDC
Start of Injection	300 CAD bTDC
Fuel Injection System	DI-WG
Fuel used for these tests	Isooctane ( $C_8H_{18}$ )

Table 2.1 Engine characteristics.

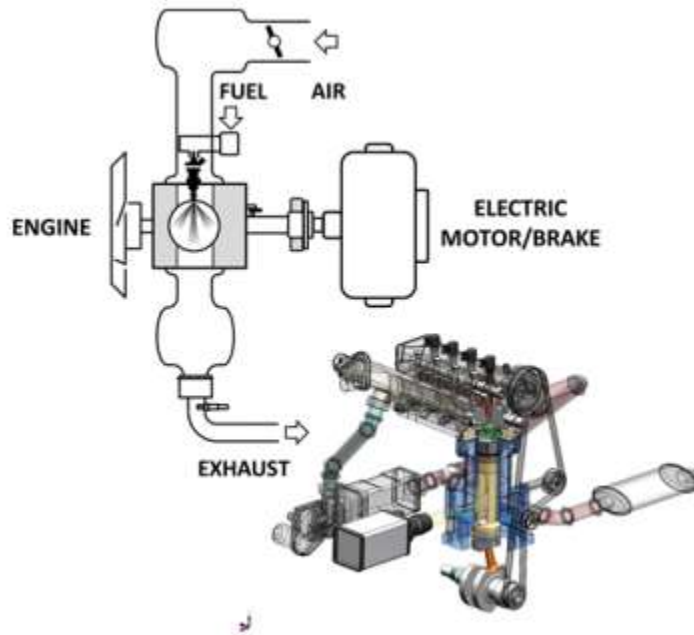


Figure 2.1 Schematic representation of test rig setup from [10].

The optical engine crankshaft was connected to an electric machine that allowed to maintain a constant engine speed; an elastic coupling ensured the connection. The injector was a Magneti Marelli with a six-hole (diameter of holes of 0.140 mm, Figure 2.2), it was fitted between the two intake valves. Wall-guided (WG) mode was used for mixture formation.



(a)



(b)

Figure 2.2 (a) Magneti Marelli injector, (b) injector nozzle from [6].

An optical encoder mounted on the crankshaft was used to synchronize the control triggers for ignition and injection, it was connected to an AVL Engine Timing Unit (ETU) (Figure 2.3). The ETU was a pulse generator that allowed the synchronization between the engine cycle and the encoder. Triggers and Crank Degree Medium (CDM), from the encoder, were

used as inputs command, the first one indicated the TDC position, the CDM the pulses for each angle. An additional electronic control unit (G.D.I. Control System) (Figure 2.4) controlled the injection system, the control unit also ensured a constant fuel rail pressure (100 bar), and a piezoelectric transducer mounted at one of the extremities of the rail was used to verify the correct injection pressure. The start and the duration of the injection were fixed using the input coming from ETU.



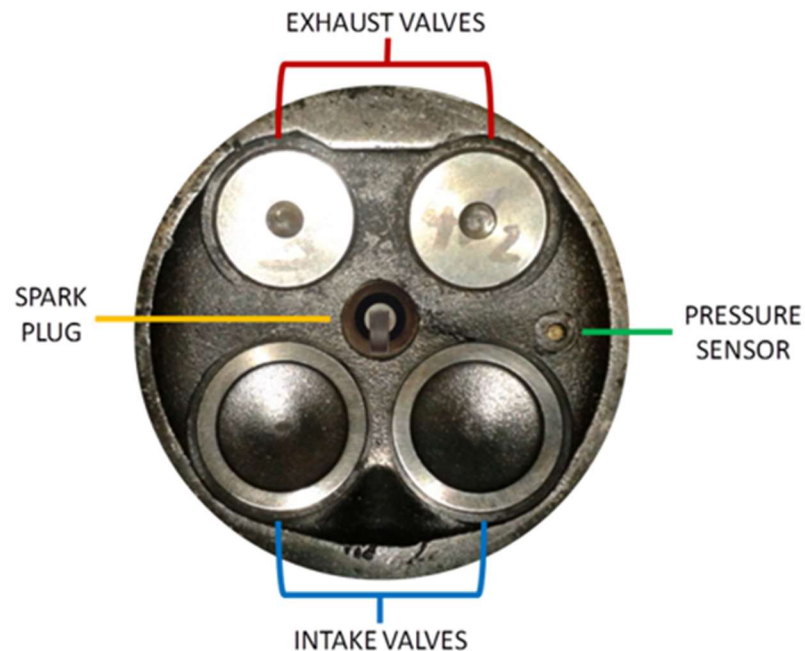
Figure 2.3 AVL ETU from [6].



Figure 2.4 G.D.I. Control System from [6].

The common rail was modified to use only one injector and afterwards tested to check there were no leakages. Furthermore, a low-pressure pump was needed to feed the high-pressure pump. The Start of Injection (SOI) was the same for all experimental tests, that value (reported in Table 2.1) ensured a homogeneous charge.

In these experimental tests were used two different types of spark plugs, the first one was a Single J-type electrode (Bosch - YR7LEU) [11], and the second type was a Double J-type electrode (NGK - DCPR8EKC) [12]. During the experimental tests were investigated three different orientations of single electrode: Uniflow, Crossflow and Counterflow; and two orientations of double electrode: Uniflow and Crossflow. In the Uniflow configuration (both types of the spark plug) the J-electrode protected the center electrode from the flow coming from the intake side. In the Crossflow position (both types of the spark plug) the ground electrode was rotated by 90 degrees with respect to the previous one. In the last configuration, Crossflow, the orientation was opposite to Uniflow. In Figure 2.5 and Figure 2.6 we can see the engine head and the configurations of the spark plug described above.



*Figure 2.5 Engine head with a single spark plug in Uniflow configuration*

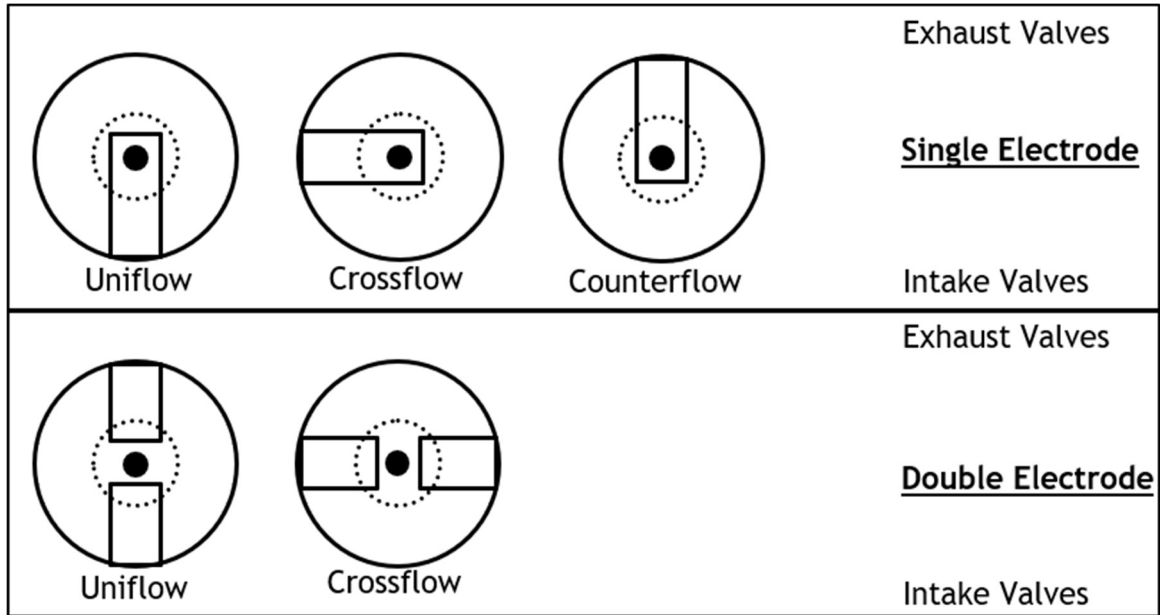


Figure 2.6 Different configurations of the spark plug.

The value of  $\lambda$  was verified with two different devices, the first was a Universal Exhaust Gas Oxygen (UEGO) sensor that has a range of  $0.55 - 1.2 \lambda$  with an accuracy of  $\pm 1\%$ , this sensor was positioned very close to the exhaust manifold. The second device was an AVL DITEST GAS 4000 and it was located down the exhaust line. This device was used to study the composition of exhaust gas, and it measured the  $\lambda$  value by using Brettschneider's equation [13]:

$$\lambda = \frac{CO_2 + \frac{CO}{2} + O_2 + \left( \frac{H_{CV}}{4} \cdot \frac{K}{K + \frac{CO}{CO_2}} - \frac{O_{CV}}{2} \right) \cdot (CO_2 + CO)}{\left( 1 + \frac{H_{CV}}{4} - \frac{O_{CV}}{2} \right) \cdot (CO_2 + CO + K_1 \cdot HC)}$$

Where  $CO_2$ ,  $CO$ ,  $O_2$  and  $HC$  were the concentrations of species with the same unit (only  $HC$  needed conversion from ppm to percentage with the relation ppm/10000).  $H_{CV}$  was the hydrogen to carbon ratio (equal to 1.73 for iso-octane),  $K$  the water gas equilibrium constant,  $K_1$  the flame ionization detector FID/NDIR conversion factor and  $O_{CV}$  the atomic ratio between oxygen and carbon. The non-dispersive infrared (NDIR) principle was used to measure  $CO_2$ ,  $CO$  and  $HC$ , instead, the electro-chemical principle for  $NO_x$  and  $O_2$ . The AVL system had an accuracy of  $\pm 3\%$  that increased up to  $\pm 5\%$  with the measured values.

During the tests was used iso-octane as a fuel, and the intake pressure was varied from 0.5 to 1 bar, to examine partial load and Wide-Open Throttle (WOT) conditions. The value of  $\lambda$  was modified from 1 (stoichiometric mixture) to 1.3 (lean mixture).

These parameters were regulated using a dedicated control system, the engine speed was set and a feedback control loop tried to keep constant by switching between the motor and generator mode of the electric machine.

The increasing or reducing of the Duration of Injection (DOI) was used to modify the air-fuel ratio, while the variation of intake pressure was obtained by acting on the opening level of the throttle valve. An absolute pressure sensor manufactured by Bosch, with an accuracy of  $\pm 1\%$ , was placed in the intake manifold for measuring the intake pressure, while the temperature was monitored by a thermocouple positioned in the intake manifold, his value is around 305K during all tests. The in-cylinder pressure was measured with an AVL GH12D transducer with an accuracy of  $\pm 1\%$  and a resolution of 0.2 CAD. This transducer was a piezoelectric pressure sensor, therefore, it used a quartz crystal to provide an electrical charge output under mechanical load. An average pressure trace of 200 cycles was used for thermodynamic analysis. The temperatures of oil and water were regulated by a thermal conditioning system that used a heat exchanger and an electric heater. This system ensured the correct thermal condition to protect the elongated piston-bore assembly.

In Figure 2.7 we can see two photos of the test rig.

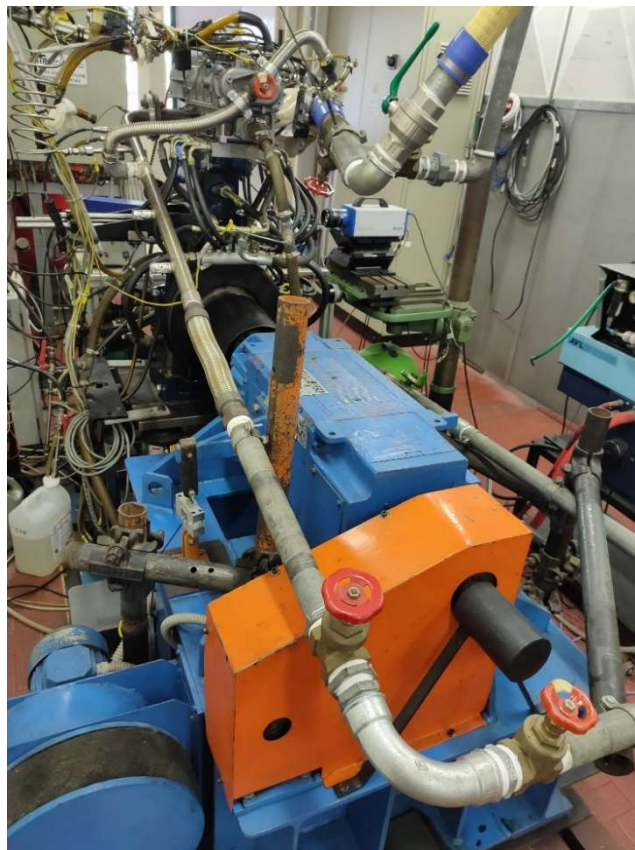
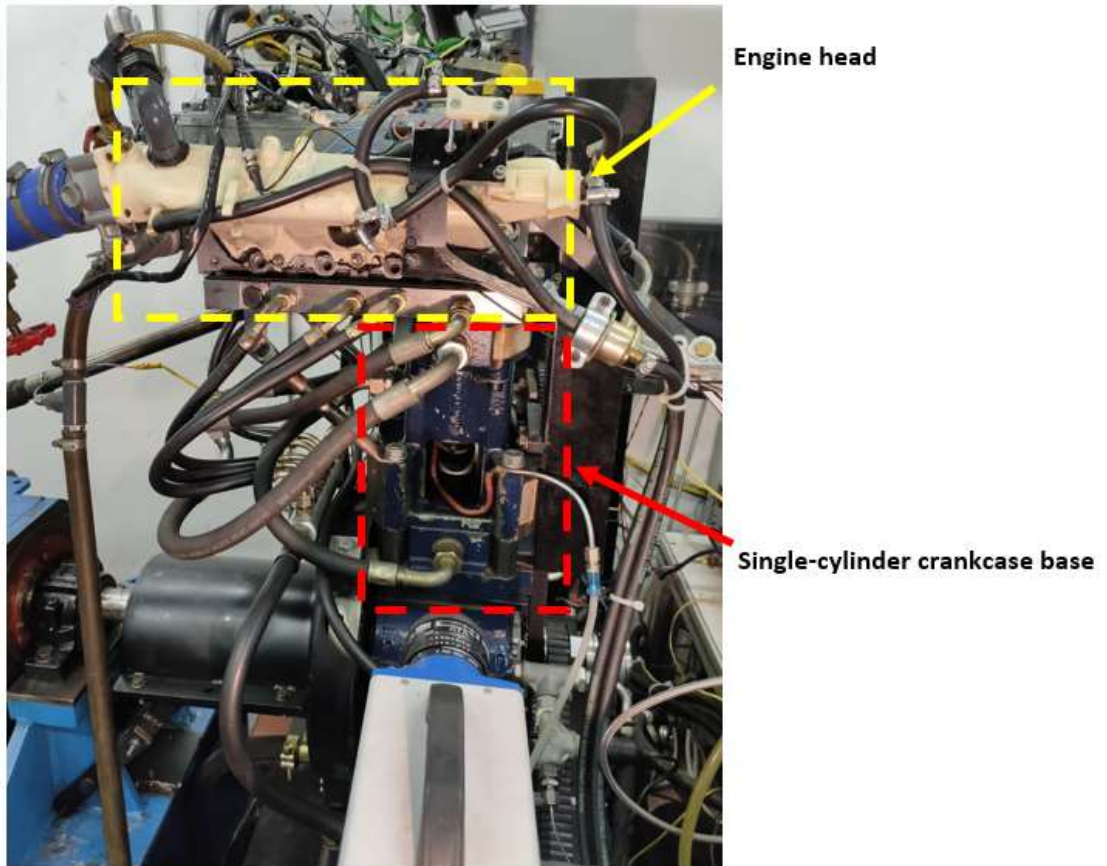


Figure 2.7 Test rig setup (top), Electric machine coupled with the engine (49.7 kW power, 230 Nm maximum torque)(bottom) from [6]

## 2.2 Procedure and Measurement Methodology for Thermodynamic Analysis

During the experimental tests were recorded different signals: intake pressure, in-cylinder pressure and equivalent ratio. A script built into NI LabView was used to analyse the signals, which returned the average of the 200 cycles with the steps described in the figure below (Figure 2.8).

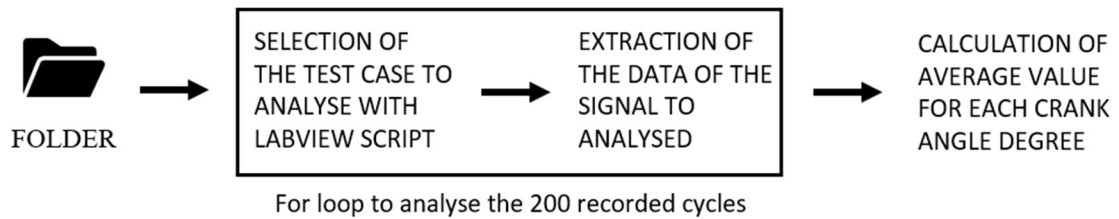


Figure 2.8 Description of LabView script.

After the calculation of the average value of in-cylinder pressure, it was necessary to equalize the value at 180 CAD BTDC to the value of the average intake pressure at the same angle (calculated in the same way as in-cylinder pressure). This correction was necessary because the in-cylinder pressure was calculated as an increment since it was measured with a piezo-electric transducer, then must be defined as a reference value which was the value of intake pressure. In thermodynamic analysis was compared the result of different values of spark plug orientation and type, and AFR to evaluate the effect of these parameters on CCV.

First of all, was calculated the Indicated Mean Effective Pressure (IMEP), but the cylinder volume was needed to perform these calculations, as a first step clearance volume was required, it was obtained with the Compression Ratio (CR) and displacement:

$$V_c = \frac{V_D}{(CR - 1)}$$

However, this equation did not take into account the variation of CR and the volume of crevices due to elongated piston, therefore, to verify the expansion level of components during the fired and motored cycle was carried out a thermal analysis on the engine. The relation below was used to compute for any crank angle degree the in-cylinder free volume:

$$V = V_c + \frac{\pi B^2}{4} \cdot (l + a - s)$$

where “l” was the connecting rod length, “B” the bore, “s” the distance between the piston axis and crank axis and “a” the crank radius. The value of “s” was calculated by:

$$s = a \cos \theta + (l^2 - a^2 \sin^2 \theta)^{\frac{1}{2}}$$

Figure 3.2 shows a schematic representation of the cylinder geometry.

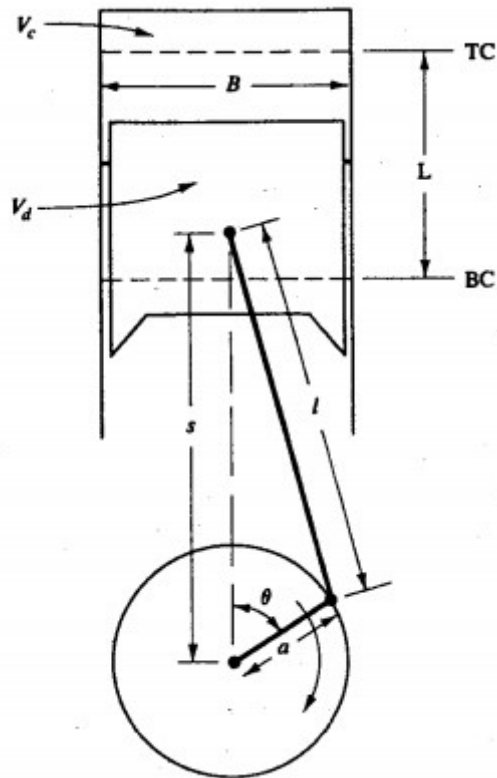


Figure 2.9 Representation of cylinder geometry from [14].

Therefore, with the available data it was possible to calculate the Indicated Work per Cycle ( $W_{c,i}$ ) for the 200 cycles with the relation:

$$W_{c,i} = \oint p dV$$

where “dV” was the instantaneous variation of volume and “p” the pressure in the cylinder measured in Pa. Then, the calculation of IMEP was now possible using the relation:

$$IMEP = \frac{W_{c,i}}{V_D}$$

where  $V_D$  was the displacement (data available in Table 2.1). With the value of IMEP for the 200 cycles was possible to evaluate the combustion stability with the calculation of  $COV_{IMEP}$ :

$$COV_{IMEP} = \frac{\sigma_{IMEP}}{\mu_{IMEP}} \cdot 100$$

where “ $\sigma_{IMEP}$ ” was the standard deviation of IMEP and “ $\mu_{IMEP}$ ” the average value of IMEP of the 200 cycles.

In the second part of the thermodynamic analysis was analysed the Mass Fraction Burned (MFB) but first of all, it was necessary to calculate the heat rate release using the first law of thermodynamics (single zone model):

$$dQ = \frac{\gamma}{\gamma - 1} \cdot p \cdot dV + \frac{1}{\gamma - 1} \cdot V \cdot dp$$

where Q was the net heat rate release in  $J/CAD$  (integral of heat rate release),  $\gamma$  the ratio of specific heat and was set to 1.35, p the in-cylinder pressure in Pa and V the instantaneous volume in  $m^3$ . The following relation allowed to compute the MFB:

$$MFB = \frac{Q_k - Q_{ST}}{Q_{EVO} - Q_{ST}}$$

where subscript “k” indicated the current crank angle, “ST” the spark timing crank angle and “EVO” the exhaust valve open crank angle.

Lastly, known the MFB trend it was possible to compute the CA value, i.e., the value of crank angle when a certain percentage of the mass of fuel was burned, CA5 was very important because indicated the first phase of combustion (flame development), CA50 was used to understand if the engine was worked close to Maximum Brake Torque (MBT).

## 2.3 Experimental Conditions

Table 5.1 shows the different operative conditions analysed during experimental tests, mainly a sweep of  $p_{INTAKE}$ , air-fuel ratio ( $\lambda$ ) and spark plug design and configuration.

To ensure comparable results from different tests was followed a procedure (because the measurements were performed in different sessions). First of all, was checked the intake temperature which was around 305K, indeed, to avoid the possibility to have an important

variation in ambient temperature (and consequently intake temperature) the tests were carried out in a small amount of days.

Engine Speed [rpm]	$p_{INTAKE}$ [bar]	$\lambda$	Spark Advance (SA) [CAD]	Spark plug Design	Spark plug orientation
1000	0.5	1.3	30	J - Type	Uniflow - Crossflow - Counterflow
				Double J-Type	Uniflow - Crossflow - Counterflow
		1.0	16	J - Type	Uniflow - Crossflow - Counterflow
				Double J-Type	Uniflow - Crossflow - Counterflow
	1.0 (WOT)	1.3	20	J - Type	Uniflow - Crossflow - Counterflow
				Double J-Type	Uniflow - Crossflow - Counterflow
		1.0	10	J - Type	Uniflow - Crossflow - Counterflow
				Double J-Type	Uniflow - Crossflow - Counterflow

Table 2.2 Experimental conditions

The second step was to monitor the temperature of the coolant system, particularly the temperature of input/output water-flow that were around 315-320K. Lastly, was continuously evaluated the condition of the piston seals to avoid the increase of blow-by leaks, indeed, during every test session were acquired motored cycles at the beginning and at the end of each session to evaluate if the peak pressure in motored condition was the same. A more detailed verification it was possible to evaluate the in-cylinder pressure at spark

timing for all configurations of the spark plug with the same  $\lambda$  and SA, Figure 2.10 shows the average pressure traces obtained from the LabView script, with the poorest mixture composition  $\lambda = 1.3$  and fixed Spark Advance of 20 CAD. The gap between the 5 pressure values at SA was around 0.1 bar, a negligible difference.

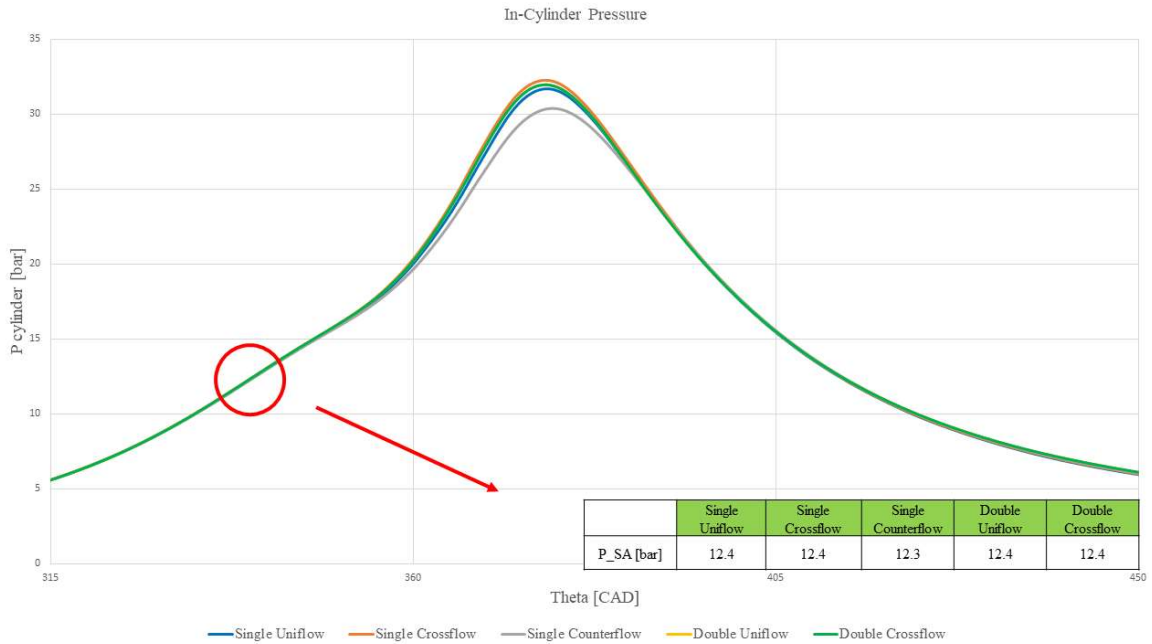


Figure 2.10 In-Cylinder Pressure with  $\lambda = 1.3$ , SA = 20 CAD and WOT conditions.

## 2.4 Thermodynamic Results

The report of the experimental tests is divided into 4 main cases, the first two sets of analysed cases were a partial load ( $p_{INTAKE} = 0.5 \text{ bar}$ ), and the first one used a lean mixture ( $\lambda = 1.3$ ), the second one was a stoichiometric test ( $\lambda = 1.0$ ). The last two sets of data were a WOT condition ( $p_{INTAKE} = 1 \text{ bar}$ ) with the two different air-fuel ratio values like the previous case. In this way, the differences between the various spark plug configurations with constant operating parameters were analysed in order to reduce influences.

### 2.4.1 Thermodynamic Results for Partial Load and Lean Mixture

( $p_{INTAKE} = 0.5 \text{ bar}$ ,  $\lambda = 1.3$ )

First of all was analysed the worst case, because the partial load decreased the tumble motion and the in-cylinder pressure at SA, moreover, the lean mixture led to slower combustion.

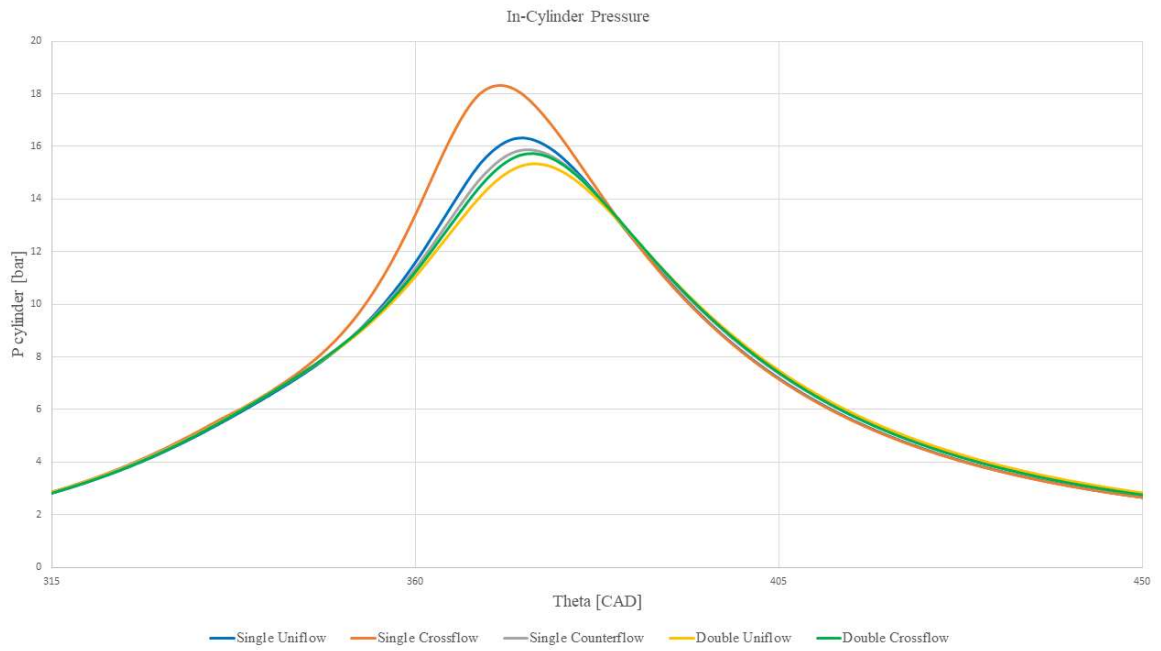


Figure 2.11 In-Cylinder Pressure with  $\lambda = 1.3$ ,  $SA = 30$  CAD and Partial Load.

Figure 2.11 shows the in-cylinder pressure, Single Crossflow allowed to obtain a higher peak of pressure with respect to other single electrode spark plugs but also to double electrode. Furthermore, Double Crossflow achieved a higher value of pressure than the Double Uniflow configuration. The high peak of the pressure of the Single Crossflow configuration was probably due to the exposure of the kernel to tumble motion which caused faster combustion. The differences between the various cases were very low (except for Single Crossflow), indeed, this trend was confirmed in IMEP values that were almost constant around 2.3 bar (Figure 2.12).

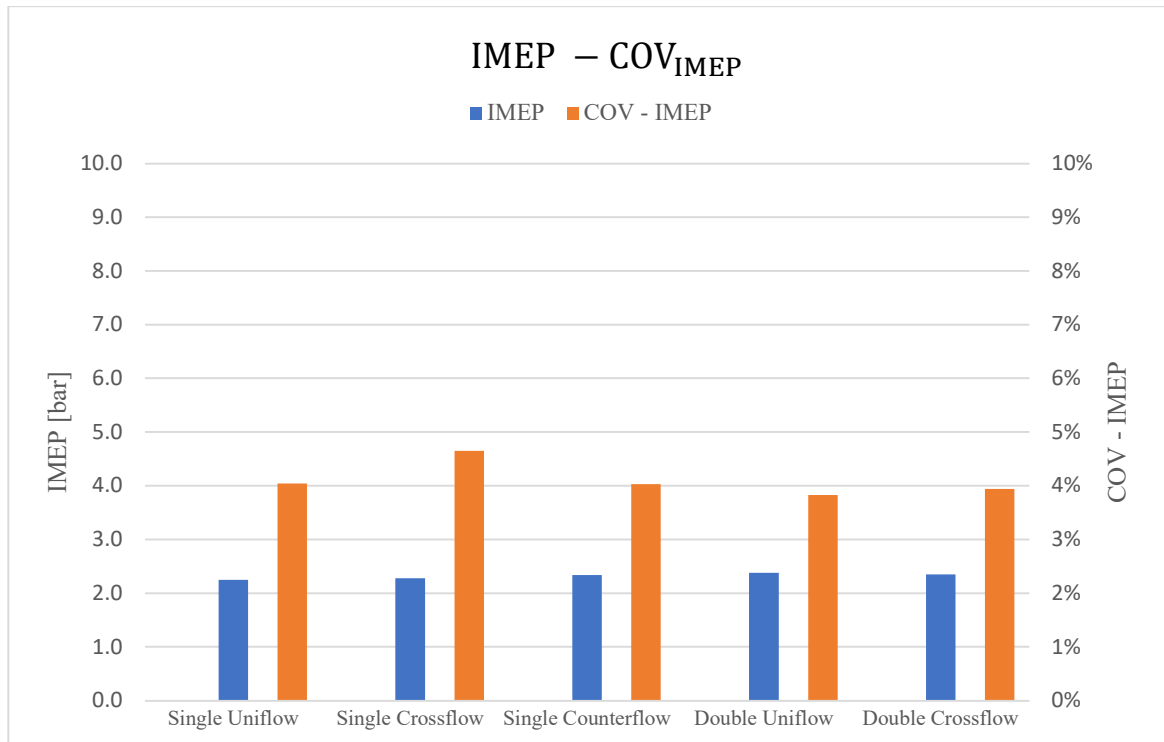


Figure 2.12 IMEP and  $COV_{IMEP}$  with  $\lambda = 1.3$ ,  $SA = 30$  CAD and Partial Load.

$COV_{IMEP}$  had the same values (4%) with all the configuration of spark plug, only Single Crossflow had a slightly higher value but lower than 5% that is the threshold to consider the combustion stable (Figure 2.12). Overall, the slower combustion due to lean mixture (characterized by longer chemical time scales) increase the interaction with tumble motion, then higher  $COV_{IMEP}$  values were expected. Single Uniflow and Double Uniflow allowed to obtain the best values in terms of Cycle-to-Cycle Variability (CCV) respectively for Single and Double type spark plugs, this was probably since the ground electrode acts as a “shield” for the tumble motion, thus, the formation of the kernel was more stable and the propagation of flame front faster. The higher peak of pressure for the Single Crossflow orientation was confirmed in Figure 5.4, furthermore, this orientation showed the lower  $COV_{P_{MAX}}$  which confirms the faster combustion in all cycles. The values of the peak of pressure variability, i.e.,  $COV_{P_{MAX}}$  were very higher than the  $COV_{IMEP}$ , these differences were mainly due to the fact that IMEP were integrated over 720 CAD.

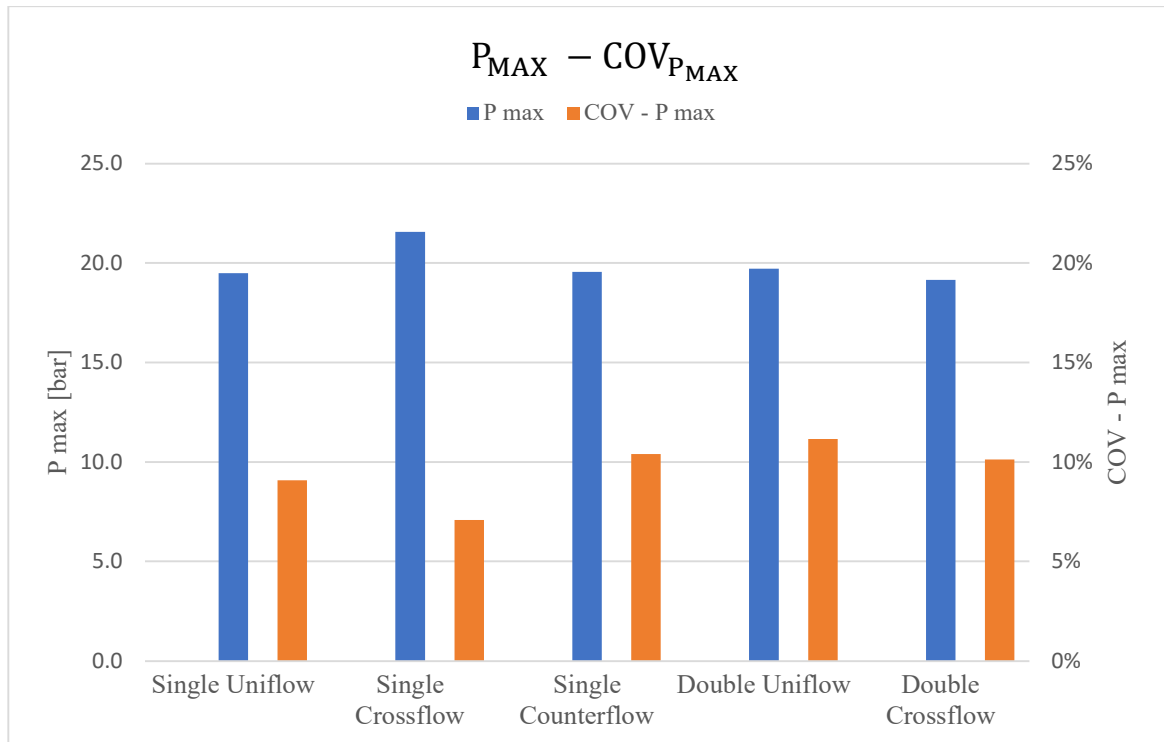


Figure 2.13  $P_{MAX}$  and  $COV_{P_{MAX}}$  with  $\lambda = 1.3$ ,  $SA = 30$  CAD and Partial Load.

The values of  $COV_{P_{MAX}}$  were around 10% with a peak of 11.2% for the Double Uniflow configuration while the lowest value was obtained with Single Crossflow (9%).

For the values of CA50 and CA5 were chosen the value of CA50 and CA5 for Single Uniflow as a reference, Figure 5.5 shows the variation of CA50 in all the configurations, this value was used to understand when the 50% of the mass of fuel was burned, and indicated the speed of burning. As expected from previous data analysed, the Single Crossflow configuration was the fastest burning with a CA50 1.5 CAD lower than the reference value, and vice-versa, Double Uniflow was the slowest combustion with the highest CA50 value (3.4 CAD higher than the reference value). Overall, the differences between the different configurations were very small.

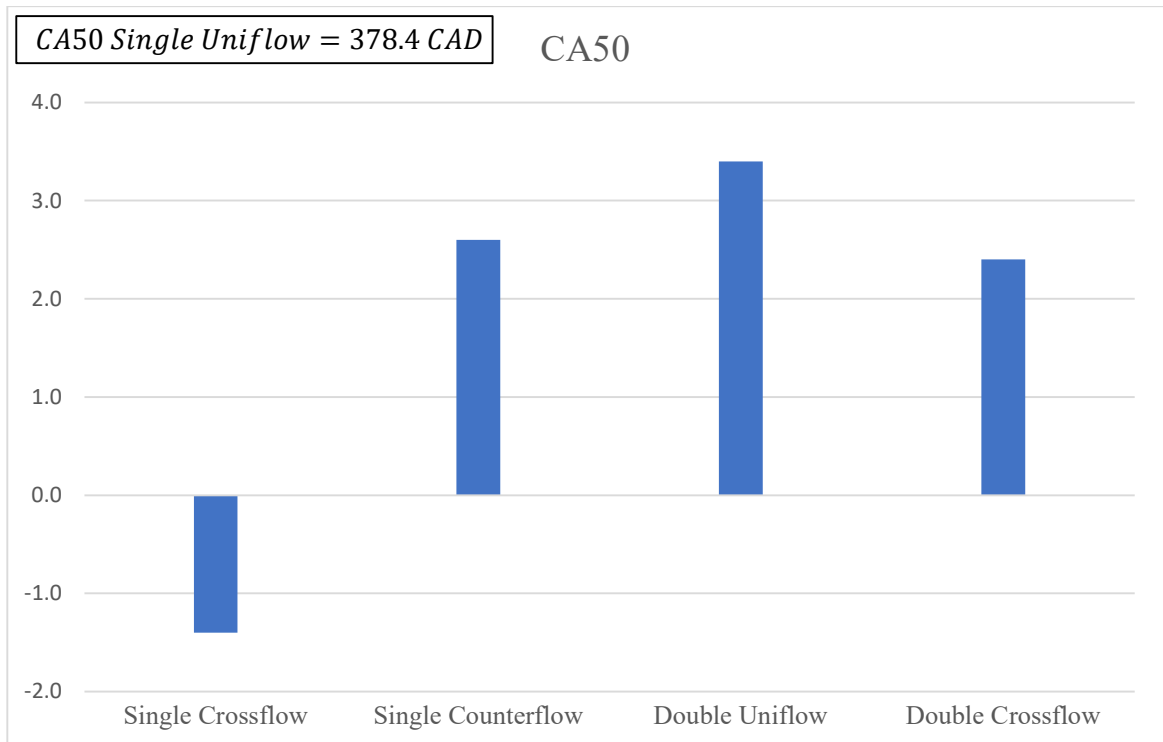


Figure 2.14 CA50 with  $\lambda = 1.3$ , SA = 30 CAD and Partial Load.

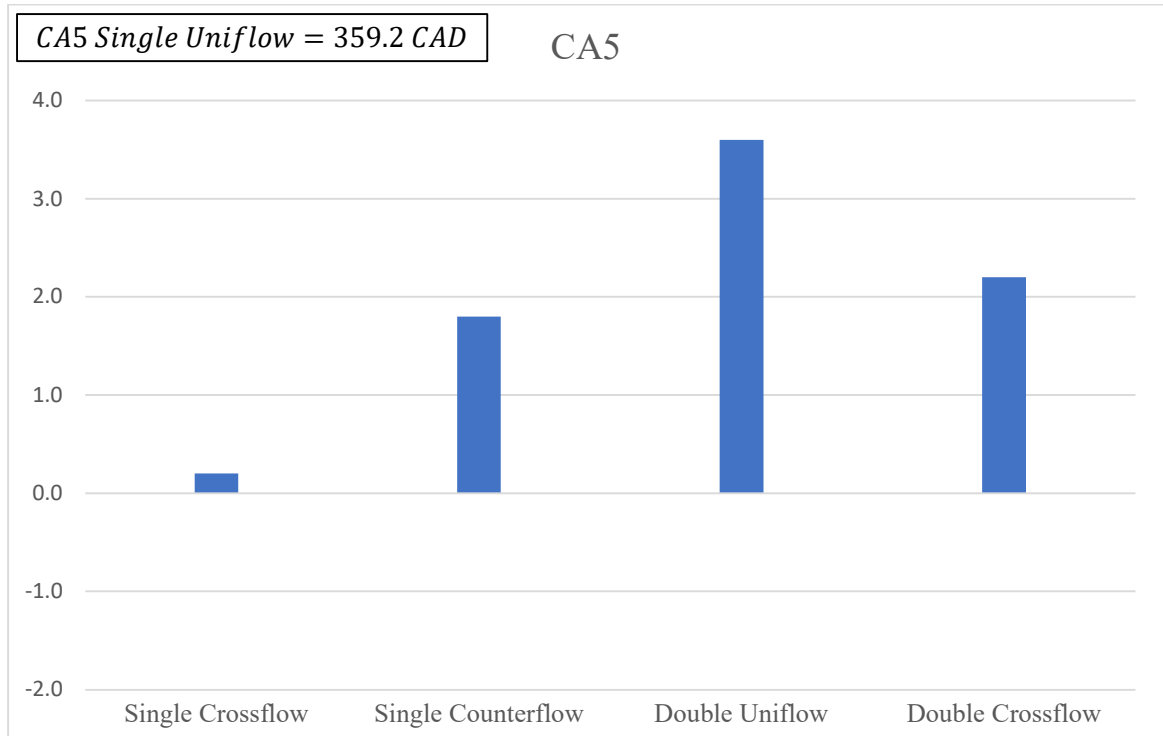


Figure 2.15 CA5 with  $\lambda = 1.3$ , SA = 30 CAD and Partial Load.

CA5 values were the angular position when 5% of the mass of the fuel was burned and indicated the speed of kernel development. The lower CA5 value was obtained with a Single

Uniflow configuration but the value of Single Crossflow was very close (only 0.2 CAD more); The Double Uniflow configuration was confirmed as the slowest combustion with a CA5 value of 3.6 CAD higher than the reference value as shown in Figure 2.15.

Overall, the Single Uniflow was the best type of spark plug for this operative condition, since it reached a good value of IMEP (2.25 bar) and a low value of  $COV_{IMEP}$  (4%) although higher than other configuration (Double Uniflow had the lowest value  $COV_{IMEP} = 3.8\%$ ) but allow to obtain a faster combustion, indeed, it reached CA5 first and the difference with the best CA50 was very small (only 1.4 CAD).

## 2.4.2 Thermodynamic Results for Partial Load and Stoichiometric Mixture ( $p_{INTAKE} = 0.5 \text{ bar}$ , $\lambda = 1.0$ )

This set of data was the second part of the partial load tests but with the stoichiometric air-fuel ratio, as expected the peaks of pressure were higher with respect to the previous case, looking to absolute value the peaks of pressure were around 17 bar.

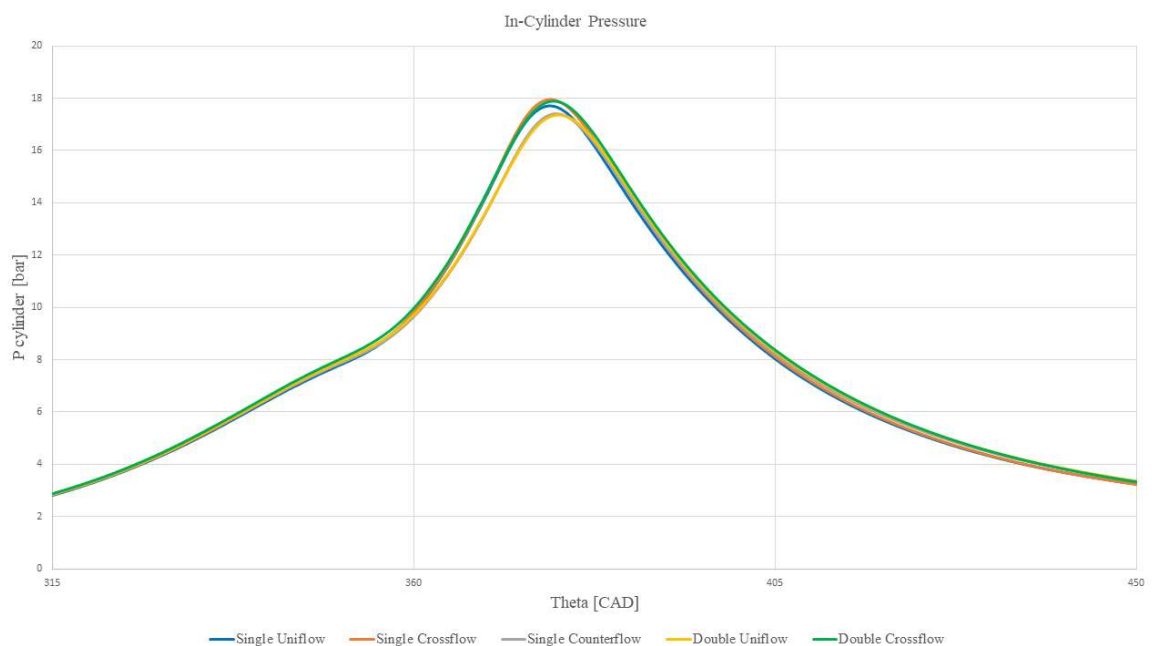


Figure 2.16 In-Cylinder Pressure with  $\lambda = 1.0$ ,  $SA = 16 \text{ CAD}$  and Partial Load.

Figure 2.16 shows the in-cylinder pressure traces of all spark plug configurations, like the previous case the Single Crossflow reached the highest peak of the average pressure but the Double Crossflow had almost the same trace and peak of pressure, besides, as the previous tests Double Uniflow showed the lowest value of pressure with Single Counterflow very close to it. Overall, the difference between the pressure was very small (less than 1 bar).

The values of IMEP were constant for all spark plug configurations around a value of 3 bar, Double Crossflow obtained the maximum absolute value (3.09 bar) and Single Uniflow the lowest value equal to 2.96 bar but the percentage difference between maximum and minimum values was only 4.2%. The maximum IMEP value was 29.8 % higher than the same value of the lean mixture test.

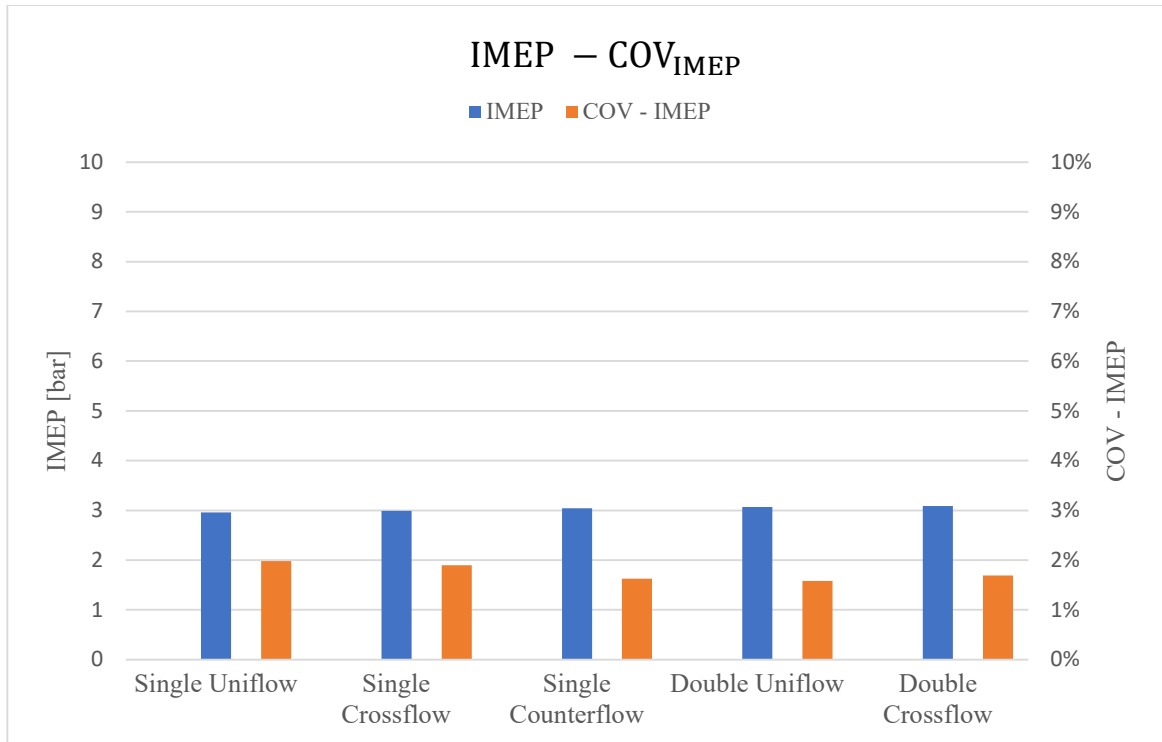


Figure 2.17 IMEP and  $COV_{IMEP}$  with  $\lambda = 1.0$ ,  $SA = 16$  CAD and Partial Load.

The main difference respect to the previous test was that the  $COV_{IMEP}$  values that were less than 2%, Double Uniflow allowed obtaining the best value (1.58%), unlike Single Uniflow which demonstrated the major variability with a  $COV_{IMEP} = 1.98\%$  (Figure 2.17). The very small differences between the 5 spark plug configurations were probably because the stoichiometric combustion was more stable and faster respect to the lean one, furthermore, the use of partial load ( $p_{INTAKE} = 0.5$ ) decreased the tumble flow into combustion chamber, then the orientation of electrode or the presence of double electrode demonstrated low influence on engine parameters.

The values of the pressure peaks were around 20 bar for all the configurations (Figure 2.19), as shown for the in-cylinder average pressure traces Double Crossflow reached the highest values (20.36 bar) while Double Uniflow and Single Counterflow the lower values, respectively 19.58 bar and 19.62 bar. These values were very similar to the previous

experimental case, moreover, the maximum peak of the pressure of the lean combustion was higher than the stoichiometric one (21.56 bar respect to 20.36 bar).

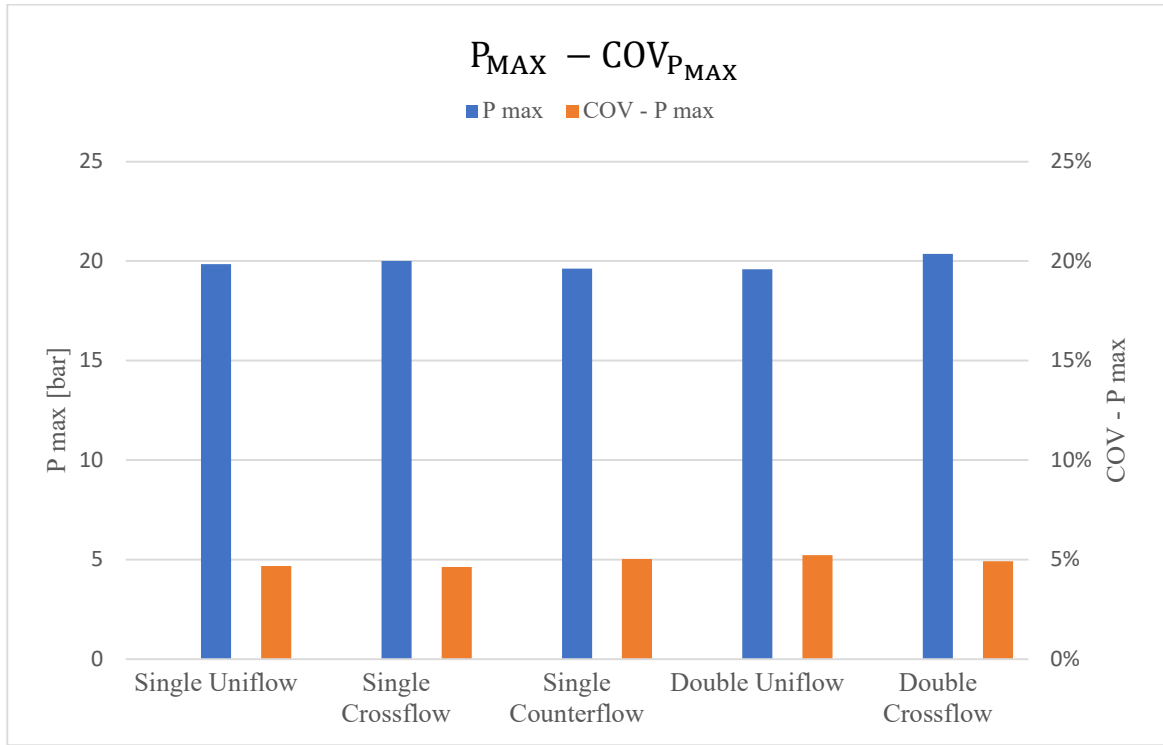


Figure 2.18  $P_{MAX}$  and  $COV_{P_{MAX}}$  with  $\lambda = 1.0$ ,  $SA = 16$  CAD and Partial Load.

The variability of the peak pressure for all test cases was around 5%, this value was half that of the previous case. The difference between  $COV_{P_{MAX}}$  values was very small, the best value was obtained with Single Crossflow configuration (4.63%), while the worse with Double Uniflow (5.21%) as shown in Figure 5.9. These low  $COV_{P_{MAX}}$  values demonstrate that all the 200 recorded cycles had a  $P_{MAX}$  close to the overall maximum value for each configuration.

As seen in the previous chapter, Figure 2.19 and 2.20 show the CA50 and CA5 values respect to the reference case which was Single Uniflow. In this test, the reference case and Single Crossflow allowed to obtain the fastest combustion, indeed they had the same CA50 value (378 CAD), instead, Double Uniflow showed the worse CA50 value equal to 380 CAD. These results confirmed the trend seen in the lean mixture tests.

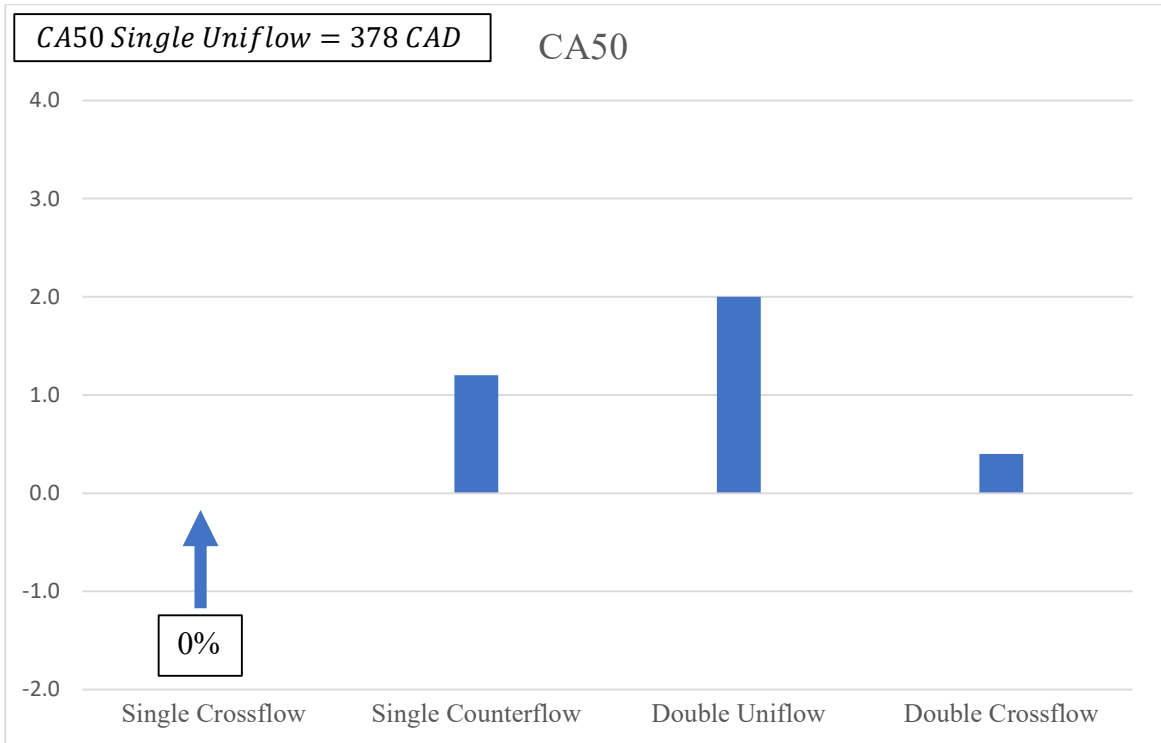


Figure 2.19 CA50 with  $\lambda = 1.0$ , SA = 16 CAD and Partial Load.

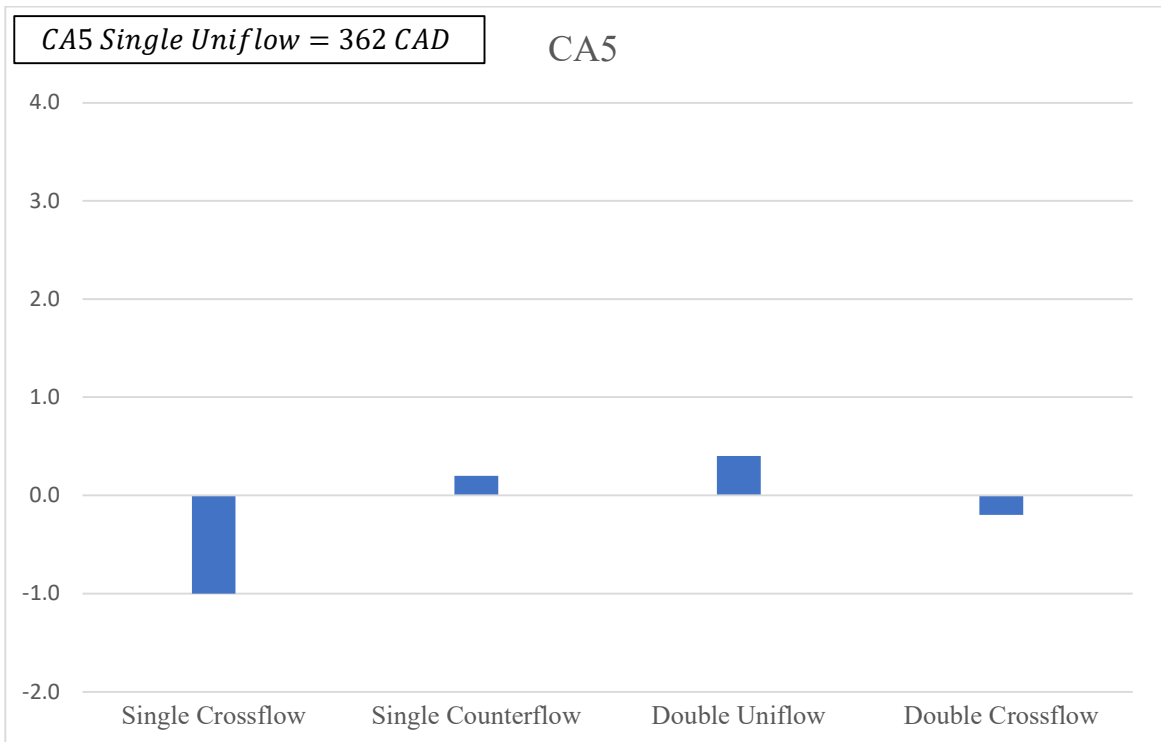


Figure 2.20 CA50 with  $\lambda = 1.0$ , SA = 16 CAD and Partial Load.

Looking at CA5, the faster kernel formation was reached with Single Crossflow, it had a CA5 = 361 CAD while the worse value was obtained with Double Uniflow (362.4 CAD).

In this case, the differences between the 5 spark plug configurations were smaller than in previous cases. Also in this experimental test, the Single Uniflow configuration had a good CA5 value like the previous test, then in terms of kernel formation and burning velocity, the Single Uniflow and Single Crossflow were alternatively the best configurations with partial load.

In conclusion, for this experimental test, with partial load and stoichiometric mixture, the best configuration of the spark plug was Double Crossflow because it ensured better values in terms of IMEP and  $P_{MAX}$ , a low Cycle-to-Cycle variability with a  $COV_{IMEP} = 1.69\%$  and  $COV_{P_{MAX}} = 4.91\%$ , and a fast combustion and kernel development, indeed, CA50 was only 0.4 CAD higher and CA5 0.2 CAD lower than the reference case.

### 2.4.3 Thermodynamic Results for WOT conditions and Lean Mixture ( $p_{INTAKE} = 1.0 \text{ bar}$ , $\lambda = 1.3$ )

The most important difference with the previous set of data was the WOT conditions, indeed the differences with the first experimental test reported were very important. In this experimental test was analysed lean combustion.

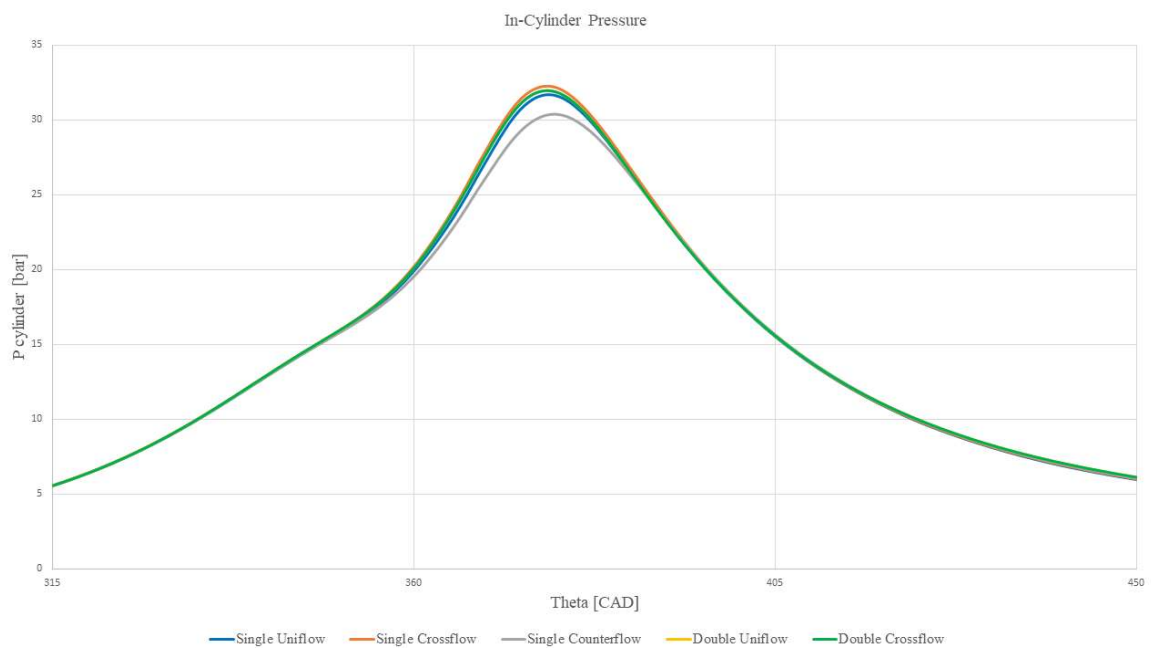


Figure 2.21 In-Cylinder Pressure with  $\lambda = 1.3$ ,  $SA = 20 \text{ CAD}$  and WOT conditions.

As shown in Figure 2.21 the peak pressure for all the configurations of spark plugs was around 32 bar, moreover, the values were very close except for the Single Counterflow which had a lower average peak pressure (30.4 bar). In this set is important to note that the two

orientations of the double electrode spark plug (Uniflow and Crossflow) had the same average in-cylinder pressure traces.

The IMEP values were around 6 bar and were almost constant, as we saw in Figure 2.22, the difference between the previous case, i.e., with partial load condition and lean mixture, was very important, and the maximum IMEP value of this set of data was 163% higher than the previous one. Returning to this experimental case, the Double Crossflow configuration reached the highest IMEP value equal to 6.26 bar while Single Uniflow obtained the worse result with a value of 6.15 bar, but the difference between these two values was very small, only 1.8%.

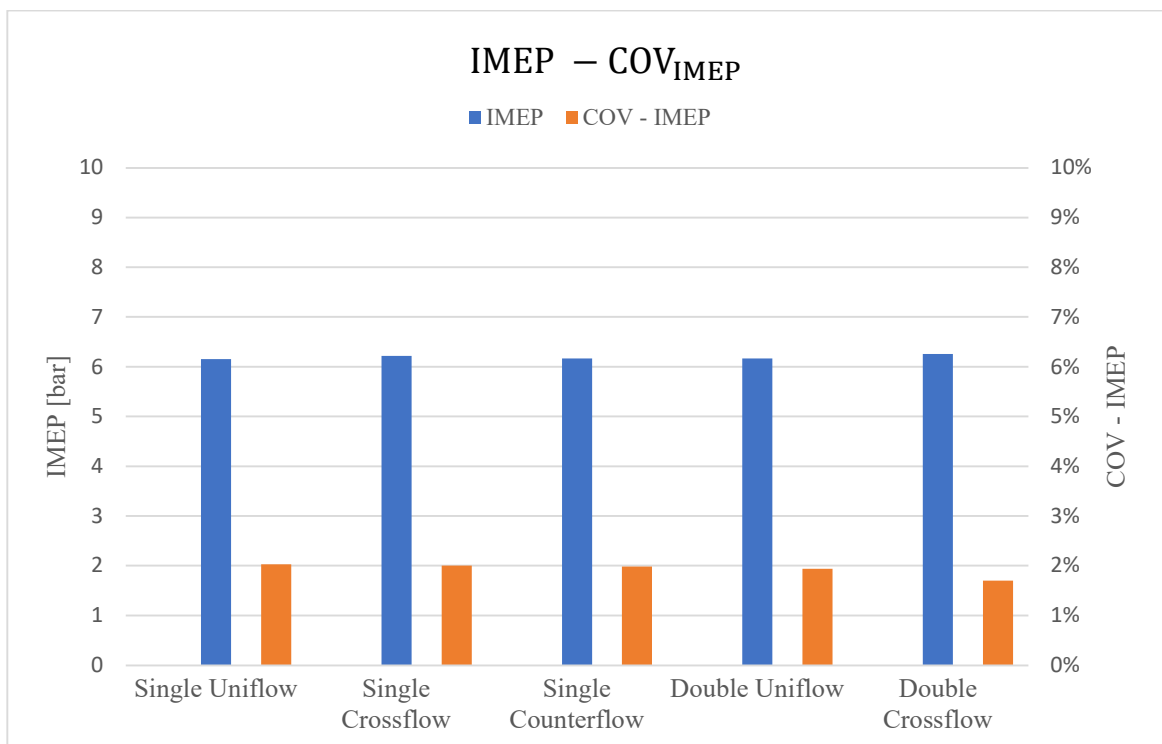


Figure 2.22 IMEP and  $COV_{IMEP}$  with  $\lambda = 1.3$ ,  $SA = 20$  CAD and WOT conditions.

The cyclic variability was very low with a  $COV_{IMEP}$  of around 2%, Double Crossflow had the lowest CCV while Single Uniflow had the highest CCV, respectively 1.7% and 2.03% of  $COV_{IMEP}$ , furthermore, the differences between the first 4 tests reported in Figure 2.22 were very small, only the Double Crossflow allowed to obtain a slightly low value. Probably this behaviour was since this configuration allowed a major interaction between the flame kernel and the tumble motion, which was permitted because the lean mixture had a longer chemical time scale. As expected from [15], the Double Crossflow configuration reached the highest peak pressure with a value of 39.9 bar, while the Single Counterflow had the lowest (37.9 bar), confirming the average in-cylinder pressure trend (Figure 2.23). The

$COV_{P_{MAX}}$  values were around 10% (Figure 2.23), and the trend of these values was similar to that seen in the previous lean combustion case, indeed, Single Crossflow showed the minimum variability of peak pressure (8.3%) and Double Uniflow (with Single Counterflow) had the highest value of  $COV_{P_{MAX}} = 10.6\%$ . These data confirmed that crossflow orientation increased the stability of the combustion with lean mixture.

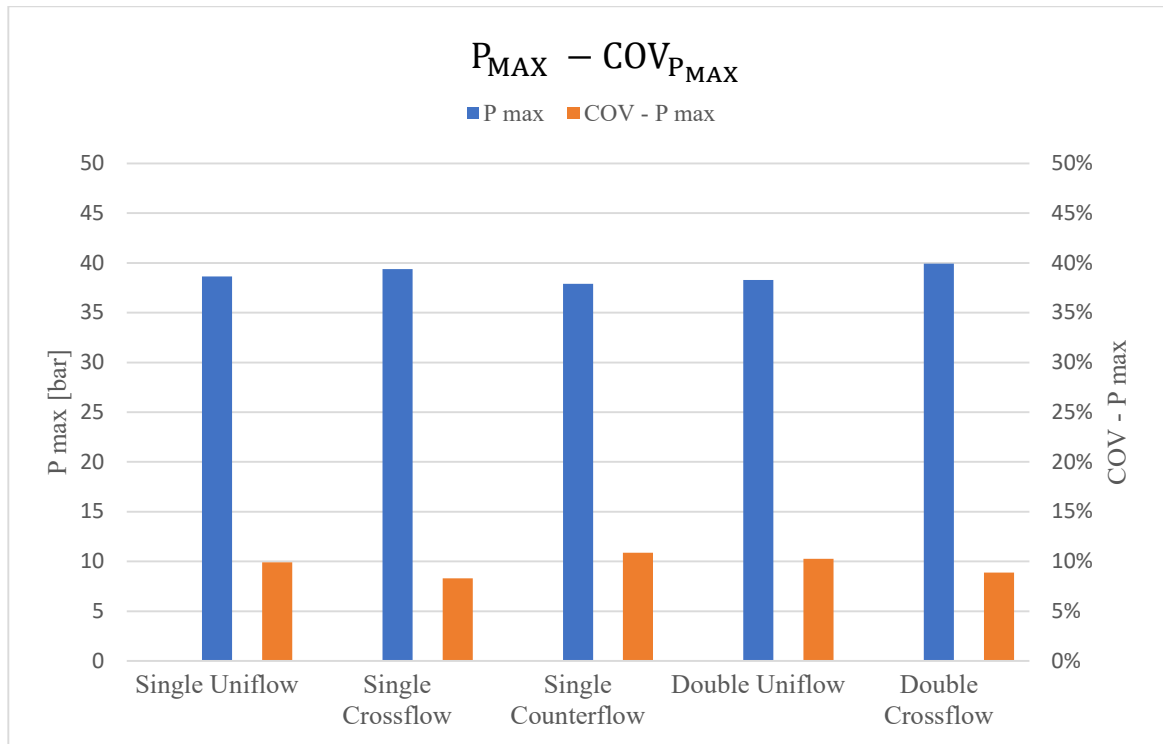


Figure 2.23  $P_{MAX}$  and  $COV_{P_{MAX}}$  with  $\lambda = 1.3$ ,  $SA = 20$  CAD and WOT conditions.

Figure 2.24 shows the values of CA50 for the different configurations as compared to the reference value, thus was 1.8 CAD lower than the reference value of the previous case, then overall the combustion was faster with the same air-fuel ratio, moreover, Single Crossflow and Double Crossflow had the same CA50 of reference which was the minimum value. In terms of CA50, Double Uniflow was the slowest burning configuration as seen also in the first experimental test ( $p_{INTAKE} = 0.5$  bar,  $\lambda = 1.3$ ).

Regarding the kernel development, the CA5 values, which indicated this first combustion stage, were reported in Figure 2.25, Single Uniflow permitted to obtain the slowest kernel formation with a  $CA5 = 359.8$  CAD while the worse value was reached with Double Uniflow configuration. Compared with the previous experimental test with a lean mixture, the duration of kernel development was almost the same, rather the formation was slower in these tests (359.8 CAD with respect to 359.2 CAD).

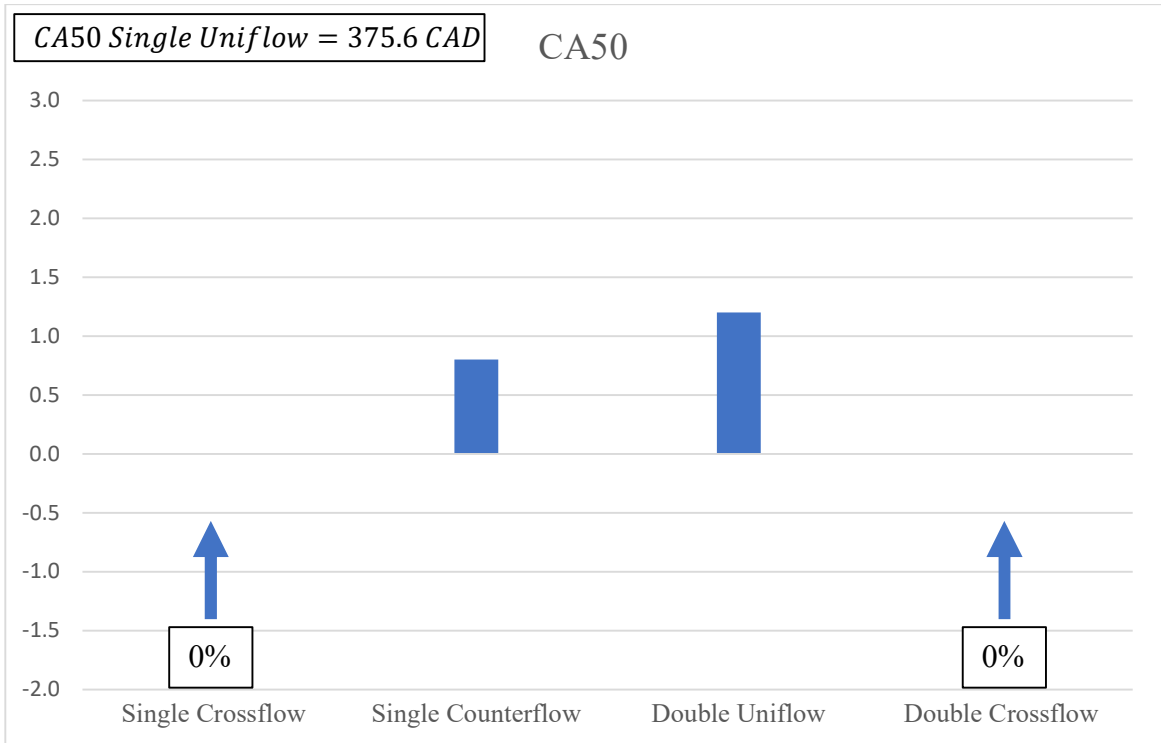


Figure 2.24 CA50 with  $\lambda = 1.3$ , SA = 20 CAD and WOT conditions.

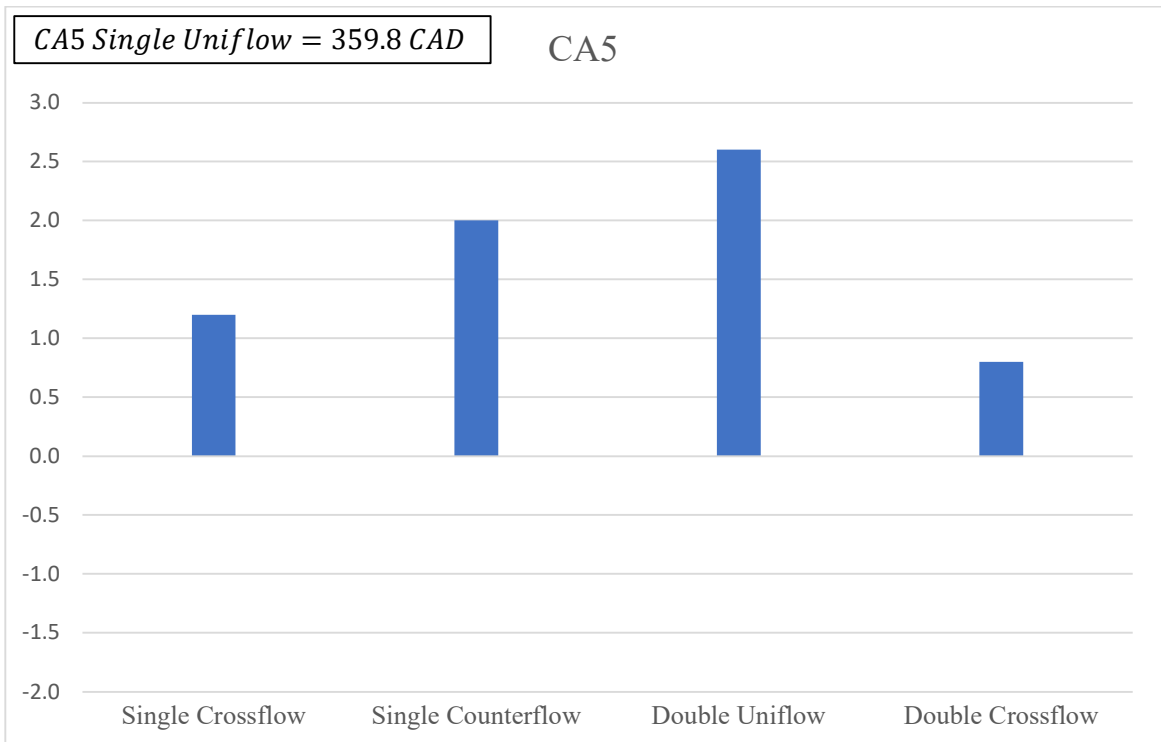


Figure 2.25 CA5 with  $\lambda = 1.3$ , SA = 20 CAD and WOT conditions.

Overall, with these experimental conditions Double Crossflow was the best configuration because demonstrated the highest value of IMEP and the lowest of  $COV_{IMEP}$ , respectively 6.26 bar and 1.7%, moreover allowed to obtain the maximum peak pressure (39.9 bar) with a low Cycle-to-Cycle Variability. In terms of combustion duration, this type of spark plug ensured the lowest burning duration with a  $CA50 = 375.6$  CAD and a good kernel development speed ( $CA5 = 360.6$  CAD).

#### 2.4.4 Thermodynamic Results for WOT conditions and Stoichiometric Mixture ( $p_{INTAKE} = 1.0$ bar, $\lambda = 1.0$ )

This last experimental case analysed a normal engine condition in full load (WOT) and with stoichiometric combustion.

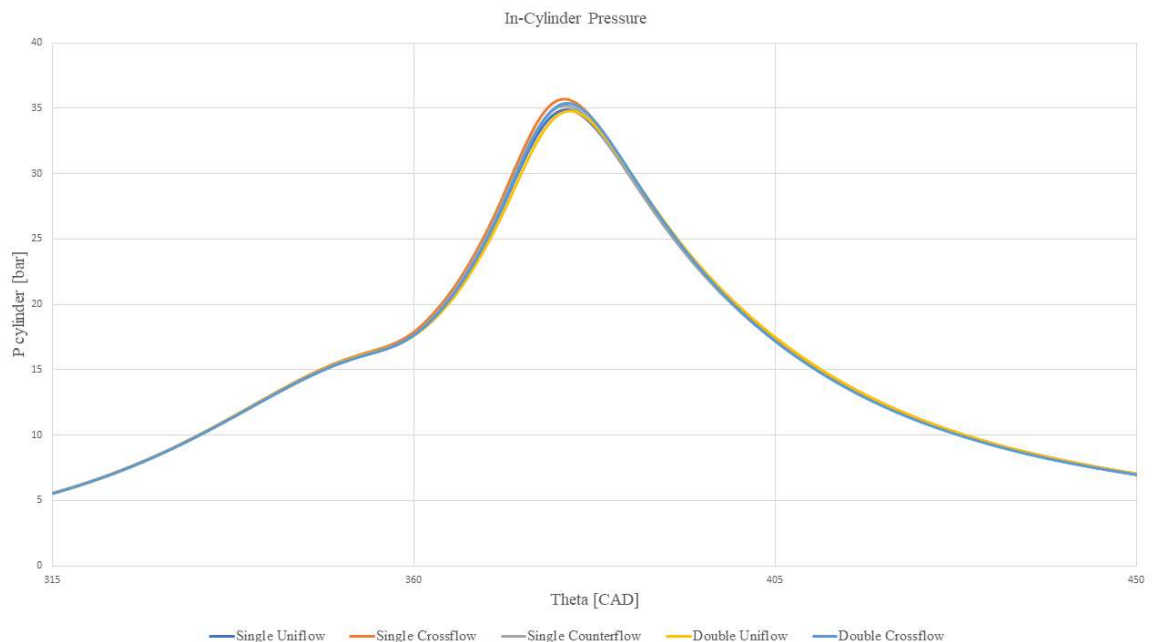


Figure 2.26 In-Cylinder Pressure with  $\lambda = 1.0$ ,  $SA = 10$  CAD and WOT conditions.

Figure 2.26 shows the in-cylinder average pressure traces, the peaks of pressure were around 35 bar, 8.6% higher than the previous test with  $\lambda = 1.3$ . Single Crossflow reached the maximum value while Double Uniflow the minimum, respectively 35.7 bar and 34.8 bar, as seen the difference between all the spark plug configurations was very small, only 2.6%. It's important to note that, with respect to other experimental cases, the trace of pressure had an almost constant value before the TDC, this was because the Spark Advance (SA) was only 10 CAD BTDC, then, as demonstrated with the computation of CA5, the combustion phase start after TDC. This phenomenon did not occur in the previous tests because the SA was higher.

As shown in Figure 2.27 the IMEP values were approximately 7.5 bar, Single Crossflow allowed to obtain the highest value (7.56 bar) while the Single Uniflow the lowest (7.45 bar) but the difference was low. Obviously, the IMEP was higher than the lean combustion case and the partial load case (Chapter 4.2.2 and 4.2.3), looking at the comparison with the previous lean burning case the value was increased by 20%. The counterflow orientation was the best with either type of spark plug (Single and Double J-electrode) as shown also with lean burning and WOT conditions.

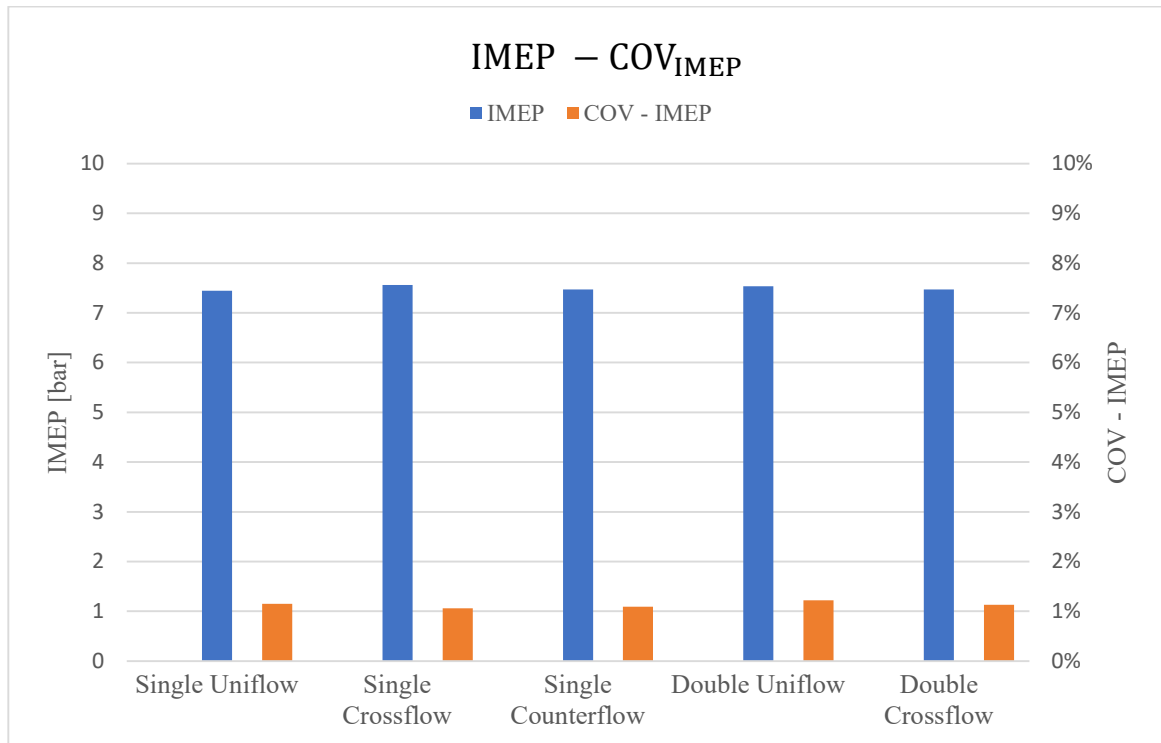


Figure 2.27 IMEP and  $COV_{IMEP}$  with  $\lambda = 1.0$ ,  $SA = 10$  CAD and WOT conditions.

These experimental tests allowed us to obtain the lowest  $COV_{IMEP}$  values as expected, the CCV was very low with values slightly over 1%, Single Crossflow reached the minimum  $COV_{IMEP} = 1.06\%$ , instead, the highest CCV was obtained with Double Uniflow configuration that showed a value of  $COV_{IMEP} = 1.22\%$ . Analysing the previous full load case, it was observed that the  $COV_{IMEP}$  differences were important, instead, the minimum value of  $COV_{IMEP}$  in the previous test was 60% higher than the lowest value in this case. Figure 2.28 shows the  $P_{MAX}$  and  $COV_{P_{MAX}}$ , the values of  $P_{MAX}$  were around 40 bar, respect to lean burning this value was 3% higher the previous one. Single Crossflow shows the highest peak pressure (40.6 bar), as shown the in-cylinder average pressure analysis. The lowest values, obtained with Single Counterflow configuration, was 2.7% lower than highest one.

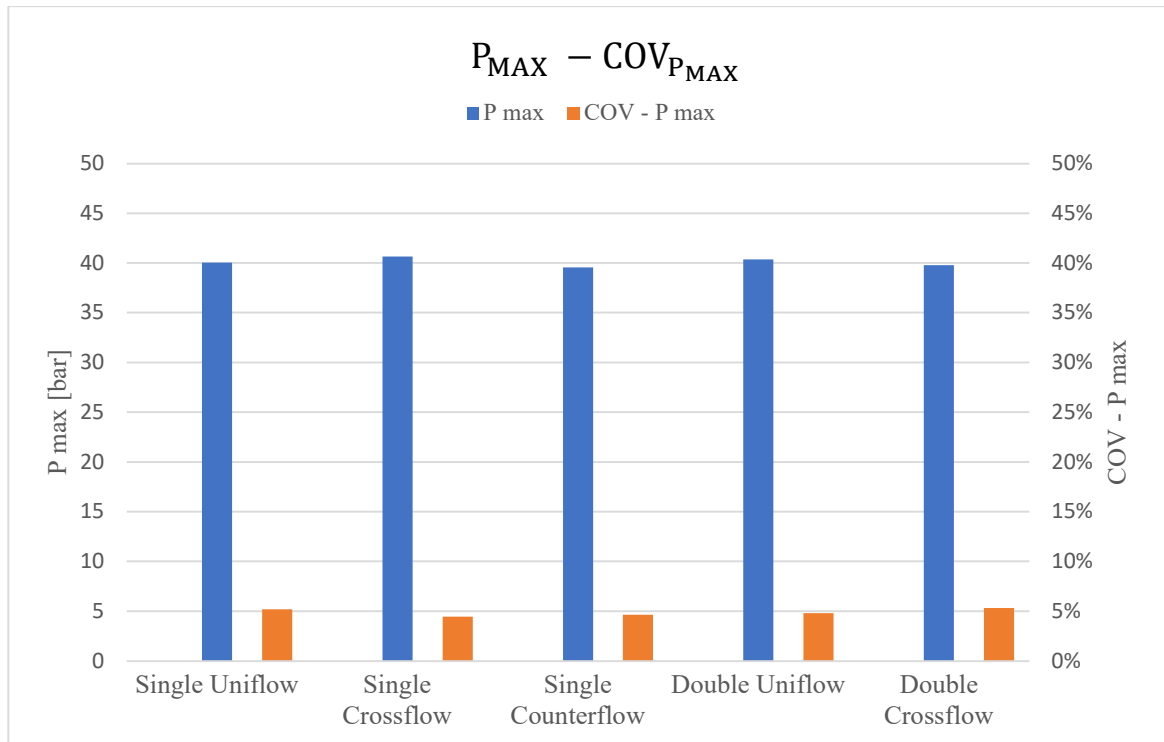


Figure 2.28  $P_{MAX}$  and  $COV_{P_{MAX}}$  with  $\lambda = 1.0$ ,  $SA = 10$  CAD and WOT conditions.

Also,  $COV_{P_{MAX}}$  values were the lowest observed in all the experimental tests analysed in this work, the values were around 5%, the minimum value (4.45%) was obtained with Single Crossflow configuration, while Double Crossflow allowed to obtain the worst value (5.32%). Compared with the previous experimental test, the best  $COV_{P_{MAX}}$  value was 86% higher than the highest in this case.

As anticipated, the values of CA50, shown in Figure 2.29, were higher than the same values of the lean burning case, but the differences were very small, indeed, the lowest CA50 value of these tests was 376 CAD, thus only 1 CAD higher than the previous case, and was obtained with Single Counterflow while Double Uniflow reached the lowest values (378.2 CAD), thus this configuration of the spark plug was the worse, in terms of combustion duration, in both cases, thus with the lean and stoichiometric mixture and with a full load.

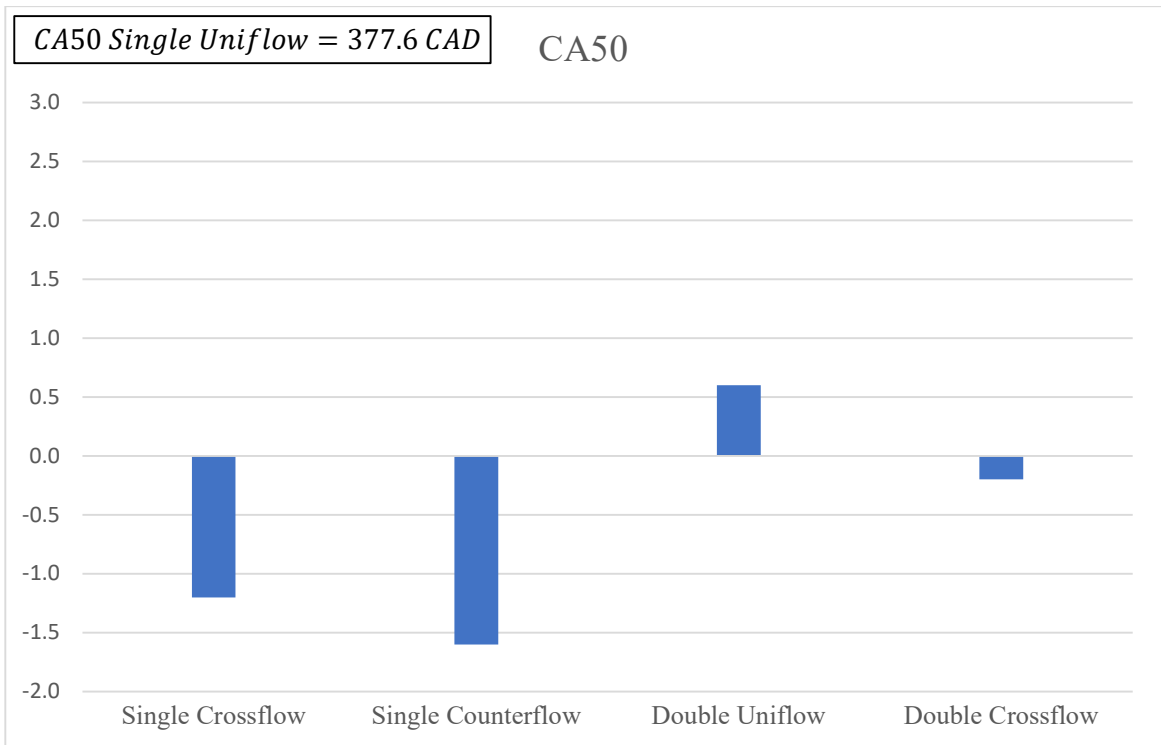


Figure 2.29 CA50 with  $\lambda = 1.0$ , SA = 10 CAD and WOT conditions.

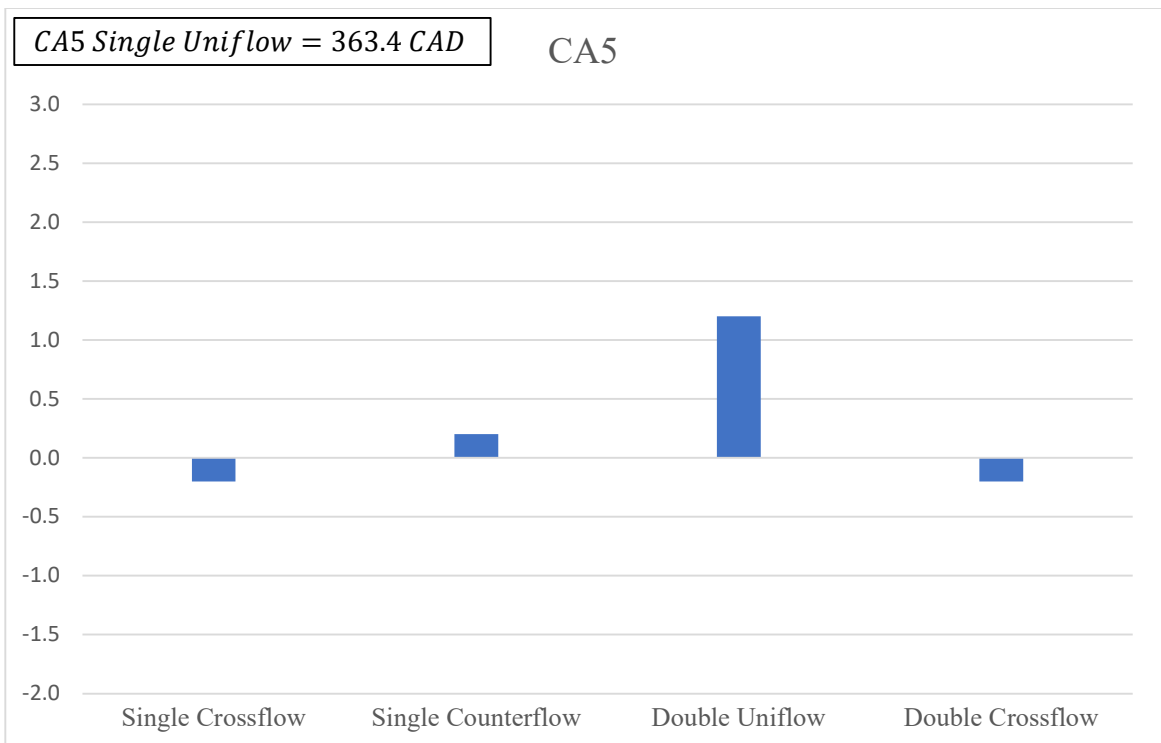


Figure 2.30 CA5 with  $\lambda = 1.0$ , SA = 10 CAD and WOT conditions.

As shown in Figure 2.30, Single and Double spark plugs in Crossflow orientation obtained the fastest kernel development with a  $CA5 = 363.2$  CAD, which was 3.4 CAD higher than the lean mixture case. The slowest kernel formation was obtained, as in the previous case, with Double Uniflow with a value of 364.6 CAD. Compared to the previous case with the stoichiometric mixture (Chapter 4.2.2), the  $CA5$  was 2.2 CAD lower than this test, this difference was probably due to the values of  $SA$  that was 16 CAD in the previous case with respect to 10 CAD in this one.

In conclusion, Single Crossflow was the best spark plug configuration for this experimental test, because obtained the best  $IMEP$  and  $COV_{IMEP}$  values, the same with  $P_{MAX}$  and  $COV_{P_{MAX}}$ . Regarding the duration of combustion, this spark plug obtained the faster kernel development with a  $CA5 = 363.2$  CAD and a good value of  $CA50$  equal to 376.4 CAD which was only 0.4 CAD higher than the lowest value.

## 3. 3-D CFD Simulation Analysis

The second part of this work was focused on a 3-D CFD Simulation of the engine used for the experimental tests. This phase was divided into two parts, the first one simulated the engine cycle without combustion, called cold cycle, in the second part was considered also the combustion. The cold cycle simulation was fundamental to set up properly the simulation model (e.g. boundary, valve lift, initialization) because allowed to compare simulation results and experimental data excluding the combustion parameters, the comparison of the results was possible thanks to an experimental cold cycle performed at CNR-STEMS, in particular, with this simulation was possible to verify the intake and exhaust air mass flow, which depended on both boundary conditions and valves timing and lift; the air mass flow influenced the in-cylinder mass and thus the in-cylinder pressure trace.

### 3.1 Simulation Setup

First of all, the simulation time parameter was set, for this model, for both the cold cycle and firing cycle, the simulation start time was  $567^{\circ}\text{CAD}$  before the TDC firing while it finished at  $120^{\circ}\text{CAD}$  after the TDC firing, therefore was not simulated the full cycle ( $720^{\circ}\text{CAD}$ ). In the simulation, the TDC firing was at  $0^{\circ}\text{CAD}$  and started during the exhaust stroke, this initial phase was used to reach the convergence of the parameters related to pressure, temperature, mass etc., and then the simulation domain was prepared to simulate the intake and compression stroke.

#### 3.1.1 Geometry Preparation

The first step of the simulation was the import of the triangulated surface in Converge, in this case, the surface was exported from the CAD program (i.e. Solidworks) in .stl format (Figure 3.1-3.2).

After that, the next step was to repair the geometry defects, which were highlighted in the Diagnosis dock and could pervert the running of the simulation. There were different types of defects: intersection, normal orientation, nonmanifold edges, open edges, overlapping triangles, small area, aspect ratio and small angle; the first four are considered an error and impeded the simulation running, and the others are classified as a warning and could cause errors in solution results.

The second step of the surface preparation was the separation into different areas, called boundaries, which allowed for the assignment of different boundary types and initial

conditions, to flag the boundary, the boundary fences, i.e. virtual borders, were used, and these allowed to assign the different areas to a boundary.

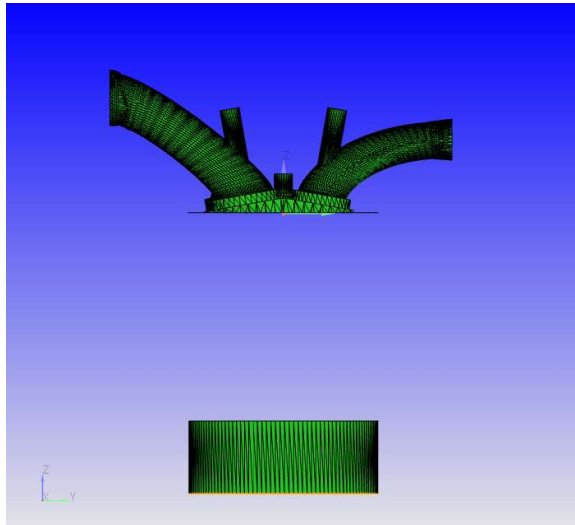


*Figure 3.1 Frontal view of engine surface.*

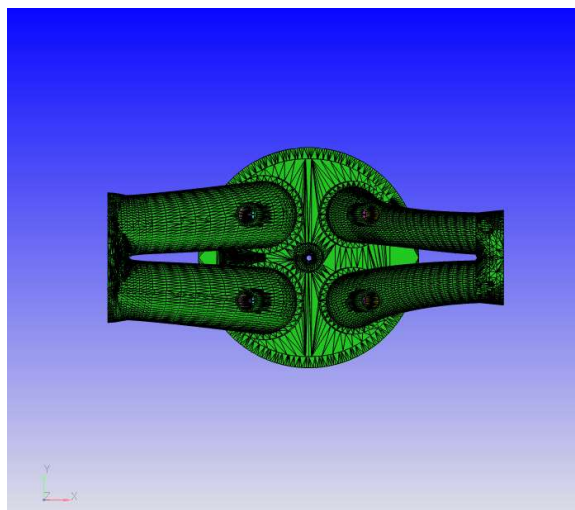


*Figure 3.2 Top view of engine surface.*

After that, was possible to prepare the piston and liner for motion, in this particular research engine was necessary to consider the crevices between piston and cylinder because the piston bore was 78.4 mm while, as reported in Chapter 2.1, the cylinder bore was 79 mm, then a cylindric volume was added under the piston and the surface was closed with a circular crown which allowed to create a cylindrical surface of the liner without irregularity.

Another important step was the preparation of valve motion, indeed, Converge created disconnected triangles to simulate the closed valve because the intersections were not possible, to help the creation of these triangles the valve seats were modified to avoid sharp edges, and the seats were divided into two parts, the first one had almost the same angle of the valve angle, the second one connected the previous with the head as shown in Figure 3.3.

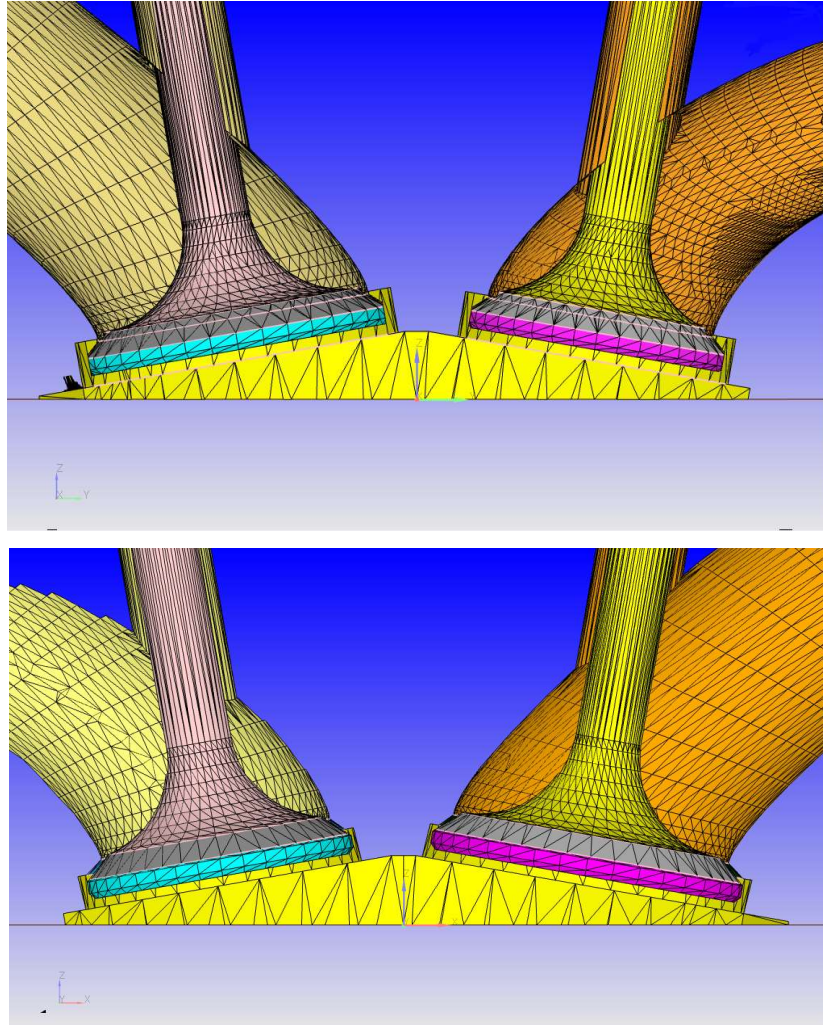


*Figure 3.3 Original valve seat (top), Modified valve seat (bottom).*

After the modification of the valve seat, the valves were translated, along the valve stem axis, to reach the correct distance from the seat when starting the valve motion, called minimum lift, i.e. 0.2 mm for both intake and exhaust valves; moreover, in the boundary menu, the minimum lift value and the valves lift were set. As shown in Figure 3.4 the valves were divided into top, angle and bottom. Lastly, the presence of errors was checked with the diagnosis tool, after this control the simulation model was ready to set up.

### 3.1 Cold Cycle Setup

#### 3.2.1 Boundary Setup

The next step was setting up the correct boundary conditions for each boundary defined earlier, this phase was very crucial because the conditions and the location of the boundary applied constraints to the transport equations. There are many types of boundaries but in this thesis was used only three: WALL boundary, INFLOW boundary and OUTFLOW boundary.

First of all, was set the WALL type boundaries, and to this category appertained all the boundaries except those marked with ID 4 and 5; some of these surfaces could translate, the boundaries marked with ID 13, 15 and 18 were the parts of intake valves, the ID 11, 12 and 13 belonged to exhaust valves, while boundary with ID 1 was the piston, the other boundaries were stationary. The moving boundaries needed a motion profile, in the case of the piston it was possible to flag the piston motion button; for the valves were necessary to import the correct valve lift (Figure 3.5).

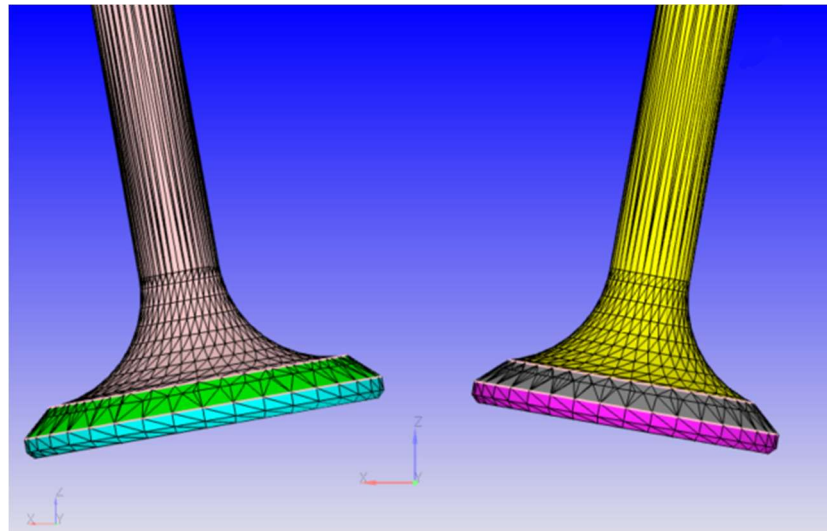


Figure 3.4 Intake valve (left), Exhaust valve (right).

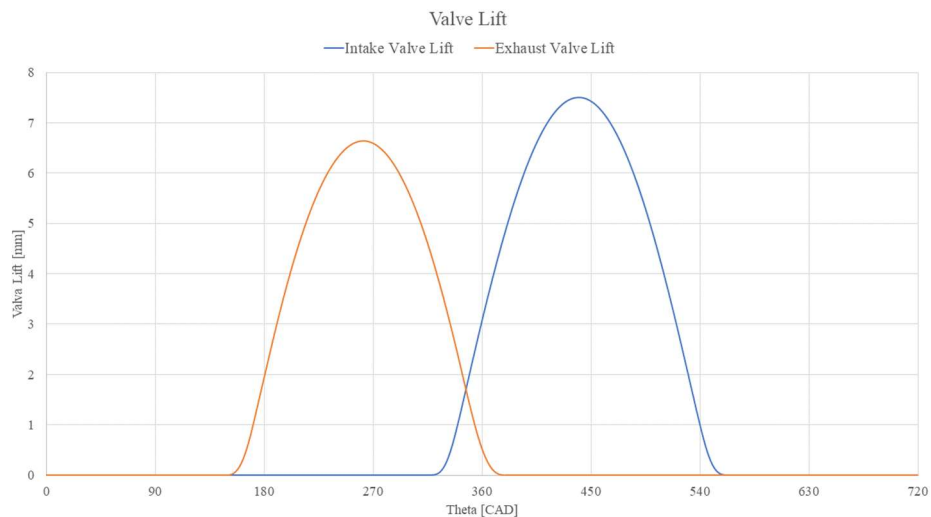


Figure 3.5 Intake and exhaust valve lift profile.

For all the WALL boundaries was set the initialization temperatures, as reported in Table 3.1, furthermore, the *Law of wall* condition type was imposed for both temperature and velocity boundary conditions. This condition is a logarithmic fit of a turbulent boundary layer, appropriate for high Reynolds number turbulent flows, in which the viscous substrate is not resolved.

ID	Boundary Name	Temperature [K]
1	Piston	380
2	Intake Port	310
3	Exhaust Port	320
6	Head	370
7	Injector	370
8	Injector Nozzle	370
9	Spark Plug	370
10	Spark Plug Electrode	370
11	Exhaust Valve Bottom	360
12	Exhaust Valve Angle	360
13	Exhaust Valve Top	360
14	Intake Valve Angle	340
15	Intake Valve Bottom	340
16	Intake Valve Top	340
17	Liner	360
18	Intake Port Angle	310
19	Exhaust Port Angle	320

Table 3.1 Initialization temperature for WALL boundaries for cold cycle.

The other two boundaries were INFLOW (Figure 3.6 (a)) and OUTFLOW (Figure 3.6 (b)), these defined the flow which goes in and out of the domain. The configuration of these boundaries was necessary to impose the pressure and temperature, for both the Dirichlet boundary conditions were set. An important difference between INFLOW and OUTFLOW was the imposed pressure, indeed, in the INFLOW boundary was imposed the static pressure and temperature, as suggested in Converge's manual, with these values the program calculated the static pressure and temperature with the formulas below (3.1 and 3.2).

$$P_{static} = P_{total} \left( 1 + \frac{\gamma-1}{2} \frac{u_i^2}{\gamma RT} \right)^{\frac{\gamma}{\gamma-1}} \quad (3.1)$$

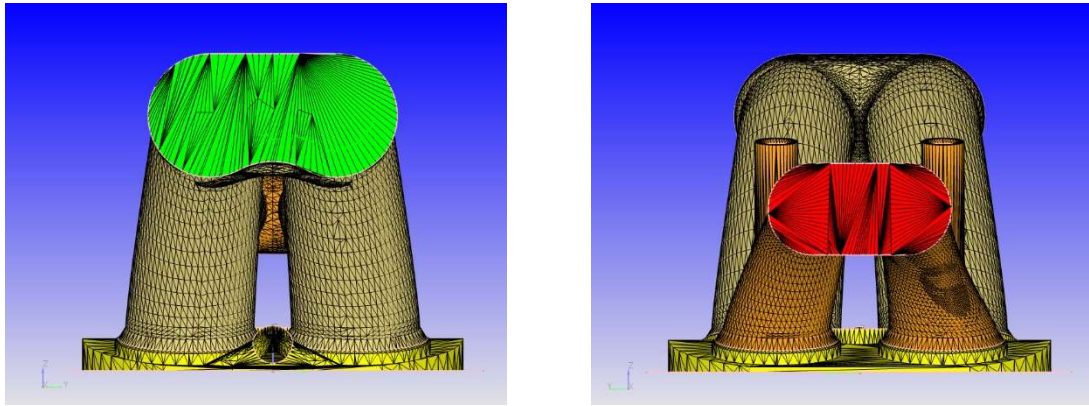
where:

- $\gamma$  is the specific heat ratio;
- $R$  is the constant of gas.

For the static pressure the formula is similar:

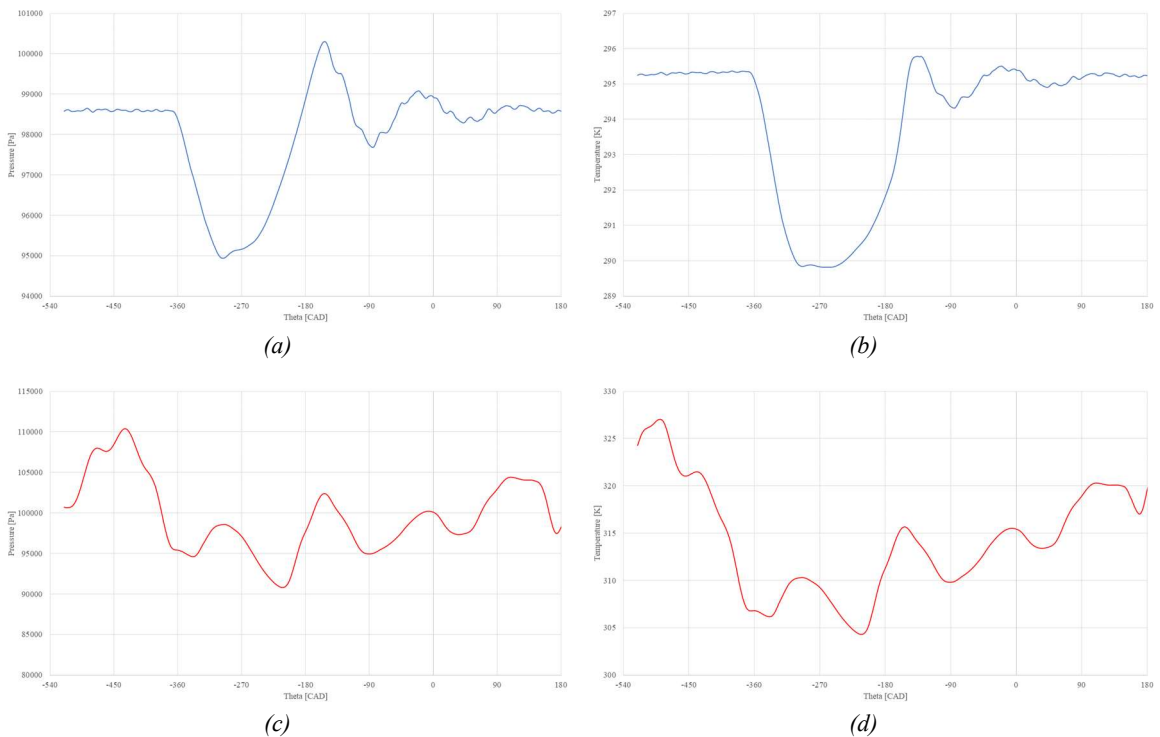
$$T_{static} = T_{total} \left( 1 + \frac{\gamma-1}{2} \frac{u_i^2}{\gamma RT} \right)^{-1} \quad (3.2)$$

The Neumann velocity condition was calculated with these two calculated conditions. For the OUTFLOW boundary were imposed the same conditions option but was used the static pressure and temperature. In this case, the INFLOW and OUTFLOW boundary conditions were imported from the previously validated GT-Power model, Figure 3.7 shows the pressure and temperature of inflow and outflow as a function of crank angle.



(a) (b)

Figure 3.6 (a) Inflow boundary (green), (b) Outflow boundary (red).



(a) (b) (c) (d)

Figure 3.7 (a) Total intake pressure, (b) Total intake temperature, (c) Static exhaust pressure, (d) Static exhaust temperature of cold cycle.

Lastly, the values of the turbulent dissipation  $\varepsilon$  and turbulent kinetic energy  $k$  were necessary for the OUTFLOW and INFLOW boundaries. The turbulent dissipation rate  $\varepsilon$  was calculated as:

$$\varepsilon = \frac{c_{\mu}^{3/4} k^{3/2}}{lengthscal} \quad (3.3)$$

where:

- $c_{\mu}$  is a constant equal to 0.09;
- $lengthscale$  is almost 10% of the hydraulic diameter.

Instead, the turbulent kinetic energy was computed as:

$$k = \frac{3}{2} u_i^2 I^2 \quad (3.4)$$

where:

- $u$  is the local velocity;
- $I$  is the turbulence intensity, normally between 0.05 and 0.2 for engines.

As suggested by the software manual, the value of  $k$  was imposed equal to 0.01 while  $\varepsilon$  was calculated with 4.3 with an imposed  $lengthscale$  value equal to 0.005; this strategy was used because the values computed with formulas 3.3 and 3.4 were not precise enough.

### 3.2.2 Regions and Initialization

The regions were used to impose the initializing values of the simulation and the creation of disconnect triangles during the opening and closing of the intake and exhaust valves. In this simulation was defined three regions, Cylinder, Intake System and Exhaust System; in Table 3.2 is reported the subdivision of the boundaries in each region and the three different regions are reported in Figure 3.8.

The creation of disconnect triangles was imposed with the definition of two cyclic events which simulate the opening and closing of intake and exhaust valves, for the first one was defined as an event between the Cylinder and Intake System regions, while the second one between the Cylinder and Exhaust System regions. The software, based on the valve lift profile, imposed in the valve boundaries, automatically derived the start and the end of the valve's motion and consequently when to put on and take off the disconnect triangles.

<b>ID</b>	<b>Boundary Name</b>	<b>Regions</b>
1	Piston	Cylinder
2	Intake Port	Intake System
3	Exhaust Port	Exhaust System
6	Head	Cylinder
7	Injector	Cylinder
8	Injector Nozzle	Cylinder
9	Spark Plug	Cylinder
10	Spark Plug Electrode	Cylinder
11	Exhaust Valve Bottom	Cylinder
12	Exhaust Valve Angle	Exhaust System
13	Exhaust Valve Top	Exhaust System
14	Intake Valve Angle	Cylinder
15	Intake Valve Bottom	Intake System
16	Intake Valve Top	Intake System
17	Liner	Cylinder
18	Intake Port Angle	Intake System
19	Exhaust Port Angle	Exhaust System

*Table 3.2 Boundaries and regions.*

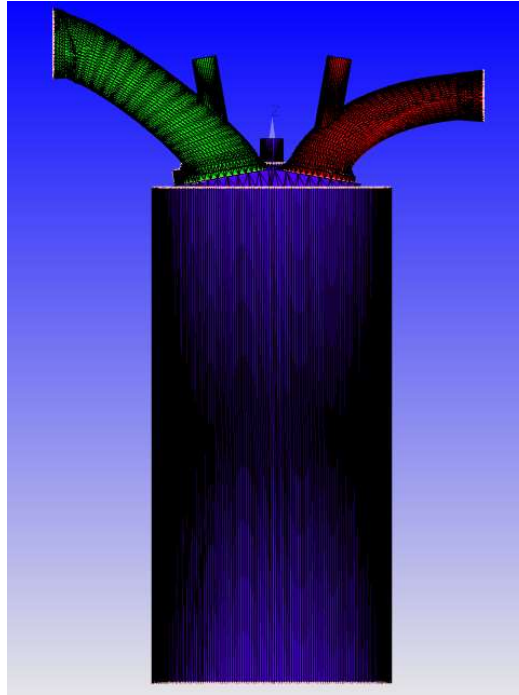


Figure 3.8 Regions: blue cylinder, green intake system and red exhaust system.

Finally, the initialization values can be imposed for the three regions, in this case, the values of turbulent kinetic energy and turbulent dissipation were the same for the different regions, while the temperatures and pressures were different, the values are reported in Table 3.3. The accuracy of these initialization values was not extremely important because the first 200 CAD of the simulation (the exhaust stroke in this simulation) was used to stabilize simulation parameters.

<b>Regions</b>	<b>Temperature [K]</b>	<b>Pressure [Pa]</b>	<b>TKE <math>k</math> [<math>m^2/s^2</math>]</b>	<b>EPS <math>\epsilon</math> [<math>m^2/s^3</math>]</b>
<b>Cylinder</b>	297.0	93833.0	10.0	20000.0
<b>Intake System</b>	295.0	98605.0	10.0	20000.0
<b>Exhaust System</b>	319.0	103200.0	10.0	20000.0

Table 3.3 Initialization values of regions.

### 3.2.3 Grid Control

First of all, the base grid value was imposed equal to 2 mm, with this value the software estimated 65517 cells but the cells needed in some particular places, for example near the cylinder walls, to calculate properly the thermodynamic parameters, were more, for this reason, fixed embedding was set near the boundary around the Cylinder region, i.e. Liner, Piston and Head. The fixed embedding was permanent and had an embedding scale equal to 1, then the cell value was equal to 1 mm. To ensure the correct calculation of the

thermodynamic parameters during the exhaust and intake stroke, another two boundaries were created (i.e. Intake Port Angle and Exhaust Port Angle), and then, was possible to set a permanent fixed embedding on these new boundaries and valves angle (i.e. ID 12,14,18,19), the embedding scale was equal to 2, then the cell value was equal to 0.5 mm.

After that, the Adaptive Mesh Refinement (AMR) was set, in particular, was used two different groups with different embedding criteria, in the first group there was the Cylinder region, for this region was imposed a permanent velocity AMR with a maximum embedding level equal to 3 and a sub-grid criterion equal to 1.0 m/s. Furthermore, a cyclic temperature AMR (starting from -19 CAD and ending at 153 CAD) with a maximum embedding level equal to 3 and a sub-grid criterion equal to 2.5 K. The Intake System was the only region in the second group and the permanent velocity AMR was set with the same parameters as the first group.

With these different grid control methods, the maximum cell number was around 740000.

### 3.3 Cold Cycle Results

First of all, as described above, after the simulation model set-up, a cold cycle was simulated to ensure the correctness of the simulation parameters imposed in the case setup. To verify that the thermodynamic results were correct, the experimental data was used but, for the parameters not measured during the experimental tests the results of the previously validated GT-Power model were used (i.e. Mass flow rate of intake and exhaust valve and In-Cylinder mass)

#### 3.3.1 In-Cylinder Mass

The first step of the model validation was the verification of the In-Cylinder mass, in this case, the experimental data were not available, and then the validation of the simulated result data was performed with the results of the GT-Power simulation. The output file named *region\_flow.out*, in Converge, contained the mass flow rate between the different regions. In this simulation, the start time was -567 CAD before the TDC firing (as reported in 3.1), then, when the exhaust valves opened, this initial phase was used to reach the convergence of thermodynamic parameters, as shown in Figure 3.9, this process required almost 90 CAD.

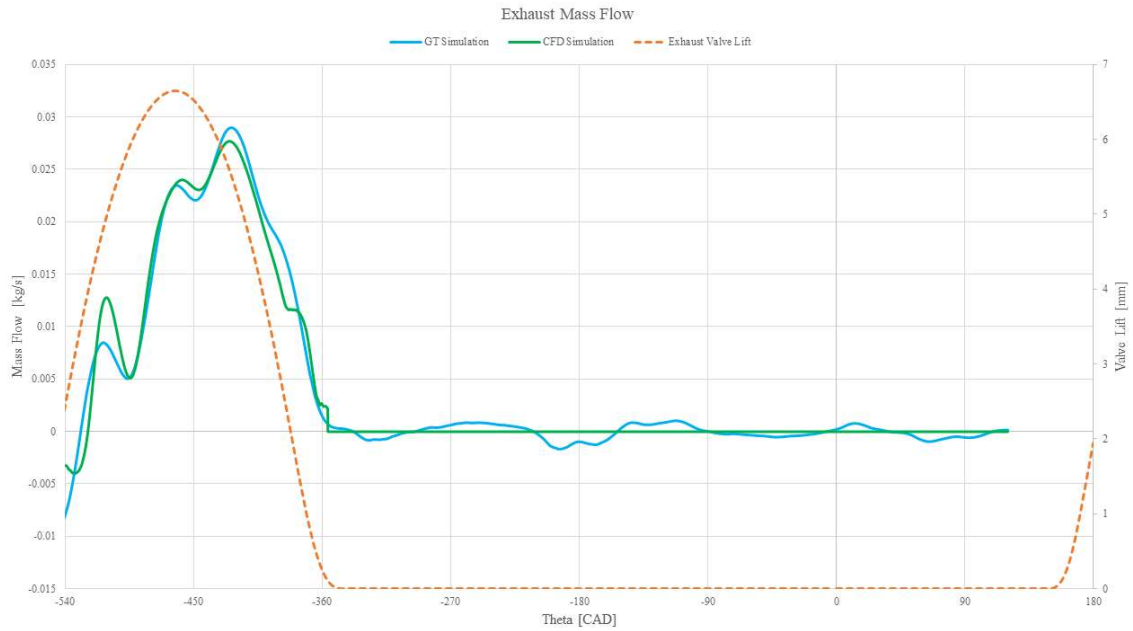


Figure 3.9 Exhaust mass flow of cold cycle and exhaust vales lift.

Indeed, in the first part of the simulation the exhaust mass flow rate had a lot of variabilities, then, at around -460 CAD before the TDC firing, the value was almost the same as GT simulation; after this first part of stabilization, the CFD simulation computed a lower value of mass flow.

An important difference was obtained during the valve closing, indeed, the results of CFD simulation showed a step when the exhaust valves closed (Figure 3.10), this particular trend was due to the fact that the valves close when the value of valve lift was equal to the minimum lift value.

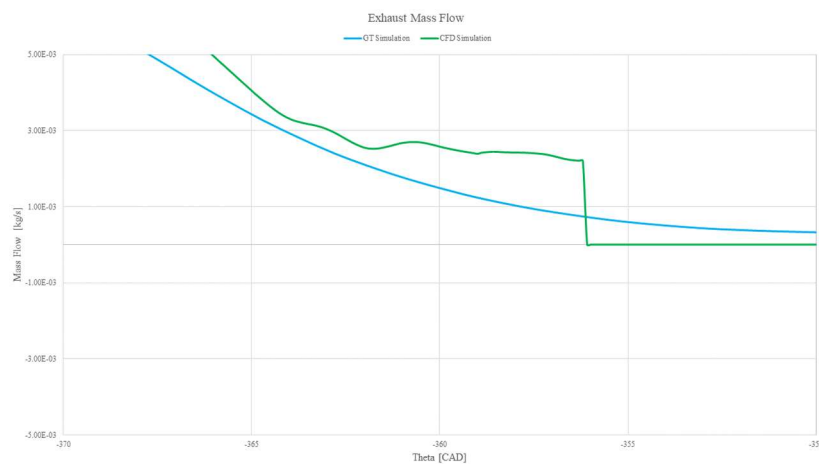


Figure 3.10 Closing phase of exhaust valves.

After the analysis of the exhaust phase, the intake phase was investigated, Figure 3.11 demonstrate the trend of intake mass flow with the two different simulations, i.e. GT simulation and CFD simulation; the value of mass flow rate resulting from the CFD

simulation was slightly lower than the GT simulation, then we could expect a lower value of in-cylinder mass during the intake stroke and compression though the two trends almost coincided during the closing of intake valves.

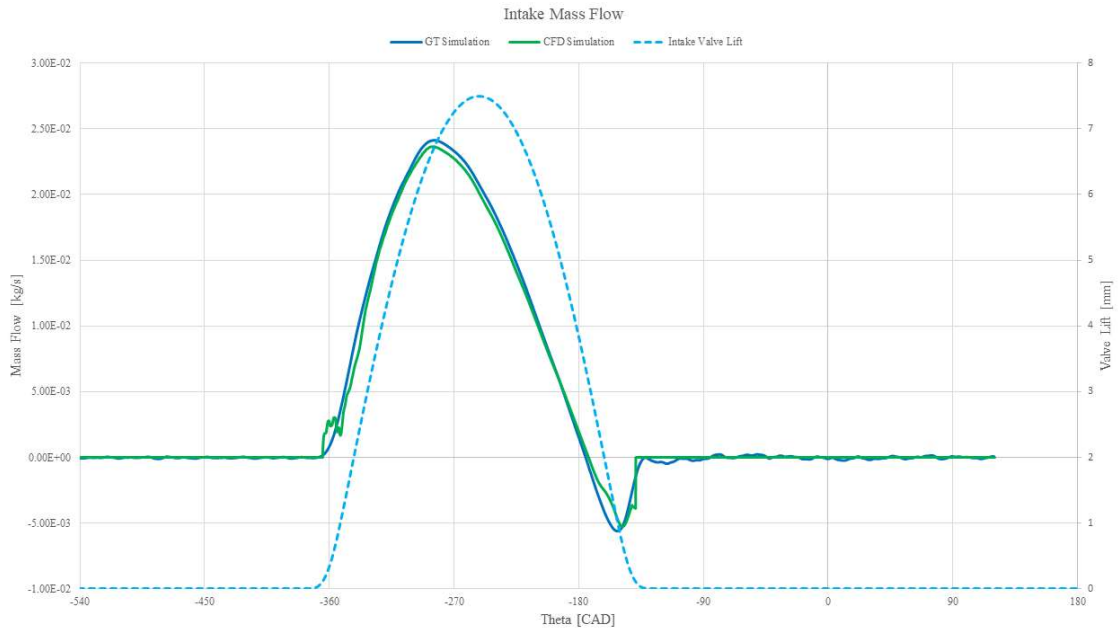


Figure 3.11 Intake mass flow of cold cycle and intake valves lift.

As seen with the exhaust mass flow rate, also the intake mass flow resulting from CFD simulation showed a little step during the intake valves opening and closing (Figure 3.12 and Figure 3.13), the reason was the same as the exhaust valves, when valve motion lift reached the minimum lift the valves opening immediately and the same during the closing.

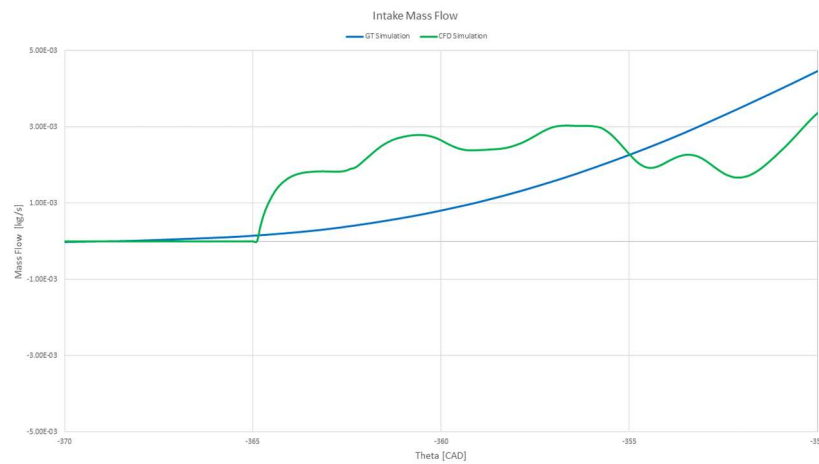


Figure 3.12 Opening phase of intake valves.

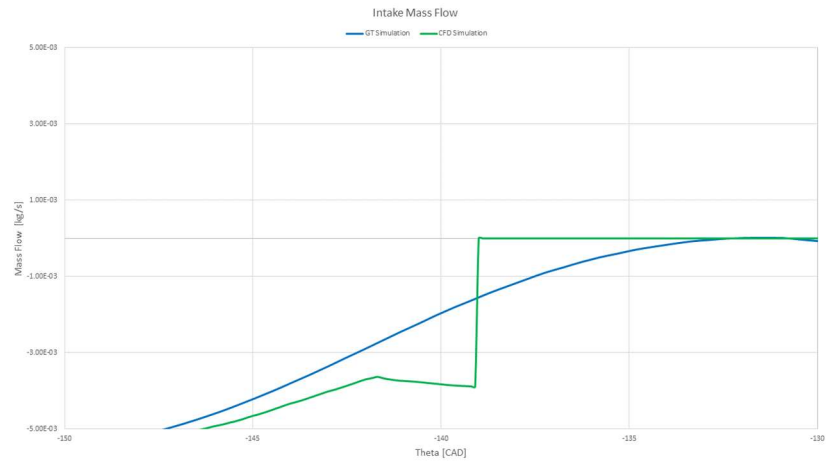


Figure 3.13 Closing phase of intake valves.

The in-cylinder mass result from the CFD simulation was compared with the GT simulation, as expected from the trend of intake mass flow, the mass during the intake and compression stroke was slightly lower than the 1-D simulation (Figure 3.14), but at the TDC firing the CFD trapped mass was equal to 475.84 mg, while the GT simulation value was 476.92 mg, with an error of 0.22%. The lower value of mass was influenced, also, by the residual mass after the exhaust phase, indeed, the exhaust mass flow rate during the exhaust valve closing was higher than the result from GT the simulation as shown in Figure 3.10

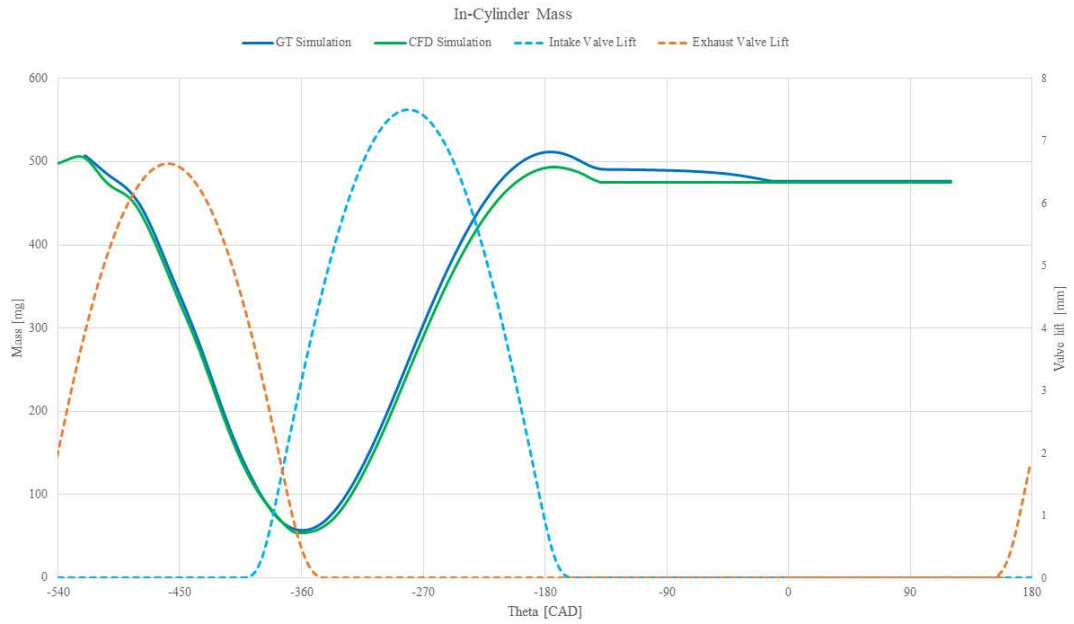


Figure 3.14 In-Cylinder mass during the cold cycle.

### 3.3.2 In-Cylinder Thermodynamic Parameters

To validate the simulation model, in addition to the analysis of the mass in the cylinder, was important to verify the correctness of the in-cylinder pressure and temperature; furthermore, the correctness of the compression ratio and the squish height at the TDC. The results of the CFD simulation were compared with the experimental cold cycle pressure trace.

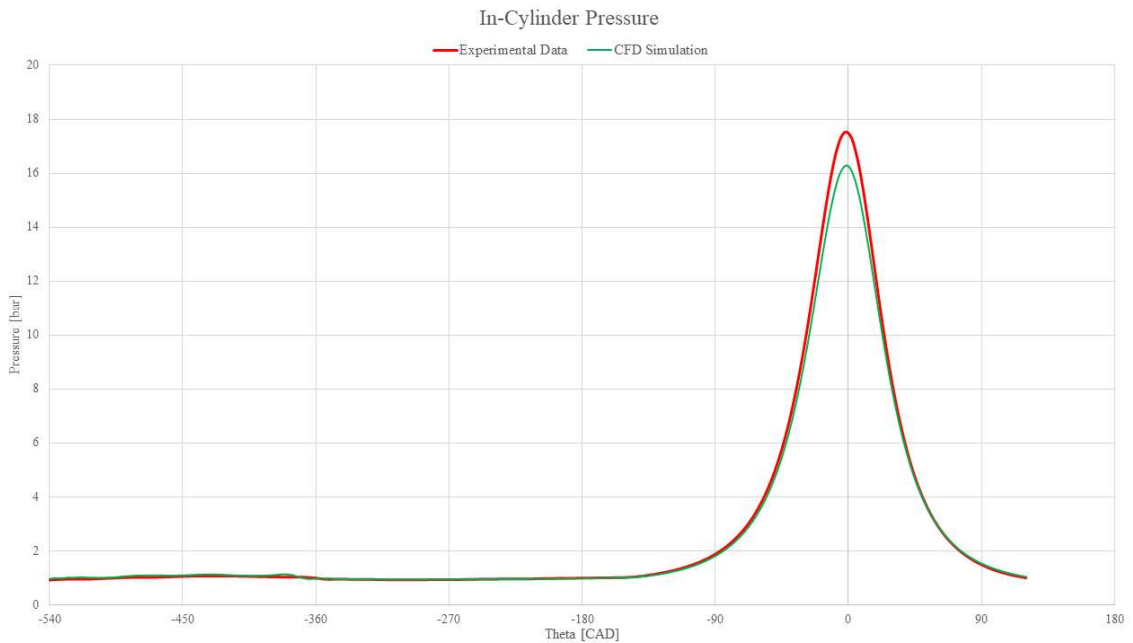


Figure 3.15 In-cylinder pressure during cold cycle.

Figure 3.15 shows that the two pressure traces were very close up to the final part of the compression stroke, thus, the value of pressure, at the beginning of combustion, from the simulation was lower than the experimental one, but the difference was lower than 1 bar, an acceptable error for this particular type of engine.

To better understand the difference between the experimental test data and the simulation results, the logarithmic diagram (Figure 3.16) and the in-cylinder temperature (Figure 3.18) were plotted. Figure 3.16 shows that the differences between the two trends were minimum, in particular, the pumping area of the two results was similar, unlike the lines during the compression and expansion stroke had two different inclinations, this was probably due to a different polytropic compression, then with a different polytropic index. In Figure 3.17 was possible to see the detail of the logarithmic diagram, the simulation started at the beginning of exhaust stroke (A), the simulated results did not match and were slightly higher than the experimental one, these differences decreased as the simulation continued, thus was due to the initial convergence phase, indeed, during the following intake phase (B) the pressure and volume results were equal to the experimental one.

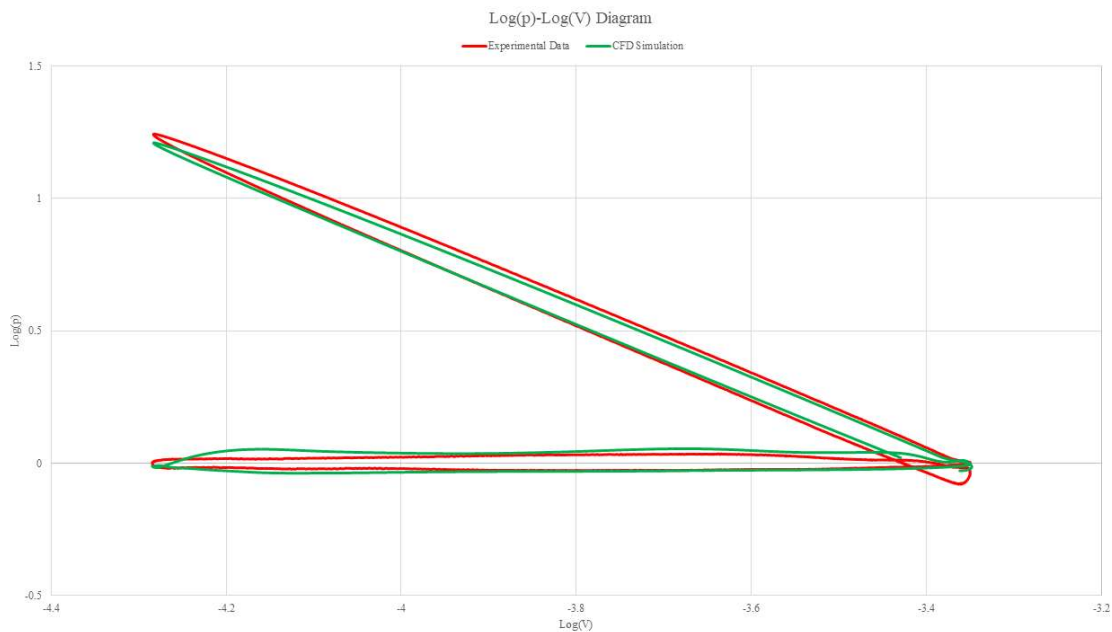


Figure 3.16 Logarithmic diagram of cold cycle.

In this Figure was, also, possible to understand the different inclinations of the polytropic compression and expansion, but at the beginning of compression, the simulated and experimental volume and pressure results were equal (C), then the different peak of pressure was due to the different polytropic processes.

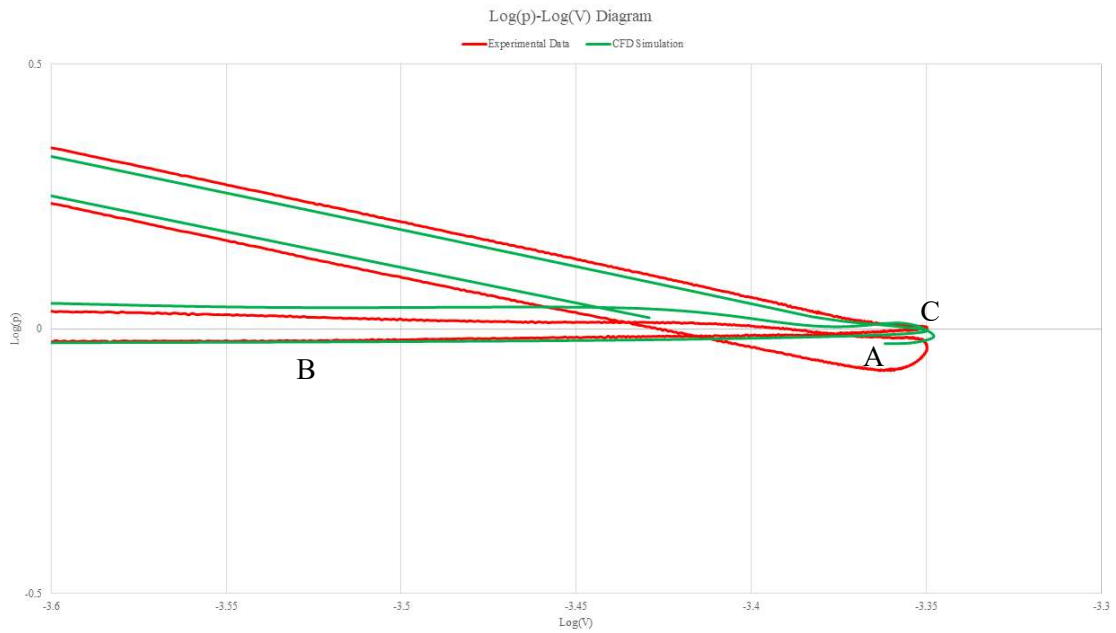


Figure 3.17 Detail of the logarithmic diagram of cold cycle.

Last of all, the in-cylinder temperature was analysed, because the temperature during the whole cycle influenced the trapped mass and the pressure during compression and expansion stroke.

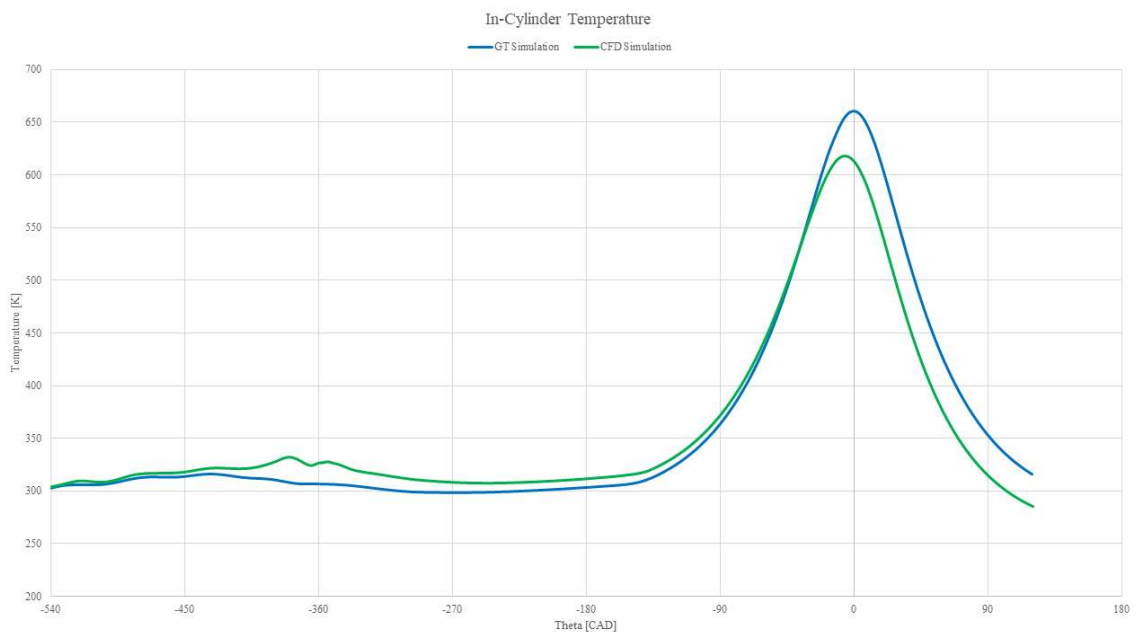


Figure 3.18 In-cylinder temperature during cold cycle.

As for the mass flow rate and in-cylinder mass the comparison was performed with the GT simulation, as reported in Figure 3.18. During the last part of the exhaust process and the intake stroke, the difference between the results was high, while this difference decreased during the compression stroke. As shown in Figure 3.18 the CFD simulation results were

higher than the GT simulation one, and vice-versa at the TDF firing, but at the spark timing, the difference was lower than 25 K.

### 3.3.3 In-Cylinder Motion

This type of analysis was used to evaluate the motion of the air inside the combustion chamber during the intake and compression stroke, this motion was very important because allowed the correct mixing of the air with fuel and the turbulent flame propagation. In this type of engine (DISI) the tumble motion was the most relevant flow motion, this was an organized motion around the y-axis which was generated from the air that entered during the intake stroke; moreover, about the x-axis was generated another motion, called cross tumble which had lower importance, lastly, the motion around the z-axis (swirl) was negligible for this type of engine. Figure 3.19 shows the direction of the three flow motions.

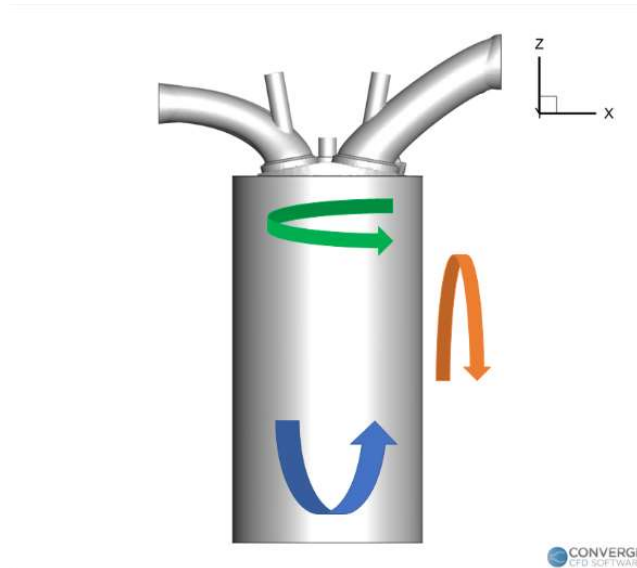


Figure 3.19 Air flow motion inside the chamber: tumble (blue), cross tumble (orange) and swirl (green).

For the reason described above, only the tumble and cross tumble was analysed, furthermore, the turbulence intensity was computed with the formula:

$$\frac{u'}{v_p} = \frac{(tke \cdot 2/3)^{0.5}}{v_p} \quad (3.5)$$

where:

- $tke$  was the turbulent kinetic energy [ $m^2/s^2$ ];
- $v_p$  mean piston speed [ $m/s$ ].

As shown in Figure 3.20 the tumble around the y-axis had the higher values, and then the most relevance in the air motion inside the chamber, while, as expected the cross tumble around the x-axis showed a lower value, around 0.

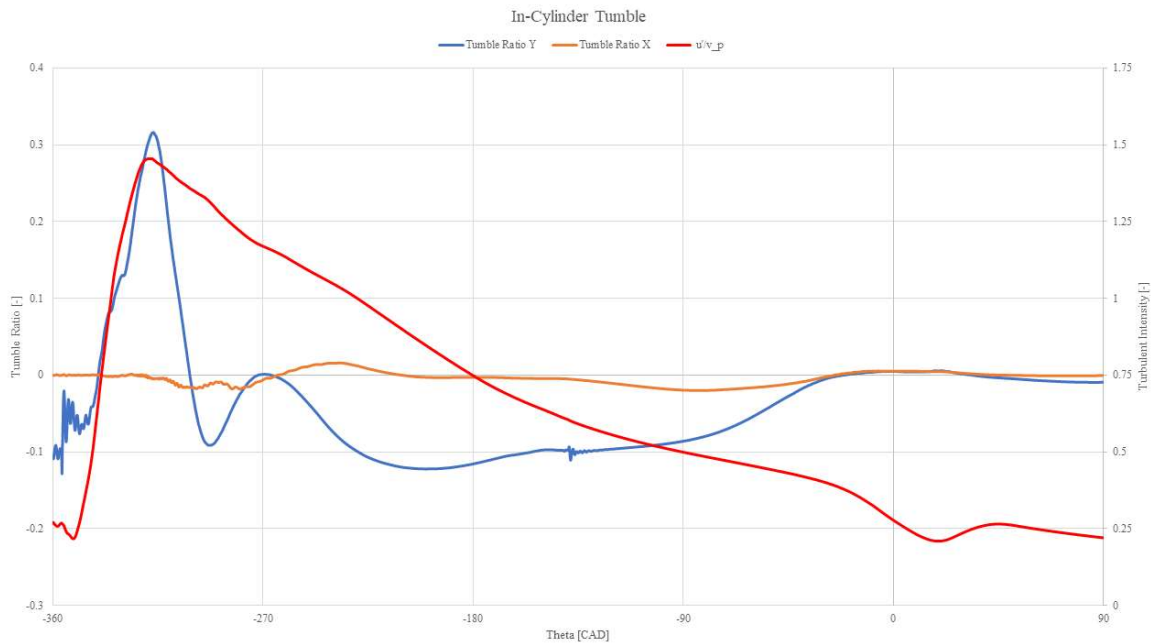


Figure 3.20 Tumble and turbulent intensity of the cold cycle.

The first oscillation of the tumble was due to the initial opening phase of the intake valves, subsequently, the values increased up to 0.3 as the valve lift increased, the direction of the tumble in this first phase was the same as the crankshaft (positive), from -315 CAD the value decreased and change the direction of the motion (Figure 3.21a); during the injection phase the value of tumble increased up to 0, this was due to the interaction between the motion of the trapped air and the liquid spray injected (Figure 3.21b). After that, the tumble increased again in the negative direction and reached the negative maximum value (-0.12) when the intake valves were at the maximum lift (Figure 3.12c). The tumble ratio value, subsequently, decreased in absolute value during the intake valves closing and compression stroke (Figure 3.12d); at the Start of Combustion (SOC), the tumble ratio was positive and slightly over 0 (Figure 3.12e). The tumble motion was correctly converted into turbulence as demonstrated in Figure 3.20 since the turbulence intensity increased as the tumble motion in the first phase, however, this value rapidly decreased during the subsequent phase and reached a value of 0.33 at SOC, this behaviour was due to the flat piston crown.

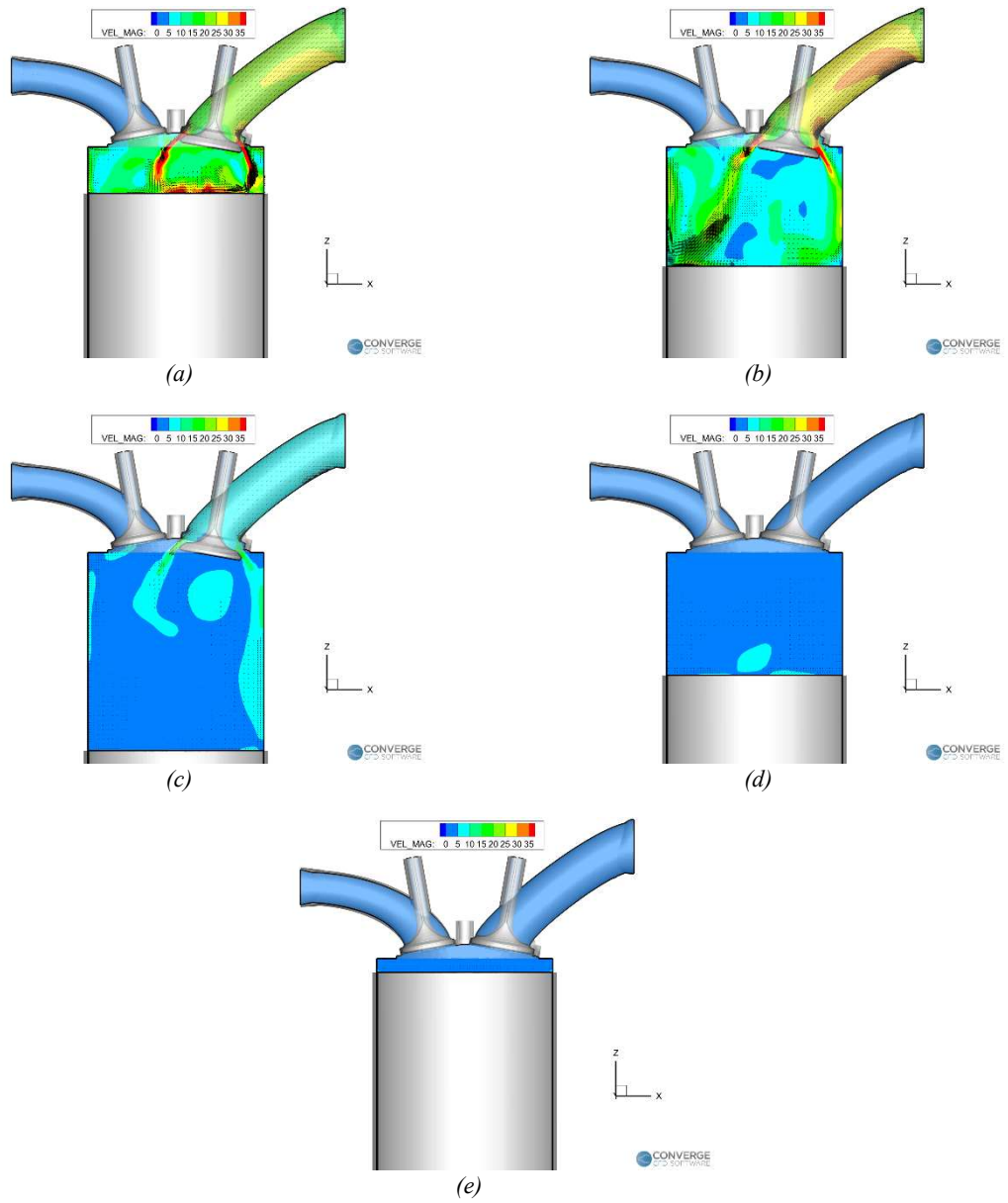


Figure 3.21 Flow motion on the plane passing through the intake valve axis:-315 CAD (a), -270 CAD (b), -200 CAD (c), -90 CAD (d) and -10 CAD (e).

## 4. Conclusions and Future Works

The thesis work, presented above, was focused on the analysis of the combustion in a Direct-Injection Spark-Ignition (DISI) Research Engine and was divided into two main parts; the first part was centred on the analysis of the experimental data carried out during the internship period at CNR-STEMS, this analysis allowed to calculate, mainly, the IMEP values, the  $COV_{IMEP}$  values and the duration of the combustion. During the experimental tests were examined the different conditions of intake pressure, air-to-fuel ratio and 5 types of spark plugs. The main results of these analyses were listed below:

- The  $COV_{IMEP}$  values of all the examined tests were lower than the threshold of 5%.
- The experimental tests with the lower intake pressure and poor mixture were the worst case in terms of IMEP and Cycle-to-Cycle variability, with the same intake pressure but a stoichiometric mixture better results were obtained.
- In the tests performed with the WOT condition, as expected, the cycles with  $\lambda = 1$  showed the better IMEP and  $COV_{IMEP}$  values, while with the higher air-to-fuel ratio the duration of the combustion was almost the same with the different spark plugs.
- Overall, the spark plug configuration and orientation did not demonstrate a noticeable variation in the results with all the engine parameters tested.

In the second part of this work was performed the 3D-CFD Simulation, in particular, the cold cycle simulation was validated based on the experimental data, where available, and on previously validated GT-Power simulation. From the simulation was possible to analyse the tumble motion and the turbulence inside the combustion chamber, as expected for this particular type of engine, the turbulence was very low.

The cold cycle model is an excellent starting point for a future 3D-CFD Simulation of the firing cycle that allows investigation of the flow field and the distribution of the air-fuel ratio into the combustion chamber, these influence the kernel formation and thus the Cycle-to-Cycle variability, especially with during the lean combustion process.



# Acknowledgement

I should like to thank, first of all, my supervisor Prof. Federico Millo for the knowledge and the opportunity to deepen the field of internal combustion engines during his study course, and thank you for the opportunity to develop this thesis work.

A special thanks to my CNR-STEMS supervisors Dr. Simona Silvia Merola and Dr. Eng. Adrian Irimescu for their daily guidance and attention during my internship and during the experimental and simulation analysis.

I would like to thank PhD Andrea Piano and the PhD student Salvatore Roggio, who daily helped me during the development of the 3-D simulation model on Converge Studio.

Furthermore, I cannot fail to mention my parents, without your support and motivation I would never have reached this important goal.

A heartfelt thanks to my girlfriend Anna for supporting me and for her patience, even when the desire to give up was great.

Other important thanks to all my family, in particular to my grandmother for the encouragement and support during the worst moments, always with a smile.

Last but not least, a huge thanks to all my friends, those of always and those I met during this adventure, thanks a lot to everyone.



# References

1. Rapp, V., Killingsworth, N., Therkelsen, P., Evans, R., Lean-burn internal combustion engines. Lean Combustion (Second Edition), Academic Press, 2016, 111-146, <https://doi.org/10.1016/B978-0-12-804557-2.00004-3>.
2. Kalwar, A., & Agarwal, A. K., Lean-burn combustion in direct-injection spark-ignition engines. In Alternative Fuels and Advanced Combustion Techniques as Sustainable Solutions for Internal Combustion Engines, 2021, 281-317, DOI:[10.1007/978-981-16-1513-9\\_12](https://doi.org/10.1007/978-981-16-1513-9_12).
3. Bowditch, F.W., "Cylinder and Piston Assembly", in US Patent App. 2,919,688.
4. Bowditch, F.W., "A New Tool for Combustion Research A Quartz Piston Engine", SAE technical paper 610002, 1961.
5. Irimescu, A., Merola, S., and Martinez, S., Influence of Engine Speed and Injection Phasing on Lean Combustion for Different Dilution Rates in an Optically Accessible Wall-Guided Spark Ignition Engine, SAE Int. J. Engines, 2018, 11(6), 1343–1369, DOI:[10.4271/2018-01-1421](https://doi.org/10.4271/2018-01-1421).
6. Cecere, G., "Visualization of flame-fluid interactions and influence on kernel growth," Master's Thesis, Politecnico di Torino, 2021.
7. Lee, Y., Grimes, D., Boehler, J., Sparrow, J. et al., "A Study of the Effects of Spark Plug Electrode Design on 4-Cycle Spark-Ignition Engine Performance," SAE Technical Paper 2000-01-1210, 2000, <https://doi-org.ezproxy.biblio.polito.it/10.4271/2000-01-1210>.
8. Geiger, J., Pischinger, S., Böwing, R., Koß, H. et al., "Ignition Systems for Highly Diluted Mixtures in SI-Engines," SAE Technical Paper 1999-01-0799, 1999, <https://doi-org.ezproxy.biblio.polito.it/10.4271/1999-01-0799>.
9. Zhao L, Moiz AA, Som S, et al. Examining the role of flame topologies and in-cylinder flow fields on cyclic variability in spark-ignited engines using large-eddy simulation. *International Journal of Engine Research*. 2018;19(8):886-904. doi:[10.1177/1468087417732447](https://doi.org/10.1177/1468087417732447)
10. A. Schirru, A. Irimescu, S. Merola, A. d'Adamo, S. Fontanesi, "Flame Kernel Growth and Related Effects of Spark Plug Electrodes: Fluid Motion Interaction in an Optically Accessible DISI Engine ", World Academy of Science, Engineering and Technology International Journal of Mechanical and Mechatronics Engineering Vol:14, No:3, 2020.
11. <https://www.autodoc.co.uk/bosch/13782787> accessed on Aug, 9<sup>st</sup>, 2022.
12. <https://www.autodoc.co.uk/ngk/1042864> accessed on Aug, 9<sup>st</sup>, 2022.
13. AVL DiTEST GmbH, "USER MANUAL AVL DITEST GAS 1000", [www.avlditest.com](http://www.avlditest.com).
14. Heywood, J.B. Internal Combustion Engine Fundamentals. McGraw Hill. New York, USA, 1988.

15. Cecere, G.; Irimescu, A.; Merola, S.S.; Rolando, L.; Millo, F. Lean Burn Flame Kernel Characterization for Different Spark Plug Designs and Orientations in an Optical GDI Engine. *Energies* **2022**, *15*, 3393. <https://doi.org/10.3390/en15093393>

